

University of Warsaw

MATEUSZ FILA

**Study of  $^{16}\text{O}(\gamma, \alpha)^{12}\text{C}$  nuclear  
reaction with the Warsaw TPC  
detector**

Doctoral thesis

The thesis written under the supervision of  
Prof. dr hab. Wojciech Dominik

Warsaw, August 2023



To my father Mariusz





*With four parameters I can fit an elephant, and  
with five I can make him wiggle his trunk.*

— John von Neumann



# Abstract

The determination of the carbon-to-oxygen ratio produced during the final stages of helium burning in stars poses a significant challenge in nuclear astrophysics. The relevant reactions occur at energies below the Coulomb barrier, making direct measurements highly demanding and associated with considerable uncertainties.

Recently, the utilization of high-intensity  $\gamma$ -ray beams has offered a new opportunity to investigate the crucial  $^{12}\text{C}(\alpha, \gamma)^{16}\text{O}$  reaction, which regulates the carbon-to-oxygen ratio, through the exploration of time-reversal photodisintegration  $^{16}\text{O}(\gamma, \alpha)^{12}\text{C}$  reaction. This method presents certain advantages over previous measurement techniques, including reduced background and different systematic uncertainties.

To exploit this promising approach, a dedicated active-target Time Projection Chamber, known as the WARSAW TPC has been developed at the University of Warsaw. The detector has been designed and optimized to facilitate comprehensive studies using high-intensity  $\gamma$ -ray beams. The detector utilizes an electronic redundant strip readout, DAQ system based on the General Electronics for TPCs (GET), and a stack of three Gas Electron Multiplier (GEM) foils for charge amplification.

In 2022, the WARSAW TPC was deployed for a series of measurements at the High Intensity Gamma-Ray Source (HI $\gamma$ S) facility, located at the Triangle Universities Nuclear Laboratory (TUNL) in Durham, NC, USA. These experiments focused on studying the time-inverse photodisintegration  $^{16}\text{O}(\gamma, \alpha)^{12}\text{C}$  processes utilizing a high-intensity monochromatic  $\gamma$ -ray beam in the center-of-mass energy range of 1.35–6.7 MeV.

This thesis presents the first analysis of that experimental material and one of the first analyses done with any data collected with the WARSAW TPC. The results in form of relative cross-sections for E1 and E2 multipolarity components as well as the E1–E2 mixing phase angle were obtained on a limited statistics achieved with a manual event reconstruction.

The obtained results prove the WARSAW TPC and proposed techniques of data processing and analysis can be effectively used for studies of  $\gamma$ -beam induced nuclear reactions.



## Preface

The following work is a culmination of almost 6 years of work with the WARSAW TPC collaboration at Faculty of Physics of the University of Warsaw. My history with the group started during the first year of my Master studies in November 2017 when my scientific supervisor at that time, dr hab. Agnieszka Korgul prof UW recommended me to take student laboratories with the collaboration. I accomplished that lab, started another, and another, decided to write my Master thesis in scope of the group, and finally begin my doctoral project with it in October 2019.

During my PhD studies I supported a number of the WARSAW TPC group's activities and took a countless responsibilities from being a slow-control expert, the main developer of the detector control system, the main developer of event reconstruction framework, through running laboratory test and measurements, planning future experiments, configuring laboratory network and software systems, to setting up the experiments, taking shifts (including all the night shifts), providing IT support during the experiments, being an event reconstruct expert, and software engineering consultant for Monte Carlo simulations framework, and finally conducting the data analyses.

The time-scale for my PhD studies was very unfortunately. The original plan assumed conducting a calibration experiment with radioactive ion beams at JINR, Dubna, Russia in a middle of 2020 and the full scale experiment with the high intensity  $\gamma$ -beam at HI $\gamma$ S, Durham, USA in late 2020. The outbreak of COVID-19 and the closure of international borders made us rethink the plan entirely.

With a great dedication we were able to refine the operation procedures and progress the software side of the project, and finally attempt the first ever experiment of our detector with the proton-beam at the IFJ PAN, Cracow, Poland in June 2021 and another experiment with neutron generator at the IFJ PAN in July and September 2021. Running two physic experiments in a full sanitary regime of the pandemic is a very peculiar experience. The experiments were successful and managed not only to commission the detector but also to secure very interesting experimental data.

With the improvement in the pandemic situation and the reopening of the international borders we decided to reassume the topic of an experiment at HI $\gamma$ S. Finally in April and in August/September 2022 after many years of delay and facing many adversities the experiment happened and the collected data became the basis of this dissertation.

Note the name of the project was changed from ELITPC to WARSAW TPC to accommodate for the upcoming TPC detector built by the Warsaw collaboration for the ELI-NP experiments.



# Contents

<b>1</b>	<b>Introduction</b>	<b>1</b>
1.1	Stellar nucleosynthesis . . . . .	1
1.2	The $^{12}\text{C}(\alpha, \gamma)^{16}\text{O}$ reaction . . . . .	3
1.3	Previous measurements . . . . .	5
1.4	Detailed balance principle . . . . .	5
1.5	$\gamma$ -ray beams . . . . .	6
1.5.1	Production . . . . .	6
1.5.2	Facilities . . . . .	6
1.6	Charged particle detection . . . . .	8
1.6.1	Stopping power . . . . .	8
1.6.2	Time projection chambers . . . . .	10
1.6.3	OTPC . . . . .	11
1.6.4	e-TPC . . . . .	11
1.6.5	Active target detector . . . . .	11
1.7	Author's contribution . . . . .	12
<b>2</b>	<b>Detector</b>	<b>13</b>
2.1	Detector concept . . . . .	14
2.2	Charge multiplication . . . . .	16
2.3	Readout board . . . . .	17
2.4	DAQ system . . . . .	19
2.4.1	Readout chain . . . . .	19
2.4.2	GET based components . . . . .	20
2.4.3	DAQ PC . . . . .	21
2.4.4	Control room PC . . . . .	22
2.4.5	Storage . . . . .	23
2.5	Online Trigger . . . . .	23
2.5.1	Trigger-modes . . . . .	23
<b>3</b>	<b>Experiment</b>	<b>27</b>
3.1	Overview . . . . .	28
3.2	Background . . . . .	30
3.3	TPC configuration . . . . .	32
3.4	$\gamma$ -beam monitoring . . . . .	33
3.4.1	Alignment . . . . .	33
3.4.2	Beam energy monitoring . . . . .	33
3.4.3	Beam intensity . . . . .	34

3.5	Online trigger & electronics . . . . .	34
<b>4</b>	<b>Reconstruction</b>	<b>37</b>
4.1	Data preprocessing . . . . .	37
4.1.1	Waveform corrections . . . . .	37
4.1.2	Channel mappings . . . . .	43
4.2	Event classification . . . . .	46
4.3	Manual reconstruction . . . . .	51
4.3.1	Experts & datasets . . . . .	51
4.3.2	Procedure . . . . .	52
4.4	Reconstruction quality . . . . .	52
4.4.1	Misidentification . . . . .	53
4.4.2	Reconstruction resolution . . . . .	54
4.4.3	Unpaired dataset . . . . .	54
4.5	Offline trigger . . . . .	57
4.5.1	Implementation . . . . .	57
4.5.2	Trigger Tuning . . . . .	58
4.5.3	Trigger efficiency . . . . .	60
<b>5</b>	<b>Analysis</b>	<b>61</b>
5.1	Beam monitoring . . . . .	61
5.1.1	Intensity . . . . .	61
5.1.2	Energy . . . . .	64
5.1.3	Alignment . . . . .	65
5.2	Data quality . . . . .	67
5.2.1	Drift velocity correction . . . . .	67
5.2.2	Fiducial cuts . . . . .	69
5.2.3	Acceptance correction . . . . .	72
5.3	Event selection . . . . .	74
5.4	Energy scale . . . . .	77
5.4.1	Energy reconstruction . . . . .	77
5.4.2	Energy calibration . . . . .	78
5.4.3	Energy resolution . . . . .	80
5.4.4	Energy unfolding . . . . .	82
5.5	Response uniformity . . . . .	84
5.6	Angular distributions . . . . .	86
5.6.1	Angular resolution . . . . .	86
5.6.2	Azimuthal angle . . . . .	87
5.6.3	Polar angle . . . . .	90
5.6.4	Confidence regions . . . . .	95
5.6.5	Power analysis . . . . .	96
<b>6</b>	<b>Results</b>	<b>99</b>
6.1	Relative cross-section . . . . .	99
6.1.1	Total cross-section . . . . .	100
6.1.2	E1 and E2 cross-section fractions . . . . .	101
6.2	E1–E2 mixing phase angle evolution . . . . .	102



6.3	$\gamma$ -beam energy-spatial position dependence . . . . .	103
6.4	Detector capabilities . . . . .	103
<b>7</b>	<b>Outlook</b>	<b>105</b>
7.1	Machine event reconstruction . . . . .	106
7.1.1	Classical event reconstruction . . . . .	106
7.1.2	Machine learning based event reconstruction . . . . .	107
7.2	Absolute cross-sections . . . . .	109
7.3	Continuation of the experiments . . . . .	109
<b>8</b>	<b>Summary</b>	<b>111</b>
<b>Appendix A</b>	<b>Kinematics of photodisintegration of oxygen</b>	<b>115</b>
A.1	Center of Mass reference frame . . . . .	116
A.2	Laboratory reference frame . . . . .	117
A.3	Useful relations . . . . .	118
<b>Appendix B</b>	<b>Coordinate system</b>	<b>121</b>
B.1	DET and BEAM coordinate systems . . . . .	121
B.1.1	Definition . . . . .	121
B.1.2	Transformation . . . . .	122
B.2	UVW coordinate system . . . . .	123
B.2.1	Definition . . . . .	123
B.2.2	Transformation . . . . .	124
B.3	Reference frames . . . . .	125
<b>Appendix C</b>	<b>Detector Control System</b>	<b>127</b>
C.1	DCS structure . . . . .	128
C.2	Middleware . . . . .	129
C.3	User interface . . . . .	129
C.4	Historical data . . . . .	131
C.5	Experimental equipment and sensors . . . . .	132
C.6	Interlock . . . . .	134
C.6.1	Hardware interlock . . . . .	134
C.6.2	Software interlock . . . . .	134
C.7	Software project . . . . .	135
C.8	3rd party bug fixes . . . . .	135
<b>Appendix D</b>	<b>TPCReco</b>	<b>137</b>



# List of Tables

2.1	Number of readout strips . . . . .	18
3.1	Beam energies . . . . .	29
3.2	Total number of events measured for each energy . . . . .	30
3.3	Separation energies . . . . .	30
3.4	TPC settings . . . . .	32
4.1	Unpaired event classification . . . . .	54
4.2	Offline trigger efficiency . . . . .	60
5.1	Beam distributions measured with HPGe . . . . .	65
5.2	Drift velocity correction factors . . . . .	69
5.3	Acceptance unaffected subsample selection . . . . .	73
5.4	Q-values for selected photodisintegration reactions . . . . .	75
5.5	2-prong isotopic selection . . . . .	76
5.6	Resonance states of oxygen-16 . . . . .	79
5.7	Common polarization states as Stokes vectors . . . . .	87
5.8	Fitted beam polarization parameters . . . . .	89
5.9	Legendre polynomials . . . . .	90
5.10	Cross-section ratios and E1–E2 mixing phase angle . . . . .	93
7.1	Estimated available number of events collected during the experiment .	106
C.1	Experimental equipment used with DCS . . . . .	133



# List of Figures

1.1	Gamow window . . . . .	2
1.2	Oxygen-16 nuclear levels scheme . . . . .	3
1.3	S-factor . . . . .	4
1.4	Total S-factor uncertainties . . . . .	4
1.5	Ratio of cross-section of $^{16}\text{O}(\gamma, \alpha)^{12}\text{C}$ and $^{12}\text{C}(\alpha, \gamma)^{16}\text{O}$ reactions . . .	6
1.6	Scheme of a Compton back-scattering . . . . .	7
1.7	Scheme of the $\gamma$ -beam production system at the HI $\gamma$ S facility . . . . .	8
1.8	Brag curves . . . . .	9
1.9	TPC principle of operation . . . . .	10
1.10	OTPC principle of operation . . . . .	11
2.1	Detector cross-section . . . . .	14
2.2	Scheme of detector internal structure . . . . .	15
2.3	GEM foils . . . . .	16
2.4	Photograph of the readout pads . . . . .	17
2.5	Structure of WARSAW TPC readout . . . . .	17
2.6	Readout strip section . . . . .	18
2.7	DAQ readout chain scheme . . . . .	19
2.8	Trigger . . . . .	24
2.9	Trigger mode effects on the drift axis coordinate . . . . .	25
3.1	Photo of experimental setup at HI $\gamma$ S . . . . .	27
3.2	Scheme of experimental setup . . . . .	28
3.3	Experimental points . . . . .	29
3.4	Separation energies . . . . .	31
3.5	Beam alignment with BGO . . . . .	33
3.6	Trigger and beam rate for HI $\gamma$ S experiment . . . . .	35
4.1	Raw electronics waveform . . . . .	38
4.2	Average electronics waveforms for different channels . . . . .	38
4.3	Comparison of shaping times . . . . .	40
4.4	Electronic waveform corrections . . . . .	41
4.5	Noise reduction with signal corrections . . . . .	42
4.6	Electronic waveform event representation . . . . .	43
4.7	Logical channel mapping . . . . .	44
4.8	Physical channel mapping . . . . .	45
4.9	Typical noise . . . . .	47
4.10	Typical dot-like event . . . . .	47

4.11	Typical 1-prong event . . . . .	48
4.12	Typical 2-prong event . . . . .	48
4.13	Typical proton-nitrogen event candidate . . . . .	49
4.14	Typical 3-prong event . . . . .	49
4.15	Pile-up event example . . . . .	50
4.16	Example 3-prong event misidentified as a 2-prong . . . . .	53
4.17	Reconstructed track length consistency . . . . .	55
4.18	Post hoc track length analysis . . . . .	56
4.19	Level-2 offline trigger . . . . .	58
4.20	Offline trigger sensitivity . . . . .	59
5.1	Beam stability . . . . .	62
5.2	Trigger rate stability . . . . .	63
5.3	HPGe spectrum unfolding . . . . .	64
5.4	Beam tilt fit . . . . .	66
5.5	Beam spatial distributions . . . . .	66
5.6	Drift velocity simulation . . . . .	67
5.7	Drift velocity correction estimation . . . . .	68
5.8	Fiducial cut: vertex position . . . . .	70
5.9	Fiducial cut: border padding . . . . .	70
5.10	Fiducial cut: global Z-span . . . . .	71
5.11	Fiducial cut: relative Z-span . . . . .	71
5.12	Fiducial cut sequence . . . . .	72
5.13	Density of reconstructed events . . . . .	74
5.14	Acceptance cut . . . . .	75
5.15	Isotope selection . . . . .	76
5.16	Ion ranges in CO <sub>2</sub> . . . . .	77
5.17	Energy reconstruction methods comparison . . . . .	78
5.18	Energy calibration . . . . .	79
5.19	Energy resolution . . . . .	80
5.20	Energy spectrum of run $E_\gamma = 11.9$ MeV . . . . .	81
5.21	Normalized detector response matrix . . . . .	82
5.22	Center of mass energy after applying energy reconstruction, calibration and unfolding. . . . .	83
5.23	Comparison of $\alpha$ kinetic energy for subsamples “up” and “down” . . . . .	85
5.24	Probability distribution for beam polarization . . . . .	88
5.25	Beam polarization fit . . . . .	89
5.26	Probability distribution for angular distribution . . . . .	91
5.27	Fitted polar angle distribution . . . . .	92
5.28	Polar angle distribution fitted to energy selected data . . . . .	94
5.29	Confidence regions . . . . .	95
5.30	Power of a test against pure E1 and pure E2 alternatives . . . . .	97
6.1	Relative total $^{16}\text{O}(\gamma, \alpha)^{12}\text{C}$ cross-section . . . . .	100
6.2	E1 to total cross-section ratio . . . . .	101
6.3	E1–E2 mixing phase angle evolution . . . . .	102
6.4	Reconstructed $\gamma$ energy position dependence . . . . .	103

7.1	Classic machine event reconstruction . . . . .	107
7.2	Event classification model confusion matrix . . . . .	108
A.1	Center of Mass reference frame . . . . .	116
A.2	Laboratory reference frame . . . . .	117
A.3	Center-of-Mass (CM) to LAB transformation . . . . .	119
B.1	DET and BEAM coordinate systems . . . . .	121
B.2	Beam tilt correction . . . . .	123
B.3	UVW coordinate system . . . . .	124
C.1	DCS scheme . . . . .	127
C.2	DCS structure . . . . .	128
C.3	DCS GUI . . . . .	130
C.4	Grafana dashboard example . . . . .	131
D.1	TPCReco GUI . . . . .	138





# List of Acronyms

<b>ADC</b>	Analog-to-Digital Converter
<b>AGET</b>	ASIC for GET
<b>AsAd</b>	ASIC & ADC
<b>ASIC</b>	Application-Specific Integrated Circuit
<b>BGO</b>	Bismuth Germanium Oxide
<b>CDF</b>	Cumulative Density Function
<b>CM</b>	Center-of-Mass
<b>CoBo</b>	Concentrator Board
<b>DAQ</b>	Data acquisition
<b>DB</b>	Database
<b>DCS</b>	Detector Control System
<b>ELI-NP</b>	Extreme Light Infrastructure Nuclear Physics
<b>FEL</b>	Free Electron Laser
<b>FPGA</b>	Field-Programmable Gate Array
<b>FPN</b>	Fixed-Pattern Noise
<b>GEM</b>	Gas Electron Multiplier
<b>GET</b>	General Electronics for TPCs
<b>GUI</b>	Graphical User Interface
<b>GoF</b>	goodness-of-fit
<b>HEP</b>	High Energy Physics
<b>HI<math>\gamma</math>S</b>	High Intensity Gamma Source
<b>HPC</b>	High-Performance Computing
<b>HPGe</b>	High Purity Germanium
<b>HV</b>	High Voltage
<b>K-S</b>	Kolmogorov-Smirnov
<b>LRT</b>	Likelihood Ratio Test
<b>LV</b>	Low Voltage
<b>PSU</b>	Power Supply Unit
<b>MLE</b>	Maximum Likelihood Estimation

**ML** Machine Learning  
**MPAD** Mirror Paddle Detector  
**OCI** Open Container Initiative  
**OTPC** Optical Time Projection Chamber  
**PCB** Printed Circuit Board  
**PDF** Probabilty Density Function  
**PID** Proportional-Integral-Derivative  
**R&D** Research and Development  
**SCADA** Supervisory Control And Data Acquisition  
**SPAD** Single Paddle Detector  
**SRIM** Stopping and Range of Ions in Matter  
**TPC** Time Projection Chamber  
**TUNL** Triangle Universities Nuclear Laboratory  
**UTR** Upper Target Room  
**VSC** Version Control System

# Glossary

**beam nominal energy** the symbol  $E_\gamma$  is used for nominal  $\gamma$ -beam energy in the LAB (target rest frame) reference frame. This value does not necessary reflect the real mean or mode of the beam delivered, rather than reflect a setting of the beam requested and is supposed to be a rough approximation of the real beam. In the following sections and chapters this value is used like a human readable identifier that informs the reader about the approximated beam energy in place of enigmatic run identification number.

**center of mass energy** the symbol  $E_{\text{CM}}$  is used for the kinetic energy of the system in the center of mass reference frame. A low-energy nuclear physics community convention is used to give a non-relativistic value not including the rest mass is used, as opposed to the relativistic center-of-mass energy  $\sqrt{s}$  used by the High Energy Physics community (HEP).

**endpoint** a point where a charged particle's trajectory ends within a particle detector..

**prong** a track or path left by a charged particle within a particle detector. When a charged particle moves through a detector, it can leave behind a visible trail of detector hits or signals. Each such path is called a “prong,” and it represents the path taken by the particle as it traverses the detector.

**vertex** a point in a spacetime where a reaction or decay takes place. Point of origin of the reaction products.



# Chapter 1

## Introduction

*It is little wonder that the determination of the ratio  $^{12}\text{C}/^{16}\text{O}$  produced in helium burning is a problem of paramount importance in Nuclear Astrophysics.*

— William A. Fowler, 1984

### 1.1 Stellar nucleosynthesis

From the ancient times people pondered about their origin and place in the world. Today, thanks to the nuclear astrophysics, we know that the atomic nuclei of our bodies and our environment were created inside the stars in a process known as a stellar nucleosynthesis.

The stellar nucleosynthesis is a multistage process closely tied to the evolution of a star. In the first stage a young star consists mostly of hydrogen, that is being burned into the helium-4. As the compositions of a star changes, another process, a so-called  $3\alpha$  process:  $3\alpha \rightarrow ^{12}\text{C}$ , becomes viable and a star enters the helium burning stage.

The carbon-12 created in the  $3\alpha$  process can be converted to oxygen-16 in an  $\alpha$ -capture reaction of  $^{12}\text{C}(\alpha, \gamma)^{16}\text{O}$ . The relative rates of these reactions determine the abundances of the carbon-12 and oxygen-16. The time evolution of the molar abundances can be described by a system of equations [1]:

$$\begin{aligned} \frac{d[^{12}\text{C}]}{dt} &= \frac{1}{3!}[\alpha]^3 \rho^2 \lambda_{3\alpha} - [\alpha][^{12}\text{C}] \rho \lambda_{^{12}\text{C}(\alpha, \gamma)^{16}\text{O}} \\ \frac{d[^{16}\text{O}]}{dt} &= [\alpha][^{12}\text{C}] \rho \lambda_{^{12}\text{C}(\alpha, \gamma)^{16}\text{O}} - [\alpha][^{16}\text{O}] \rho \lambda_{^{16}\text{O}(\alpha, \gamma)^{20}\text{Ne}} \end{aligned} \quad (1.1)$$

where  $[\alpha]$ ,  $[^{12}\text{C}]$  and  $[^{16}\text{O}]$  are the molar abundances of the corresponding nuclei,  $\rho$  is the density and  $\lambda_i$  is a rate of corresponding reaction. The ratio of abundances of carbon-12 to oxygen-16 at the end of the helium burning is an important parameter for the modelling of stellar evolution [2].

In order to determine the ratio, the rates of  $3\alpha$  process  $^{12}\text{C}(\alpha, \gamma)^{16}\text{O}$  should be known. A stellar reaction rate can be calculated from a Maxwell-Boltzmann distribution defined by a stellar temperature  $T$ , and the reaction's cross-section  $\sigma$ [3]:

$$N_A \langle \sigma v \rangle = \sqrt{\frac{8}{\pi \mu (k_B T)^3}} N_A \int_0^\infty dE \sigma(E) E e^{-E/k_B T} \quad (1.2)$$

where  $N_A$  is the Avogadro constant,  $k_B$  is Boltzmann constant,  $\mu$  is reduced mass of the reaction substrates, and  $v$  is relative velocity of the substrates.

For the reactions of charged particles the cross-section can be factorized into the astrophysical S-factor  $S$  and tunneling through the Coulomb barrier [2]:

$$S(E) = \sigma(E) E e^{2\pi\eta} \quad (1.3)$$

where  $\eta$  is the Sommerfeld parameter defined as  $\alpha Z_1 Z_2 \sqrt{\frac{\mu c^2}{2E}}$  for  $Z_i$  being a charge of a substrate,  $\alpha$  being the fine-structure constant and  $c$  being the speed of light. The S-factor is a commonly used variable in the nuclear astrophysics domain. By expressing the Equation 1.2 with a S-factor one can obtain:

$$N_A \langle \sigma v \rangle = \sqrt{\frac{8}{\pi \mu (k_B T)^3}} N_A \int_0^\infty dE S(E) e^{-E/k_B T - 2\pi\eta} \quad (1.4)$$

For slowly changing reactions the value under integral is governed by the exponential term. The exponential term has a peak structure and describes a so-called Gamow window depicted in the Figure 1.1. Therefore the majority of non-resonance stellar reactions occur at relatively narrow energy window.

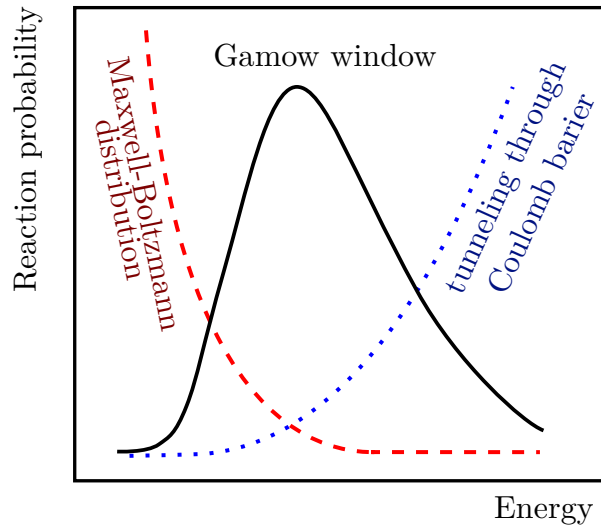


Figure 1.1: Gamow window. A Gamow window is narrow energy window where a stellar reaction occur. The window is a result of product of two probabilities: the probability density of Maxwell-Boltzmann distribution due to thermal equilibrium and probability of tunneling through a Coulomb barrier.

## 1.2 The $^{12}\text{C}(\alpha, \gamma)^{16}\text{O}$ reaction

Given its importance for determining the  $^{12}\text{C}/^{16}\text{O}$  and its elusiveness the  $^{12}\text{C}(\alpha, \gamma)^{16}\text{O}$  reaction was nicknamed in the literature as “the key reaction” or “the holy grail of nuclear astrophysics” [1]. The Gamow window for this reaction for red giant stars is located at around  $E_{\text{CM}} = 300$  keV. The cross-section value at this energy is estimated to be around  $10^{-17}$  b and orders of magnitude lower than the current experimental sensitivity.

The cause for such low cross-section is the existence of large Coulomb potential and the fact that at the oxygen-16 have no resonant levels at the Gamow energy. With the lack of resonant levels the reaction occurs on the tails of existing levels:  $1^-$  at 7.12 MeV and  $1^-$  at 9.59 MeV or  $2^+$  at 6.92. Since the states differ by angular momentum and parity different multipolarities of  $\gamma$ -ray are observed from their decays to the ground state: E1 for  $1^-$  and E2 for  $2^+$  states. Determining the contributions from each state pose an additional complication to the problem. The level scheme of oxygen-16 is shown in the Figure 1.2.

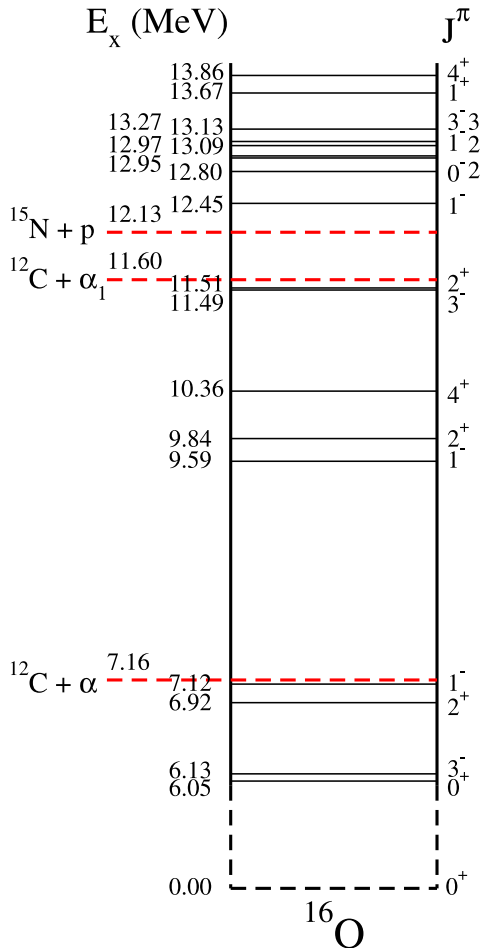


Figure 1.2:  $^{16}\text{O}$  nuclear levels scheme. Irrelevant levels are omitted. Figure taken from [1].

With the lack of experimental data for the relevant Gamow window, the cross-section value for that region is extrapolated with a theoretical fits, such as R-matrix [1], to the experimental data from higher energy regions. For stellar evolution modeling a goal of achieving 10% of uncertainty of that extrapolation is often mentioned [4].

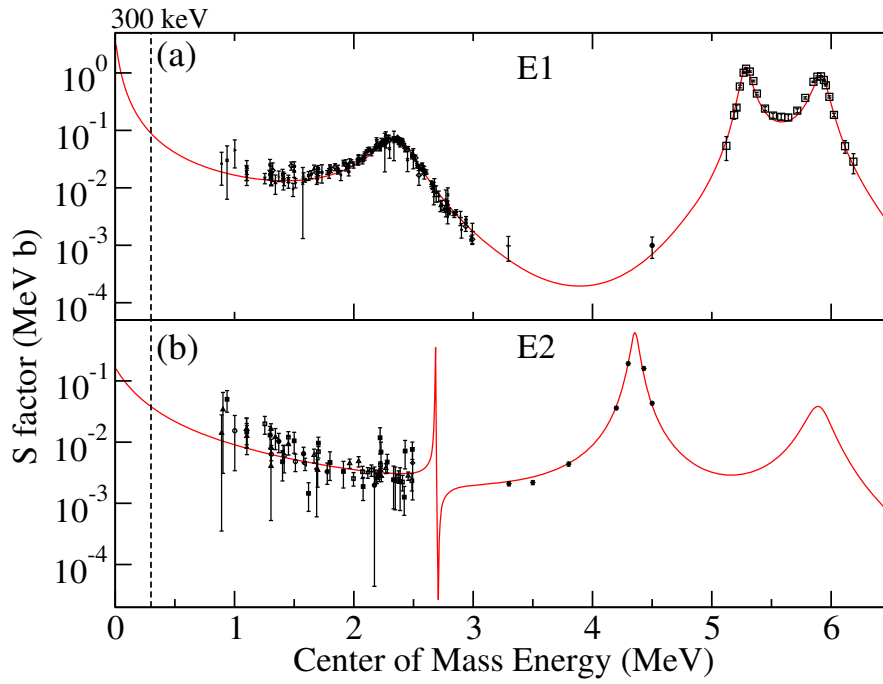


Figure 1.3: S-factor of the  $^{12}\text{C}(\alpha, \gamma)^{16}\text{O}$  reaction. The S-factor for E1-transition is presented on top, the S-factor for E2 transition on bottom. The stripped line at the 300 keV marks the Gamow window for the red giant stars. The red line is a R-matrix fit to the experimental data. Figure taken from [1].

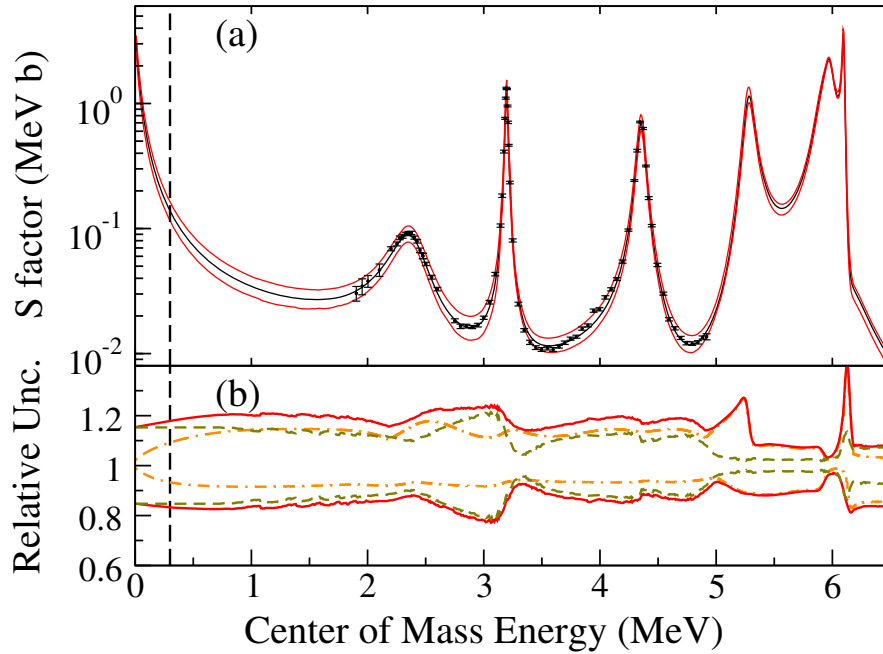


Figure 1.4: Total  $^{12}\text{C}(\alpha, \gamma)^{16}\text{O}$  reaction S-factor. Top: theoretical R-matrix fit to the experimental data is show. Bottom: uncertainties of the fit are given. Figure taken from [1].



### 1.3 Previous measurements

Due to its importance for the domain over the years the  $^{12}\text{C}(\alpha, \gamma)^{16}\text{O}$  reaction was at the aim of many experiments. With the experimental data collected over the decades the uncertainties of the reaction's cross-section at stellar evolution relevant energy of 300 keV were significantly lowered but the end-goal of reaching the required 10% is still far. Collected experimental points as well as a theoretical R-matrix fit is depicted in the Figures 1.3 and 1.4.

A traditional experiment on the  $^{12}\text{C}(\alpha, \gamma)^{16}\text{O}$  consists of an  $\alpha$ -beam and carbon target. The produced  $\gamma$ -rays are measured by  $\gamma$ -detectors. Usually an array of the detectors is used in order to measure the angular distribution of the radiation and determine its multipolarity. This experiment scheme was explored over the years with the used of either NaI detectors [5] or arrays of High Purity Germanium (HPGe) and Bismuth Germanium Oxide (BGO) [6, 7] or  $\text{BF}_2$  and BGO [8] detectors.

The consensus is that the direct measurement exploitation is reaching the end as pushing for lower energies is meeting technical barriers such as time-scale of the experiment or the problem of cooling of the target. Instead of abandoning the prospect of determining its cross-section at the relevant energies the effort is placed on researching other indirect methods.

In recent years a novel promising approach of studying the time inversed  $^{16}\text{O}(\gamma, \alpha)^{12}\text{C}$  reaction was developed and studied with an Optical Time Projection Chamber (OTPC) [9]. The experimental approach to study the photodisintegration reaction is very different from the classical approach, as instead of detecting the  $\gamma$ -rays from deexcitation of oxygen with a  $\gamma$ -detector, a tracking detector used to measure the charged products of the disintegration reaction  $^{16}\text{O}(\gamma, \alpha)^{12}\text{C}$ .

The photodisintegration indirect method of studying the  $^{12}\text{C}(\alpha, \gamma)^{16}\text{O}$  is one of the main subjects of this work.

### 1.4 Detailed balance principle

Due to strong and electromagnetic interactions being invariant under time reversal operation, the cross sections of reactions of alpha-capture  $^{12}\text{C}(\alpha, \gamma)^{16}\text{O}$  and time reversed photodisintegration  $^{16}\text{O}(\gamma, \alpha)^{12}\text{C}$  can be related by the detailed balance principle [10]:

$$^{12}\text{C}(\alpha, \gamma)^{16}\text{O} \rightleftharpoons ^{16}\text{O}(\gamma, \alpha)^{12}\text{C} \quad (1.5)$$

The formula allows for calculating the cross-section of direction reaction  $\sigma_{\alpha\gamma}$  based on the cross-section of photodisintegration  $\sigma_{\gamma\alpha}$ , momentum  $p$  and spin factor  $g$  of each system:

$$\sigma_{\alpha\gamma} \cdot g_{\alpha\gamma} \cdot p_{\alpha\gamma}^2 = \sigma_{\gamma\alpha} \cdot g_{\gamma\alpha} \cdot p_{\gamma\alpha}^2 \quad (1.6)$$

After a substitution a final formula expressed with spins  $J$ , reduced mass  $\mu_{\alpha\text{C}}$  of  $\alpha$ -C system,  $\gamma$ -beam energy  $E_\gamma$ , and center of mass energy  $E_{\text{CM}}$  can be obtained (kinematics of the problem discussed in Appendix A):

$$\sigma_{\alpha\gamma} = \sigma_{\gamma\alpha} \frac{2J_O + 1}{(2J_\alpha + 1)(2J_C + 1)} \cdot \frac{E_\gamma^2}{E_{CM}} \cdot \frac{1}{\mu_{\alpha C} c^2}, \quad (1.7)$$

The ratio of the direct and photodisintegration reactions cross-sections is a simple function of the energy depicted in the Figure 1.5. Note the cross-section of  $^{16}\text{O}(\gamma, \alpha)^{12}\text{C}$  reaction is one order of magnitude larger in the energy range relevant to this study.

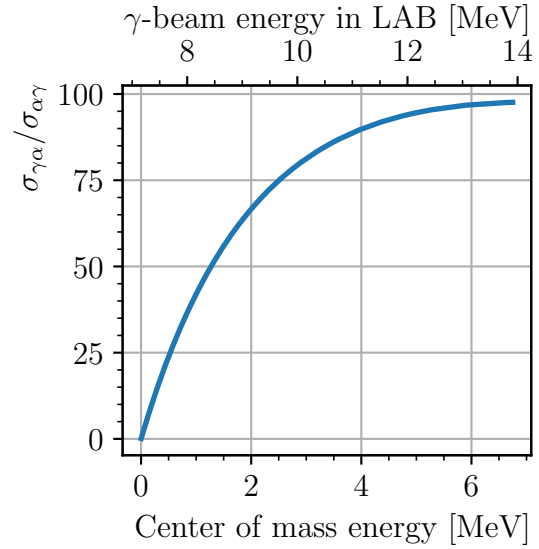


Figure 1.5: Ratio of cross-section of  $^{16}\text{O}(\gamma, \alpha)^{12}\text{C}$  and  $^{12}\text{C}(\alpha, \gamma)^{16}\text{O}$  reactions. The cross-sections are related by the detailed balance principle. The  $^{16}\text{O}(\gamma, \alpha)^{12}\text{C}$  cross-section is larger than the  $^{12}\text{C}(\alpha, \gamma)^{16}\text{O}$  cross-section.

## 1.5 $\gamma$ -ray beams

The  $^{16}\text{O}(\gamma, \alpha)^{12}\text{C}$  reaction cross-sections varies significantly with the energy. The prospect of conducting a oxygen-16 photodisintegration experiment requires an access to a monochromatic, high-intensity  $\gamma$ -beam source. The quality and precision of the measurements results strongly depend on the characteristic of the source used.

### 1.5.1 Production

The state-of-the-art technique for producing high-intensity  $\gamma$ -beam is a Compton back-scattering of laser photons on accelerated electron beam. The scheme of Compton back-scattering is presented in the Figure 1.6. For small scattering angles  $\theta$  the  $\gamma$ -beam energy  $E_\gamma$  is given by:

$$E_\gamma = 4\gamma^2 E_0 \frac{1}{1 + (\theta\gamma)^2 + \frac{4E_0\gamma}{m_e c^2}} \approx 4\gamma^2 E_0, \quad (1.8)$$

where,  $E_0$  – laser energy,  $\gamma$  – electron beam Lorentz factor,  $m_e$  – electron mass.

### 1.5.2 Facilities

In contrast to all the types of charged particle accelerators or neutron generators the construction of brilliant, high-intensity  $\gamma$ -beam facilities became feasible relatively

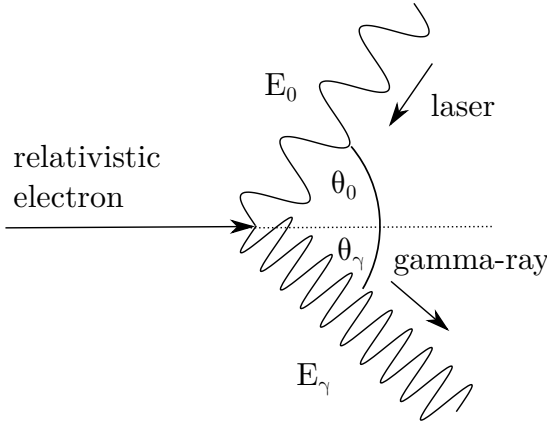


Figure 1.6: Scheme of a Compton back-scattering process using laser beam. Gamma-ray beam with energy  $E_\gamma$  is obtained from back-scattering laser photons with energy  $E_0$  on a relativistic electron beam. The laser beam collides at angle  $\theta_0$  and the gamma-ray beam is back-scattered at angle  $\theta_\gamma$ .

recently and currently only three facilities are considered to be capable to deliver a  $\gamma$ -beam of features required for the study:

1. High Intensity Gamma Source (HI $\gamma$ S), Triangle Universities Nuclear Laboratory (TUNL), Durham, North Carolina, USA.
2. NewSUBARU, Hyogo, Japan,
3. Extreme Light Infrastructure Nuclear Physics (ELI-NP), Măgurele, Romania.

## HI $\gamma$ S

HI $\gamma$ S is an operating state-of-the-art  $\gamma$ -beam facility [11]. The facility is capable of delivering a  $\gamma$  beam of energy up to 225 MeV with an intensity of  $10^8$ – $10^9$   $\gamma$ /s. The available  $\gamma$ -beam is not monochromatic but characterized by a finite width of approximately 3% full width at half maximum (FWHM). The generate  $\gamma$ -beams can be either quasi-continuos or pulsed with different beam polarities. The facility is equipped in a diagnostics system capable of online beam monitoring.

A scheme of the HI $\gamma$ S facility is depicted in the Figure 1.7. The  $\gamma$ -beam production method is based on the Compton back-scattering of a Free Electron Laser (FEL) photons on relativistic electrons accelerated in a linear particle accelerator (linac). The linac is capable of producing an electron beam of intensity of  $10^{10}$  e/s and up to 0.28 GeV, which is later accelerated by a booster synchrotron to up to 1.3 GeV.

The relativistic electrons are injected into a storage ring and organized into bunches. An optical klystron FEL system (OK-4, OK-5) is used to produce the photon beam. The initial beam is produced from the synchrotron radiation of oscillating electrons passing by the magnetic field of the wiggler magnets of OK systems. The  $\gamma$ -beam is produced in a collision and Compton scattering of collinear FEL beam and a previous bunch of electrons. Resulting  $\gamma$ -rays are characterized by a broad energy spectrum and a beam of relatively narrow energy width is obtained by collimation.

## ELI-NP

The future  $\gamma$ -beam system at the ELI-NP is expected to further push the experimental technique and open new opportunities for studies [12]. The anticipated brilliant

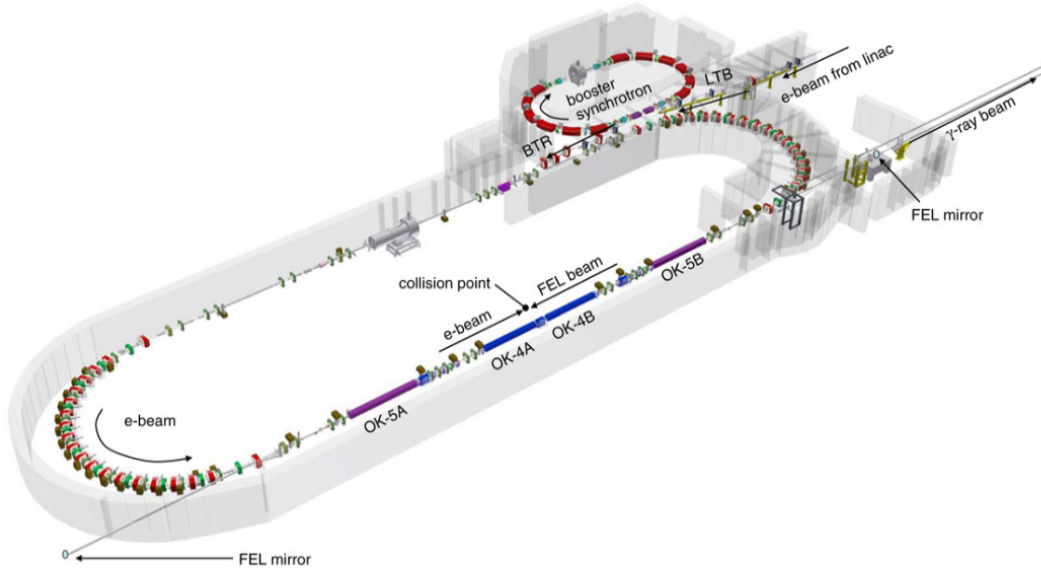


Figure 1.7: Scheme of the  $\gamma$ -beam production system at the HI $\gamma$ S facility. Figure taken from [11]

$\gamma$ -beam in energy range of with high intensity of  $10^9$   $\gamma$ /s and energy resolution of 0.5% RMS would put the facility ahead of any current  $\gamma$ -beam facility.

## 1.6 Charged particle detection

The other prerequisites for studying the  $^{16}\text{O}(\gamma, \alpha)^{12}\text{C}$  reaction is a detector capable of measuring the charged lower energy products of the reaction. A detector aspiring to provide information about E1 and E2 components of the cross-section separately instead of their sum should be capable of measuring the angular distributions of the products which is sensitive for the multipolarity.

The possibilities of measuring the products are defined by their interactions with the detector medium.

### 1.6.1 Stopping power

A charged particle moving through a medium losses its kinetic energy through ionization of the medium. A mean energy loss per path unit in the medium is called a stopping power and can be described by a Bethe-Bloch formula [13]:

$$-\frac{E}{x} = \frac{4\pi e^4 Z_2}{m_e v^2} Z_1^2 \log \left( \frac{2mv^2}{\langle I \rangle} \right) \quad (1.9)$$

where  $Z_1$  is particle atomic number,  $Z_2$  is medium atomic number,  $v$  is particle velocity,  $m_e$  is electron mass,  $m$  is particle mass,  $\langle I \rangle$  is medium's averaged excitation potential per electron, and higher relativistic velocity terms are omitted.

In practice a series of corrections is needed for the formula in order to reproduce the experimental data, therefore a common choice in the nuclear physics community is to

instead use the experimental stopping powers in form of tables provided by Stopping and Range of Ions in Matter (SRIM) [14].

Either the theoretical formula can be integrated in order to obtain the profile of ionizations along the particle path described by a characteristic Bragg. An example Bragg curves for  $\alpha$  particles and  $^{12}\text{C}$  are depicted on Figure 1.8.

The shape of a Bragg curve is characteristic to given ion and medium pair. A Bragg curve can be also reduced to its length in order to provide an energy-range table for given ion and medium pair. The given values describe an average length and the variance in form of length straggling and also angular straggling is often also given or simulated.

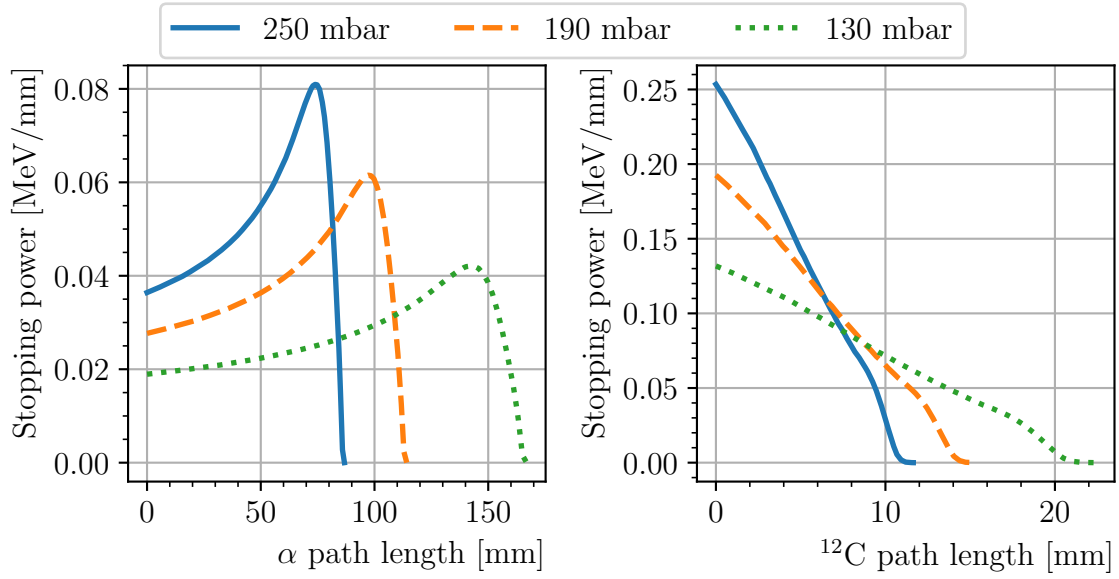


Figure 1.8: Bragg curves for  $\alpha$  particles and  $^{12}\text{C}$  in  $\text{CO}_2$  at 293.15 K. The shape of the curve depends on the ion type, energy, medium and its density. Left: the Bragg curves for an  $\alpha$  particle with kinetic energy of 4.5 MeV. Right: the Bragg curves for  $^{12}\text{C}$  of 1.5 MeV kinetic energy. Data taken from [14].

### 1.6.2 Time projection chambers

A Time Projection Chamber (TPC) [15] is a type of particle detector used in experimental physics to track the paths of charged particles. It operates by detecting the ionization produced when charged particles pass through a gas or liquid medium, and uses this information to reconstruct the particle tracks.

The electric field within the chamber causes the free electrons to drift towards the central electrode, where they are collected and measured by an array of readout sensors. By measuring the position and timing of the ionization events, the TPC can reconstruct the three-dimensional path of the charged particle.

The TPC offers several advantages over other particle detectors. It has high spatial resolution and can track particles over a long distance, allowing it to reconstruct the trajectories of complex particle interactions. It also has excellent particle identification capabilities, as the ionization pattern produced by each particle depends on its mass and charge.

TPC detectors are used in a variety of experiments in nuclear and particle physics, including studies of high-energy collisions and searches for dark matter.

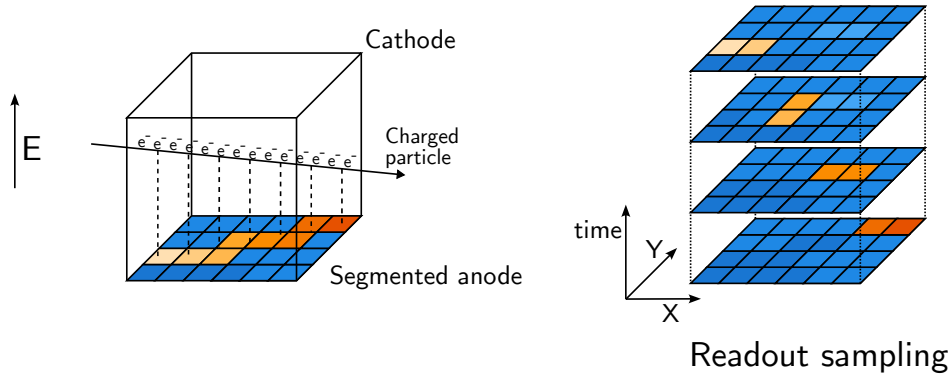


Figure 1.9: TPC principle of operation. A detector medium is being ionized by a passing charged particle. A voltage is applied over the chamber to cause a drift of electrons towards an anode, where the charge is collected. A planar information about the deposited charge is through the anode segmentation. A missing coordinate along the drift axis is obtained through a time sampling of the signal.

### 1.6.3 OTPC

An OTPC is a type of particle detector that combines the principles of a Time Projection Chamber (TPC) with the use of optical readout sensors. The optical sensors are used to record the position and timing of the ionization events. By analyzing the signals from the sensors, the OTPC can reconstruct the three-dimensional path of the charged particle with high precision. A disadvantage of the OTPC is the need of using a medium of scintillating capabilities limiting the list of reactions possible to study.

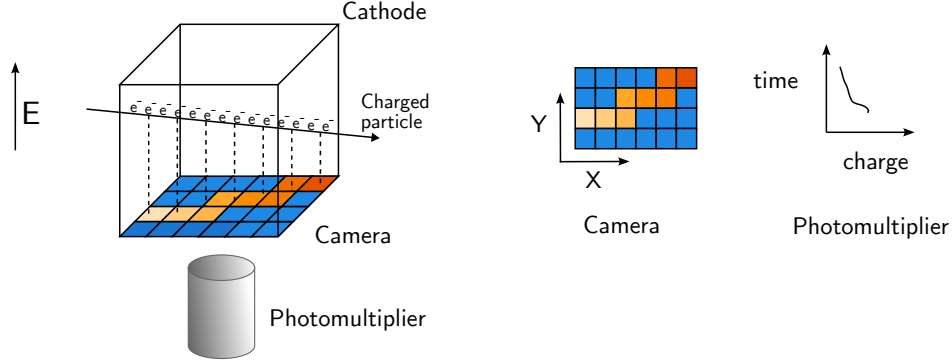


Figure 1.10: OTPC principle of operation. A detector medium is being ionized by a passing charged particle. A voltage is applied to accelerated the electrons and cause a scintillation in the medium. An optical readout system is used. The planar information about the event is obtained with a camera, while the other coordinate is obtained from a photomultiplier signal.

### 1.6.4 e-TPC

Traditionally, TPCs use a readout system based on an array of wires, but electronic readout has become increasingly common in recent years. The electronic readout system provides several advantages over traditional wire-based systems. The use of electronic sensors allows for higher spatial resolution and faster readout times. The sensors are also less susceptible to noise and other sources of interference, improving the signal-to-noise ratio of the detector.

### 1.6.5 Active target detector

In an active target detector a medium filling the detector is used not only for tracking but also as a target. In such detectors there is no ion implantation or injection steps as the reaction occurs inside the detector. This technique allows for the measurement of low energy charged products.

In case of the gaseous active target detectors this pose an interesting trade-off. Higher gas density inside the detector volume would result in higher reaction rate. On the other hand, the higher density causes stronger stopping of the charged reaction products, that results in shorter tracks than may limit the precision of the reconstruction and the measurement. As such the choice of the gaseous mixture plays very important role in the experiment planning.

## 1.7 Author's contribution

This thesis describes the experimental studies of  $^{16}\text{O}(\gamma, \alpha)^{12}\text{C}$  reaction on a  $\gamma$ -beam of HI $\gamma$ S with an active-target TPC WARSAW TPC built at the University of Warsaw.

I actively participated in the laboratory tests of the detector and later in designing and planning of the physical experiments with the detector as well as the data-taking campaigns. I was responsible for the detector control system (slow-control). My work in the post-experiment activities includes pre-processing, reconstruction and analysis of the data.

I'm the author of the calculations and results presented in chapters 4 to 6, if not mentioned differently in the text. I'm also the author of the software system described in appendix C, and one the three major contributors to the software suite presented in appendix D.



# Chapter 2

## Detector

*Now, the era of the photographic plate is over,  
and a new one has begun: that of the bubble  
chamber.*

— Gideon Yekutieli, 1963

The WARSAW TPC is an active-target TPC detector designed and built at the University of Warsaw. The final detector design stems from a decade-long Research and Development (R&D) carried out by the Warsaw TPC [16, 17] collaboration. The collaboration has also built a demonstrator mini-ELITPC detector of similar design [18–20].

The main purpose of the WARSAW TPC detector is studying nuclear reactions with the use of  $\gamma$ -beams with the particular aim at the  $^{16}\text{O}(\gamma, \alpha)^{12}\text{C}$  reaction.

The detector has been operational since March 2020. Two other physics experiments were already successfully carried out with the detector, one with the proton-beam of the Van der Graaf Generator at the IFJ PAN (The Henryk Niewodniczański Institute of Nuclear Physics of the Polish Academy of Sciences) in June 2021 [21] and second with neutron source IGN-14 (pulsed neutron generator) of the IFJ PAN in July, September 2021.

## 2.1 Detector concept

The general cross-view at the WARSAW TPC detector is presented in the Figure 2.1. The outer shell of the detector is a 170 dm<sup>3</sup> stainless steel vacuum vessel equipped with standard vacuum ports, custom signal ports, high voltage ports, two beam windows and radioactive calibration sources.

The vessel was designed to allow operation in pressures lower than the atmospheric pressures, with the typical pressures 80-250 mbar of CO<sub>2</sub>. The signal ports are placed on the top of the chamber where the front-end electronics boards can be mounted.

The frame of the outer vessel can be assembled with wheel-like metal plates to allow for rotation of the whole chamber to make the transportation easier. The WARSAW TPC was meant to be a mobile detector than can be relatively easy to deploy at any desired beam facility.

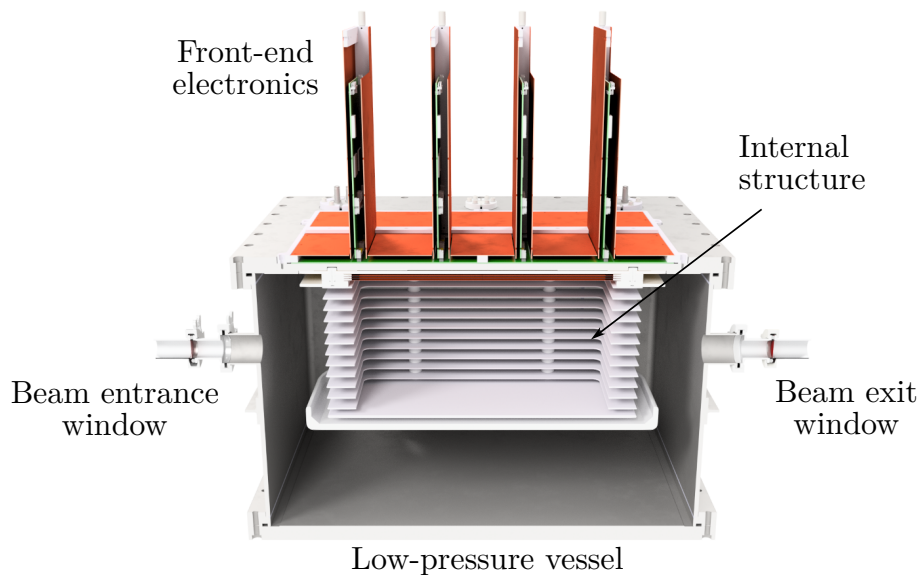


Figure 2.1: WARSAW TPC detector cross-section. The main parts of the detector are vacuum vessel, internal TPC structure and front-end electronics. Scheme taken from [22].

The internal detector structure is depicted in the Figure 2.2 and consists of:

- a drift cage,
- charge amplification micro-pattern,
- segmented electronic readout anode.

The electron drift consists of a 4 mm thick aluminum cathode plate, and 12 aluminum field-shaping 2 mm thick electrodes placed at 16 mm distance from each other. The drift cage achieves a drift uniformity lower than 1% over the entire 196 mm drift length.

While the construction of the chamber allows for up to 196 mm of drift length the actual vertical depth  $l$  that can be registered depends on the electronics time window size  $w$  (buffer history), electronics sampling rate  $\nu_{\text{sampling}}$  and electron drift length  $v_{\text{drift}}$ :

$$l = \frac{w}{\nu_{\text{sampling}}} v_{\text{drift}} \quad (2.1)$$

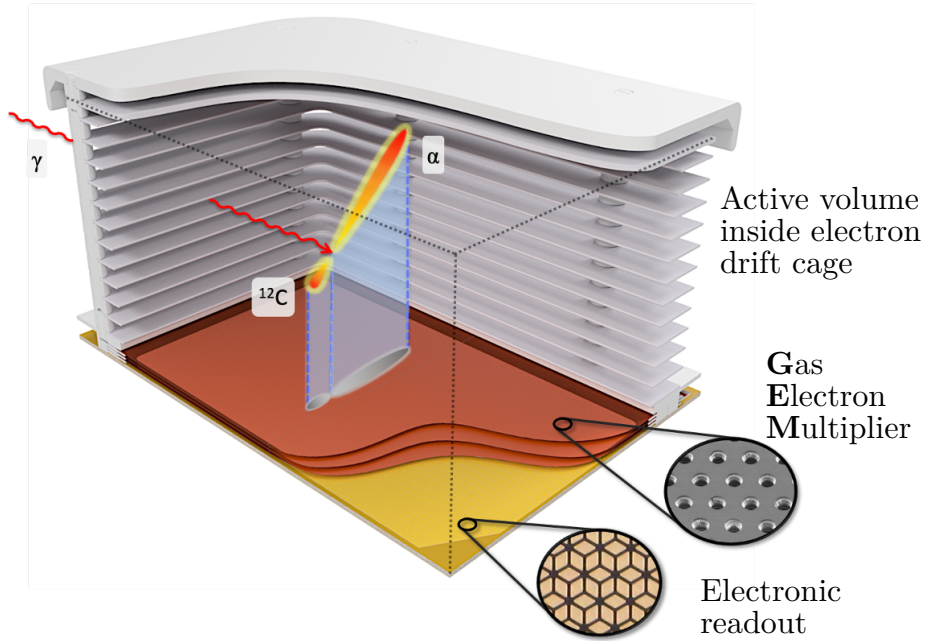


Figure 2.2: Scheme of detector internal structure. Note the detector cage is mounted in the detector with readout at the top (upside-down to orientation that is presented). Scheme taken from [22].

## 2.2 Charge multiplication

With the voltage regime at which a TPC is operating a charge multiplication mechanism has to be employed in order to produce a macroscopic signal that can be later collected by the readout.

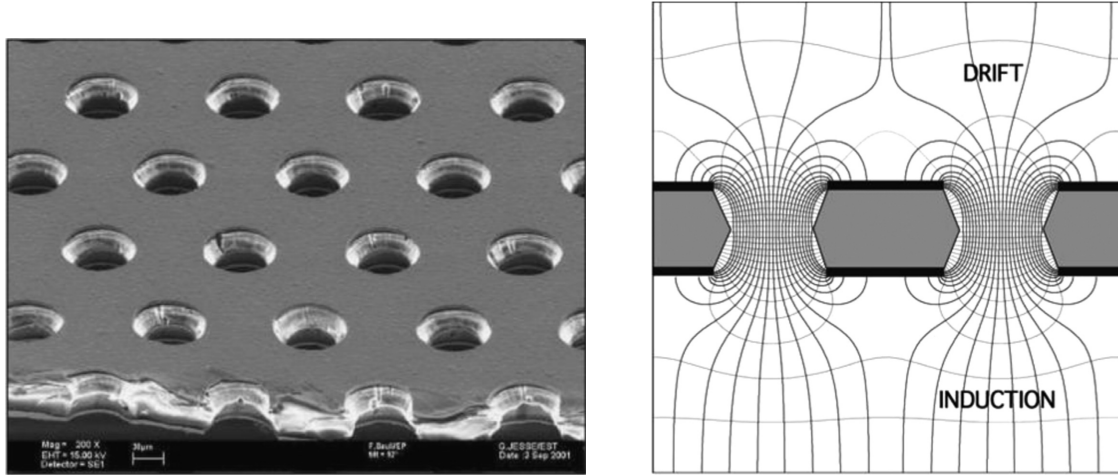


Figure 2.3: Gas Electron Multiplier (GEM) foils. Left: microscopic view on a GEM foil. The hole diameter is  $50\ \mu\text{m}$ . Right: electric field in the region of GEM foil holes. The drift electrons passing through the high field region gain enough energy to cause secondary ionization electrons in the collisions with molecules of the medium. Both pictures taken from [23].

The charge multiplication method of choice for many TPCs is the GEM technology [23]. A photo and principles of operations of the GEM are presented in the Figure 2.3.

The GEM foils are thin kapton (polyimide) foils coated on both sides with copper and perforated. By applying a difference of electrical potential to the sides of the foil a high electric field can be achieved. The order of magnitude for obtained fields is  $\sim 10\ \text{kV/cm}$  that is enough to cause an avalanche charge multiplication.

The WARSAW TPC employs a stack of three GEM foils for the charge amplification. The foils used are  $50\ \mu\text{m}$  thick with  $5\ \mu\text{m}$  of passivated copper coating. The perforation holes have  $50\ \mu\text{m}$  hole diameter, and are staggered with  $140\ \mu\text{m}$  pitch. By placing a stack on the way of the drifting primary ionizations electrons the amplification of the order of  $10^4$  can be achieved leading to macroscopic secondary ionization currents that can be observed on the readout anode.

The optimization of working conditions and operational limits for the WARSAW TPC to achieve stable conditions with high amplification has been studied extensively with both the detector and a dedicated test-bench [17, 19].

## 2.3 Readout board

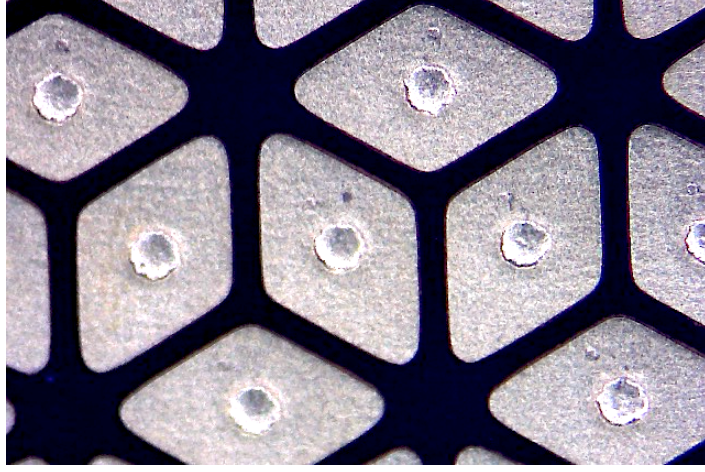


Figure 2.4: Photograph of the readout pads. The top layer of the readout Printed Circuit Board (PCB) is covered with tessellated diamond-shaped gold plated pads. The edges of pads are 1 mm long. Photo by Mikołaj Ćwiok, University of Warsaw.

The active area of the detector is a  $330 \times 200 \text{ mm}^2$  rectangle with corners cut at  $30^\circ$ . The readout board that is collecting the drifting charge is a multilayered PCB covered at the active volume facing side with a pattern of tessellated diamond gold-plated pads. The photograph of the readout pads is presented in the Figure 2.4.

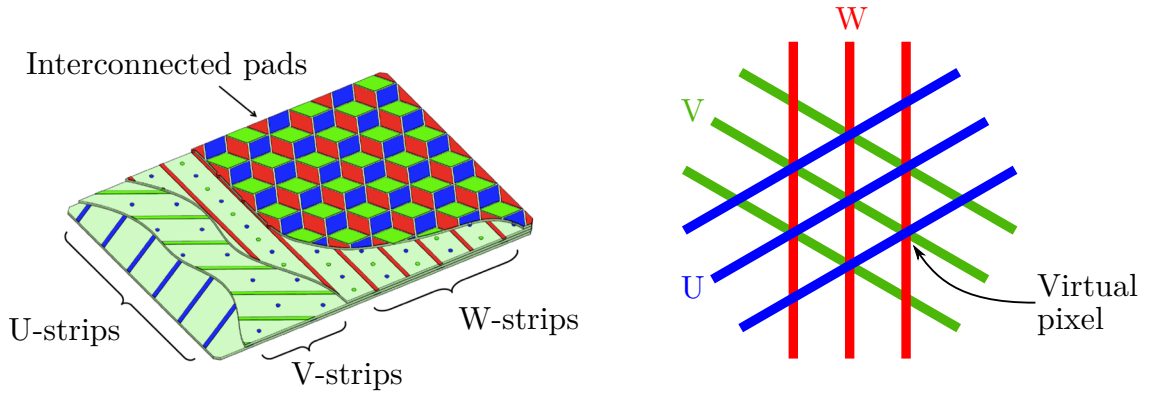


Figure 2.5: Structure of WARSAW TPC readout board. Left: the top layer diamond-shape pads are connected by underlying U, V, W-readout strips. The colour of a pad matches the colour of strip group connected to it (U — blue, V — green, W — red). The ionization electrons are collected by a pad. The strip reads charge from all the pads connected to it at once. Right: the position of event can be determined by comparison of signals from different strip-groups (U, V, W). The intersections between these strips form virtual pixels. The usage of 3 strip coordinates eliminates the ambiguity of strip mapping caused by double hit events.

The readout pads are interconnected in a pattern of lines arranged at  $60^\circ$  to each other, forming a structure of strips. The strips are organized in three families (U, V, W) depending on their direction with a 1.5 mm pitch between strips of a given family. The pattern of readout strips is presented in the Figure 2.5. A crossings of the strips from all three families creates a virtual pixels, that could be used to find a location of a single charge deposit. While the virtual pixels could be created as a crossings of strips of only two families the addition of the third strip family helps in disambiguation of multiple deposits.

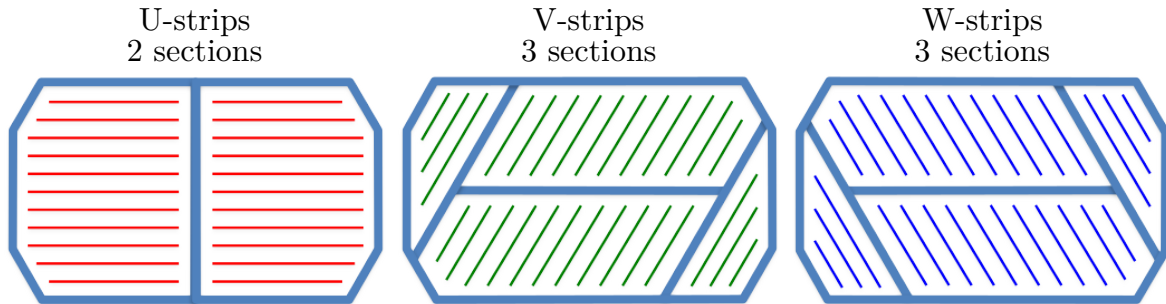


Figure 2.6: Readout strip sections. Some of the strips are splitted into two in order to achieve better deposit disambiguation. The strips that are not splitted are considered to form a single section. Scheme by Mikołaj Ćwiok, University of Warsaw.

Table 2.1: Number of readout strips for each family including the strip sections.

Direction	Total	Section	Strips
U	264	1	132
		2	132
V	376	0	72
		1	151
		2	151
W	378	0	72
		1	152
		2	152

To further increase the multiple deposit disambiguation part of the strips is split in into two forming strip sections. The shape of the strip section on the readout board is presented in the Figure 2.6 and the exact sizes of sections are listed in Table 2.1. Each strip in a section is routed to a separate electronic channel.

The strip readout is a modernization of the concept of wires used in the wire chambers detectors of the past [24] and still used in the TPCs [25]. While the wires has been replaced with the pads of the PCB the geometrical concept remains the same: a set of two or more longitudinal structures that measure only the projection on their axis is used to decipher a 3D event. A coordinate system UVW inherited from the readout segmentation is discussed in Appendix B.

The use of a strip readout is a compromise between covering the active using as few electronic channels as possible and allowing a high spatial precision by strong segmentation. This tradeoff limits the possible usage to events involving only a few charged particles — a rather typical situation in low energy nuclear physics. The strip readout is just one of the possible ways to accomplished that goal — not long ago a new multiplexing readout [26] has been proposed to address the same problem.

While the strip readout is a fairly cost-effective solution when compared to a pixel readout, it is worth mentioning that the reconstruction of strip data is significantly more complicated than in a case of a pixel readout and the additional cost of software-development shouldn't be neglected in the equation. Similarly the extra disambiguation features included in the design do not increase the disambiguation on they own and have to be additionally implemented in the reconstruction and analysis software. For instance the extra engineering effort done on splitting the strips in sections and raising the total number of electronic channels required to operate the system would be futile if the reconstruction is using a simplified model with merged sections.

## 2.4 DAQ system

Data acquisition (DAQ) is a process of collecting and recording the physical data from the sensors and detectors and as such is the essential part of every experiment. In nuclear physics and High Energy Physics (HEP) the DAQ term usually refers to the detectors that measure the data of physical importance (such as the main detector of the experiment measuring the reaction or an auxiliary detector monitoring the physical background), while all the supporting sensors are grouped together in the so-called “slow-control” or Detector Control System (DCS) (Appendix C).

### 2.4.1 Readout chain

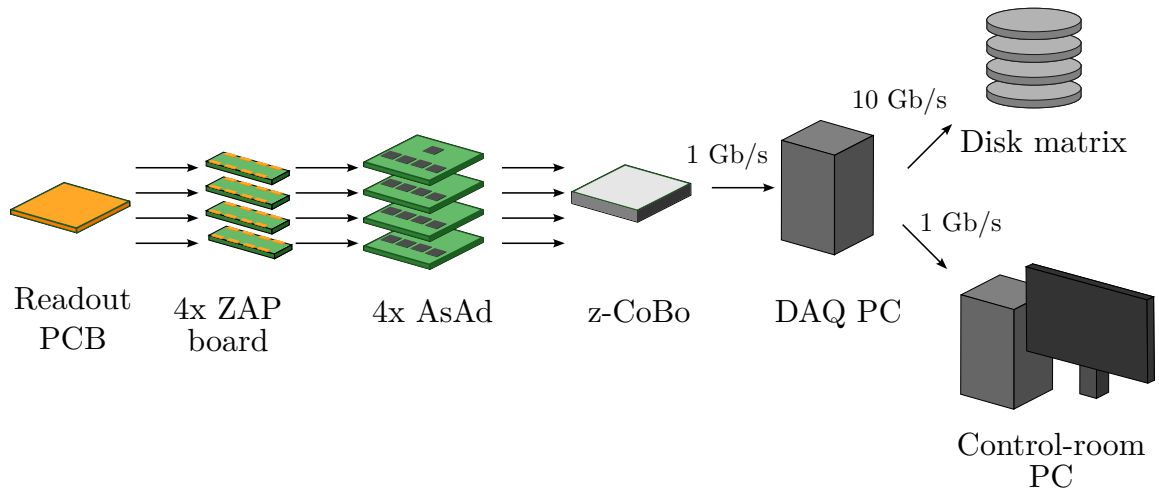


Figure 2.7: DAQ readout chain scheme.

The WARSAW TPC DAQ system is based on the General Electronics for TPCs (GET) system [27]. The GET based systems are used by other TPC groups such as ACTAR [28], AT-TPC [29], TexAT [30], S $\pi$ RIT [31]. The readout consist of multiple components that are either available of-shelf or designed at the University of Warsaw. The readout chain used by the WARSAW TPC is presented in the Figure 2.7.

### 2.4.2 GET based components

While the GET provides multiple boards and components the factors such as final required number of channels, total price of the setup and design flexibility ruled out that in place of the full system a so-called reduced GET system limited to just ASIC & ADC (AsAd)s and Concentrator Board (CoBo) is more appropriate.

#### ZAP

A signal protection circuit boards called ZAP are recommended by the GET. A ZAP board houses external pre-amplifiers and analog filters, and its role is to route the signals from the detector to the front-end electronics. Since the ZAP board are supposed to serve as an interface for the particular detector and subsequent generic front-end electronics, there is no universal ZAP design. The ZAP boards for the WARSAW TPC has been designed and built at the University of Warsaw.

#### AsAd

An AsAd board is the critical readout electronics component used in the DAQ chains of the TPCs basing on the GET. The boards are manufactured by the GET collaboration and available off-shelf.

A single AsAd board is capable of delivering 256 electronic channels. Each board houses a Field-Programmable Gate Array (FPGA) (ACTEL ProASIC3E), four ASIC for GET (AGET) chips and a 4-channel 12-bit Analog-to-Digital Converter (ADC) operating at 25 MHz.

An AGET chip provides 64 electronic channels and is featuring:

- both negative and positive input handling,
- per channel Charge Sensitive pre-Amplifier (CSA) with dynamic range of 120 fC, 240 fC, 1 pC, and 10 pC,
- variable shaping time amplifier in range 50 ns–1  $\mu$ s,
- 512 bin Switched Capacitor Array (SCA) in form of analog circular buffer with variable sampling frequency in range 1–100 MHz.

The AGET can be configured in either full readout mode(dense data representation) or partial readout (sparse data representation) mode. In case of WARSAW TPC only full readout mode has been used so far.

A total of 4 AsAd boards resulting in over a thousand available electronic channels are used with the WARSAW TPC. The size of a single event in 4-AsAds full readout mode is approximately 1.1 MB.



## z-CoBo

A CoBo is a back-end electronics board designed by GET. The purpose of the boards is performing data reduction, time stamping and formatting over data provided from the AsAd boards and transferring it to a DAQ PC. It is also capable of configuring and calibrating AsAds.

The z-COBO is a CoBo replacement designed by the University of Warsaw. The platform employs an FPGA Xilinx ZYNQ-7000 System-on-Chip (SoC) module and four AsAd adapters. The platform handles up to 1024 electronic channels and allows to read between 1 and 4 AsAds via 10 Gbit/s SFP+ links. The module fits into two units (2U) of a standard 19" rack.

## 2.4.3 DAQ PC

### Specification

The main DAQ PC of the WARSAW TPC is a Supermicro ST Single E5 SC732 (MOBO Supermicro X10SRL-F). The computer is equipped with:

- Central Processing Unit (CPU): single Intel Xeon E5-1620 V4 processor @ 3.8 GHz (4 cores, 8 threads),
- Random-Access Memory (RAM): 2x 16 GB DDR4 REG ECC 2400 MHz,
- Graphics Processing Unit (GPU): Gigabyte GeForce GTX 1050 Ti 4 GB GDDR5,
- Network Interface Card (NIC):
  - Supermicro AOC-STGN-i1S, 1xSFP+ 10 Gbit/s,
  - Supermicro AOC-STGN-i2S, 2xSFP+ 10 Gbit/s,
  - Intel Gigabit Pro/1000 CT 1 Gbit/s,
- Storage:
  - 4x 3 TB Hard Drive Disk (HDD) configured in a RAID<sup>1</sup> 5 and RAID 6 - used for data storage (RAID 5) and boot (RAID 6).
  - 2x 256 GB Solid-State Disk (SSD) configured in a RAID 1 - used for system and temporary user data (scratch).

and operates an Ubuntu 16.04 LTS with Xfce4 desktop environment (Linux).

In the case of WARSAW TPC the role of the main DAQ PC has been extended to:

- hot data storage - the data received from the z-COBO is temporary saved on the local storage and later transferred to a dedicated storage,

---

<sup>1</sup>Redundant Array of Independent Disks - a data storage technology that combines several disk in to logical units in order to achieve both data redundancy (mitigation of data-loss in case of a disk failure) or performance improvements. The RAID number signify the exact configuration. Different RAID configuration requires different minimal number of physical disks required and provide different levels of redundancy and performance improvements.

- online analysis - a user space for running online data analysis is provided,
- main DCS PC - the same computer unit is used to host all the service and data associated with the DCS,
- electronic logbook [32] server - beside the classical paper notebook an additional electronic web-interfaced version is used,
- auxiliary detector DAQ - the same computer unit hosts and handles DAQ not only from the main TPC chamber but also beam and trigger monitoring.

The system operates without a software hypervisor - all the applications and services are run directly on the operational system with the exception for Windows-only auxiliary detector DAQ applications that are run on a Virtual Machine (VM).

### **DAQ software**

The main software DAQ components are `dataRouter` and `GetController` from the GET software package. The main purpose of these applications is communication with the z-CoBo and receiving the data. In addition a dedicated on-line event preview application has been written (as a part of TPCReco package discussed in Appendix D).

#### **2.4.4 Control room PC**

The Control room PC acts as a terminal and display for the DAQ PC when it can't be accessed directly due to residing at the experimental hall. The PC is not expected to run any compute intensive workloads, so there are little constraints on the specification of the used platform.

Since only some of the services and applications hosted on the DAQ PC follow the client-server model with either web or native interfaces, all the required applications are run on the DAQ PC including their client parts. Then a Control room PC accesses whole virtual session run on DAQ PC using the Virtual Network Computing (VNC) technology.

A number of desktops and laptops has been already used to fulfil the role of the Control room PC.

### 2.4.5 Storage

The storage system includes two disk matrices:

1. QNAP TS-831X equipped with 4x 3 TB HDD, 4x 10 TB HDD,
2. QNAP TES-1885U-D1521-8GR equipped with 12x 12 TB HDD.

The QNAP TS-831X is brought to the experiments and part of the DAQ chain. The QNAP TES-1885U-D1521-8GR acts as a permanent storage, while not accessed directly as part of the DAQ all the data is transferred to it eventually after finishing the experiment. It provides the data for offline post-experiment analysis. All the utilized hard drives are either Network Attached Storage (NAS) or data center grade.

## 2.5 Online Trigger

The online trigger is a crucial element of a DAQ system in nuclear physics and HEP experiments. It plays a fundamental role in selecting which events to record and store for further reconstruction and analysis, as the rate of data produced in experiments is often high. While saving the amount of work needed at the later stages to retrieve any relevant information and reduce the size of the dataset to be kept, the most fundamental need of the selection is to lessen the load on the system as the slower parts at the end of the DAQ chain may not be able to keep up with the stream of incoming unfiltered data.

The trigger system's main purpose is to decide which events are worth recording based on predefined criteria. The criteria can vary greatly from the experiment to experiment and they can range from a threshold on some analog signal to a complex set of rules implemented on a Application-Specific Integrated Circuit (ASIC) or FPGA.

### 2.5.1 Trigger-modes

The detector is capable of two modes of triggering:

1. External trigger - external signal correlated to the beam is provided to the DAQ trigger input.
2. Self-trigger - signal from the last GEM electrode is processed with a High Voltage (HV) filter and fed to the DAQ electronics trigger input. In this mode the trigger is independent of the beam time structure and could be used for experiments with continuous beams or in facilities not providing the trigger signal or even in potential beamless experiments.

The scheme of both external and self-trigger is presented in the Figure 2.8.

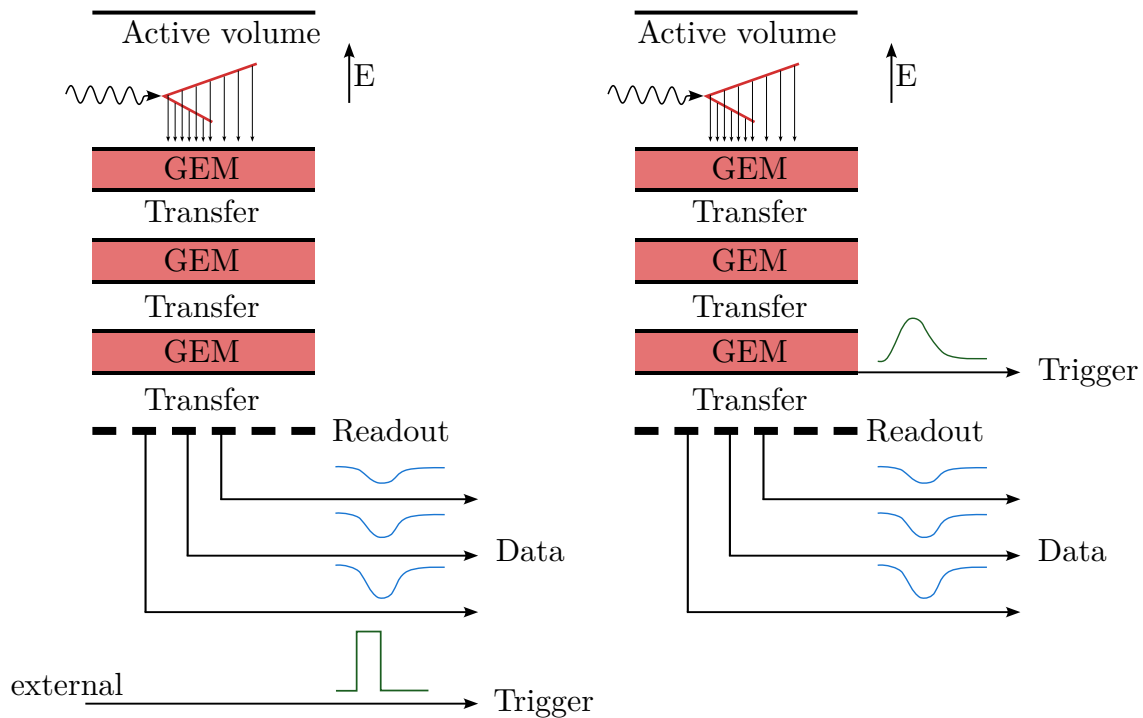


Figure 2.8: Trigger scheme. Two trigger modes available for WARSAW TPC are depicted. Left: external trigger. An external signal correlated with the beam is provided by the beam facility and fed on DAQ electronics trigger input. Right: self-trigger. Signal from the last GEM is used as a trigger. The signal on the GEM is caused by ionization electrons drifting towards the readout and being multiplied at the GEM.

The choice of triggering mode is based on the capabilities of a beam facility and the type of beam. For instance for continuous or semi-continuous the facility will not provide an external trigger, but for pulsed beam a beam release signal can be used for external trigger.

If possible the external triggering is preferable as it is able to remove all the background events not associated with the beam such as natural radiation. The other important consequence is that the start of trigger signal can be used as a origin of the drift axis in order to obtain an absolute scale (for instance the absolute position of a vertex in active volume). In self-trigger mode establishing the absolute scale on the drift axis is not possible and only relative distances can be measured (for instance the relative distance along the drift axis between endpoint and vertex). Comparison of the drift axis scales for both modes of triggering is presented in the Figure 2.9.

As a side note both triggering modes of WARSAW TPC from a DAQ electronics point of view could be considered an external trigger since the data and trigger signal are provided on two separate inputs. An internal trigger model fully built in the DAQ electronics and relying only on the stream of data without any kind of external input is being developed at the University of Warsaw as an upgrade to the detector.

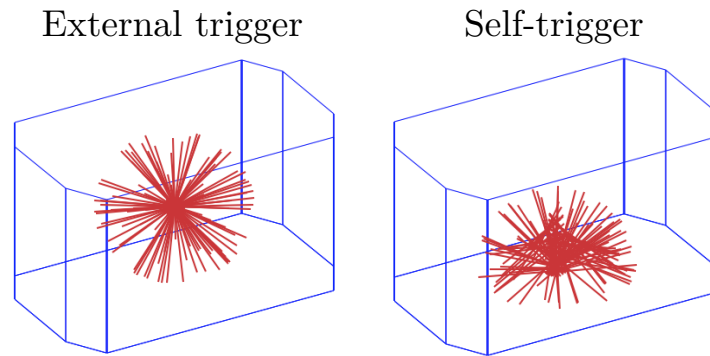


Figure 2.9: Trigger mode effects on the drift axis coordinate determination presented on a simulation data. A series of events originating uniformly for the center of chamber were simulated. Each line represents a different event. Left: external trigger. Absolute event position along the drift axis can be determined. Right: self-trigger. The information about the event absolute position along the drift axis is lost. Only relative positions along the drift axis can be measured (such as position of track endpoint with respect to the vertex). Simulation by Mikołaj Ćwiok, University of Warsaw.



# Chapter 3

## Experiment

In the 2022 an experiment was conducted with the WARSAW TPC the and  $\gamma$ -beams of the HI $\gamma$ S at the TUNL in Durham, NC, USA. The experiment was split into two campaign first in April 2022 and the other in August–September 2022. A photograph of the detector at during the experiment is presented in the Figure 3.1.



Figure 3.1: A photograph of WARSAW TPC detector and its setup during the experiment at the Upper Target Room (UTR) at HI $\gamma$ S in April 2023. The parts depicted at the photo are the WARSAW TPC detector, detector stand, and a rack full of experimental equipment. Photo by Mikołaj Ćwiok, University of Warsaw.

Note the convention of use of  $\gamma$ -beam beam nominal energy  $E_\gamma$  as a human readable run identifier. The exact value of the beam delivered may differ slightly from the nominal one and was measured during the experiment.

### 3.1 Overview

The main goal of the experiment was the measurement of the  $^{16}\text{O}(\gamma, \alpha)^{12}\text{C}$  cross-section for low-energies for multipolarities E1 and E2 with the  $\gamma$ -beam of the HI $\gamma$ S. The main detector of the experiment was the WARSAW TPC/ operating with low-pressure  $\text{CO}_2$  in order to measure the low-energy reaction products. The experiment worked also as the final confirmation of the WarsawTPC as a tool for studying the  $\gamma$ -beam induced nuclear reactions.

The detector was placed in the UTR at the HI $\gamma$ S. A various set of auxiliary detectors was used to measure and monitor to properties of the  $\gamma$ -beam. A scheme of the experimental setup is depicted in the Figure 3.2. A high purity  $\text{CO}_2$  of natural isotopic abundance was used as the TPC medium.

The reaction cross-sections were scanned with a set of  $\gamma$ -beam energies with the nominal energies  $E_\gamma$  ranging from 13.9 MeV to 8.51 MeV. The list of scanned energies with total allocated times and estimated average  $\gamma$ -beam intensity is presented in Table 3.1. The experimental points were marked on the S-factor plot [1] in the Figure 3.3 in order to visually signify the energy regions investigated in the study.

The  $\gamma$ -beam delivered to the UTR has been collimated with a lead collimator with 10.5 mm diameter and 15 cm width located approximately 10 m before the chamber and around 60 m after the  $\gamma$ -beam origin point.

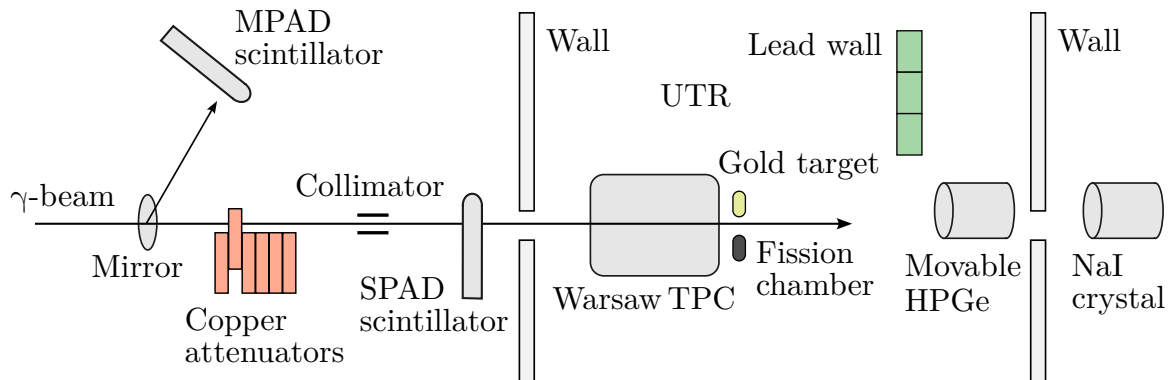


Figure 3.2: Scheme of experimental setup. The WARSAW TPC is placed in the UTR with a various other auxiliary detector for measuring and monitoring beam properties such as energy (HPGe), absolute intensity (NaI, gold targets, fission chambers). The  $\gamma$ -beam is passed to the UTR by a 10.5 mm collimator. The beam relative intensities can be monitored by scintillator detectors (MPAD, SPAD). A set of six copper-attenuators may be used to attenuate the beam as the full intensity is too high for some of the detectors.



Table 3.1: Beam energies  $E_\gamma$  investigated with corresponding center of mass energies for the  $^{16}\text{O}(\gamma, \alpha)^{12}\text{C}$  during the experiment. Total time allocated for experimental point  $t$  and estimated average  $\gamma$ -beam intensity  $I_\gamma$  are given. The intensities were estimated with an online calibration for the beam-monitoring system.

April campaign				August campaign			
$E_\gamma$ (MeV)	$E_{\text{CM}}$ (MeV)	$t$ (h)	$I_\gamma$ ( $10^8 \frac{\gamma}{\text{s}}$ )	$E_\gamma$ (MeV)	$E_{\text{CM}}$ (MeV)	$t$ (h)	$I_\gamma$ ( $10^8 \frac{\gamma}{\text{s}}$ )
13.9	6.7	4.4	1.7	9.85	2.70	1.0	4.3
13.5	6.3	3.6	1.5	9.56	2.40	2.5	3.9
13.1	5.9	3.0	1.5	9.36	2.20	4.0	4.1
12.7	5.5	2.0	1.4	9.16	2.00	13.0	4.2
12.3	5.1	1.4	1.3	8.86	1.70	49.5	3.9
11.9	4.7	4.2	1.9	8.66	1.50	89.0	3.8
11.5	4.3	4.0	1.8	8.51	1.35	28.5	4.5
11.1	3.9	6.0	2.0				
9.85	2.70	9.4	2.0				
9.56	2.40	11.4	1.9				

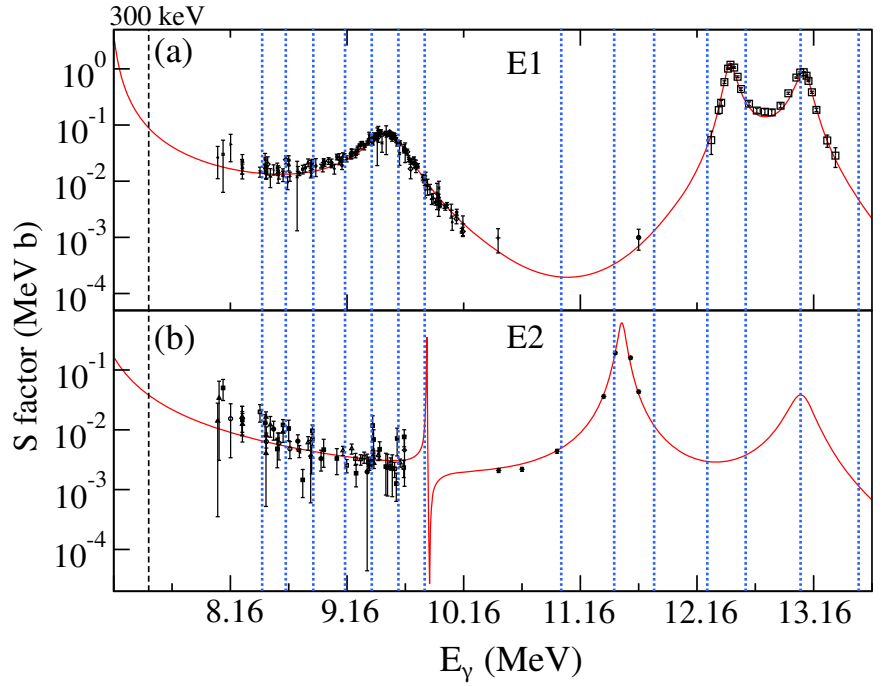


Figure 3.3: Experimental points. Note the OX axis is energy of  $\gamma$ -beam in the LAB reference frame. The S-factor figure taken from [1].

The experiment was accomplished in the full scale without any major problems. A total size of over 4 TB experimental was secured. The number of events registered (accepted by the trigger and saved on the disks) for each experimental point are listed in Table 3.2.

Table 3.2: Total number of events measured for each energy during the experiment. The total size of data is 4.03 TB. The numbers of events are listed without applying any cuts, selections or filters.

Total number of events		Total number of events	
$E_\gamma$ (MeV)		$E_\gamma$ (MeV)	
13.9	528264	9.85	88446
13.5	567720	9.56	33690
13.1	613327	9.36	57530
12.7	314338	9.16	63967
12.3	253922	8.86	186686
11.9	168188	8.66	238385
11.5	247699	8.51	54910
11.1	159783		

## 3.2 Background

Being aware of the possible background reactions is an important step of planning an experiment. Depending on the techniques used during the reconstruction and analyzes differentiating between the background and signal reaction might be not possible or require significant effort. A background reactions with a very high cross-section a given energy can — if not filtered out by an online trigger — dominate and overfeed the DAQ system rendering other measurements impossible.

With the choice of  $\text{CO}_2$  a number of background beam-induced reaction are possible. In particular the  $(\gamma, \alpha)$ ,  $(\gamma, n)$ ,  $(\gamma, p)$  on the naturally occurring isotopes of C and O are expected. In order to predict the occurrence of given reaction its separation energy or heat should be compared with the available energy. The separation energies of possible reactions induced on the nuclei from the  $\text{CO}_2$  are listed in Table 3.3. The separation energies are also depicted in the Figure 3.4 with a visual representation of the energy ordering.

Table 3.3: Separation energies of neutrons,  $\alpha$  particles and protons in  $^{12,13}\text{C}$  and  $^{16,17,18}\text{O}$ . The values taken from [33].

	$^{12}\text{C}$	$^{13}\text{C}$	$^{16}\text{O}$	$^{17}\text{O}$	$^{18}\text{O}$
$S_n$ (MeV)	8.722	4.946	15.664	4.144	8.044
$S_\alpha$ (MeV)	7.367	10.648	7.162	6.359	6.227
$S_p$ (MeV)	15.957	17.533	12.128	13.780	15.942

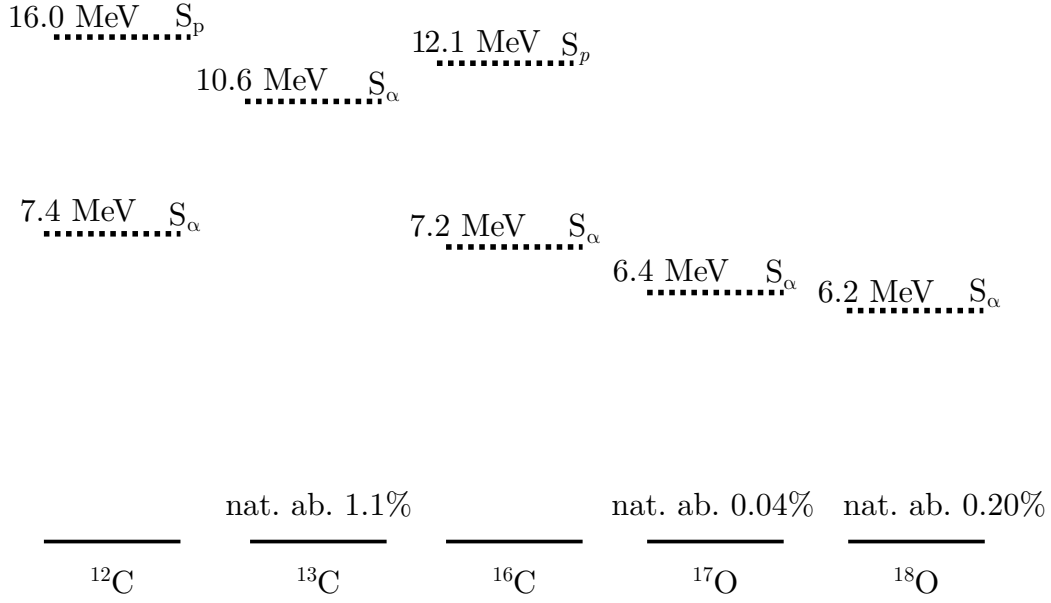


Figure 3.4: Separation energies in the naturally occurring isotopes of C and O.

An additional background might be detected by the recoils produced in the  $(\gamma, n)$  reactions, as well as inelastic scatterings. Beside the beam-induced background the TPC is subject of detecting the  $\alpha$  particle background from the vacuum vessel construction. The estimated trigger rate of this background is 0.2 Hz.

While the mentioned reactions are considered as a background for the investigated  $^{16}\text{O}(\gamma, \alpha)^{12}\text{C}$  some of them like  $^{12}\text{C}(\gamma, 3\alpha)$  pose an interesting research material on their own [34, 35].

Another notable background reaction is the  $^{16}\text{O}(\gamma, p)^{15}\text{N}$  that can be observed for experimental runs characterized by excitation energy above the proton separation  $E_x > S_p$  (in practice  $E_\gamma \in \{12.3, 12.7, 13.1, 13.5, 13.9 \text{ MeV}\}$ ). The reaction produces two ions that could be detected by the detector and it is connected by a detail balance principle to  $^{15}\text{N}(p, \gamma)^{16}\text{O}$  with a well known cross-sections [36], making the  $^{16}\text{O}(\gamma, p)^{15}\text{N}$  reaction a good candidate for a source of additional reaction rate calibration.

### 3.3 TPC configuration

The WARSAW TPC working points and DAQ configurations were optimized for each energy to allow for detection of particles of predicted energies. In particular three sets of pressures were used: 250, 190 and 130 mbar. For every pressure the HV applied to internal active structure were adjusted to obtain stable conditions with high charge multiplication.

The value of electronic sampling was tuned in accordance with the drift velocity to obtained recording depth allowing for measurements of vertical tracks of a length estimated for given energies. The list of settings used for every energy run is presented in Table 3.3. All the experimental runs were collected with the setting of GET electronics of 120 fC range and 232 ns shaping constant time. A trigger delay setting was used to record the triggering moment in approximately 10% of the available event time-window.

Table 3.4: TPC settings used during the experiment. For all the experimental runs the DAQ has been operating with the dynamic range o 120 fC and shaping time constant of 232 ns.

	Campaign	Pressure (mbar)	Sampling rate (MHz)	Drift velocity (cm/ $\mu$ s)	TPC Depth (mm)
$E_\gamma$ (MeV)					
13.9	Apr	250	12.5	0.405	150
13.5	Apr	250	12.5	0.405	150
13.1	Apr	250	12.5	0.405	150
13.1	Apr	190	25.0	0.762	141
12.7	Apr	190	25.0	0.704	130
12.3	Apr	190	25.0	0.646	119
11.9	Apr	190	25.0	0.646	119
11.5	Apr	190	25.0	0.646	119
11.1	Apr	190	25.0	0.646	119
9.85	Aug	130	25.0	0.500	92
9.85	Apr	130	25.0	0.500	92
9.56	Aug	130	25.0	0.500	92
9.36	Aug	130	25.0	0.500	92
9.16	Aug	130	25.0	0.445	82
8.86	Apr	130	25.0	0.500	92
8.86	Apr	130	25.0	0.390	72
8.86	Aug	130	25.0	0.390	72
8.66	Aug	130	25.0	0.390	72
8.51	Aug	130	25.0	0.390	72

## 3.4 $\gamma$ -beam monitoring

### 3.4.1 Alignment

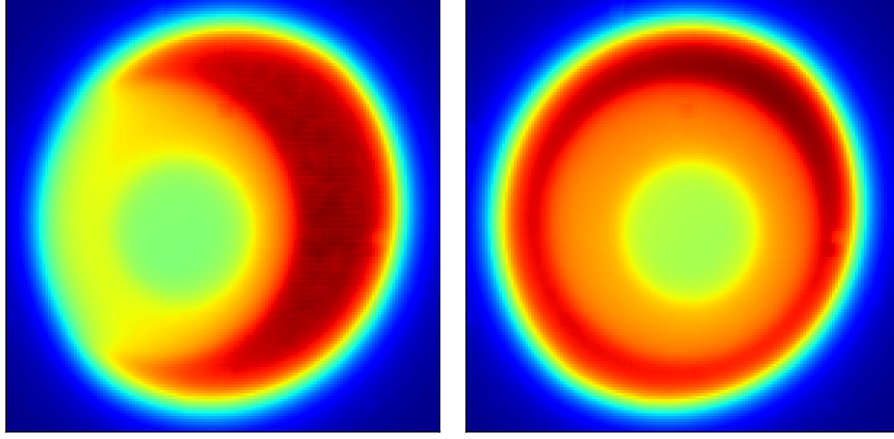


Figure 3.5: Beam alignment with BGO  $\gamma$ -camera. Left: beam misaligned with the collimator. Right: beam aligned with the collimator. In the center the shadow of the lead plugs placed in the detector ports. The misplacement of the shadows from the center measures the beam misalignment.

The chamber has been positioned according to a visible laser level system. Then the beam alignment was assessed with a BGO  $\gamma$ -camera in order to adjust the chamber. Two lead plugs were placed at the detector front and back ports of the detector, the  $\gamma$ -camera was placed after the detector on the beam-line and then the beam was launched. After stopping the beam and collecting the feedback the detector position was adjusted. The process has been repeated until satisfactory result has been achieved. The Figure 3.5 depicts the alignment data from the  $\gamma$ -camera.

The vertical position of the detector was adjusted to allow the  $\gamma$ -beam to pass between the electrodes in order to avoid generating additional background.

### 3.4.2 Beam energy monitoring

The  $\gamma$ -beam spectra were measured with a HPGe detector placed in the UTR on the beam line after WARSAW TPC. Due to the specifics of HPGe allowing it to work only with relatively low beam intensities of a few kHz, the HPGe couldn't be used online during the experimental runs with the TPC.

As such the HPGe had been covered behind a lead wall for the duration of experimental runs and the beam energy measurements had to be realized separately. During the energy spectrum measurements the HPGe was located approximately 4 m after the chamber with the center of the HPGe misaligned with the beam axis by 4 mm.

During the beam energy measurements the beam had been attenuated with a set of six copper attenuators (2.45, 4.9, 8.0, 8.0, 8.0, and 8.0 cm thick).

### 3.4.3 Beam intensity

#### Absolute intensity measurement

For the absolute calibration a large NaI crystal detector was used. Similarly to the HPGe the detector can operate only at lower beam intensities and measuring along the TPC was not possible. The measurements of the absolute has been conducted again using the five beam attenuators with known thickness and attenuation factors.

Moreover during the August campaign as an independent source of absolute intensity measurement seven gold targets of known dimensions have been placed on the beam line directly after the WARSAW TPC. A single target has been exposed to the  $\gamma$ -beam for a duration of an experimental run for each  $\gamma$ -beam energy setting. The decay measurements were performed at the low-background laboratory located in the TUNL.

In addition for a selected experimental run during the August campaign two  $^{235}\text{U}$  fission chambers were mounted at the end of the WARSAW TPC in order to provide another estimate of the absolute beam intensity.

#### Relative intensity measurement

In order to extract the absolute cross-section as well as monitor the beam stability, the beam intensity should be measured online during the experimental runs. The relative beam intensity measurements don't require the beam attenuation and can be made concurrently with the experimental runs making them ideal for the task. Their disadvantage is the requirement of calibrating them with an absolute intensity detector.

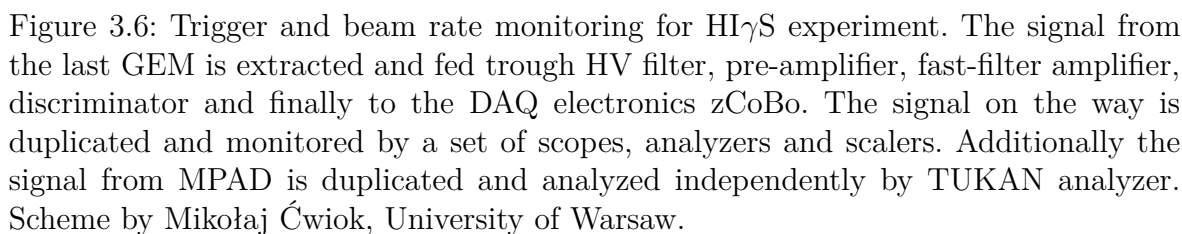
For the relative intensity determination two plastic paddle scintillators coupled with photomultiplier tubes (PMT) were used. The first Mirror Paddle Detector (MPAD) was monitoring the intensity of  $\gamma$ -beam Compton-scattered under  $40\text{--}50^\circ$  on the FEL mirror before 10.5 mm collimator, the other Single Paddle Detector (SPAD) on the beam line after the collimator.

## 3.5 Online trigger & electronics

During the experiment the WARSAW TPC was operating in self triggering mode with the signal from the last GEM acting as the trigger. The extracted signal was first filtered with a HV filter (type C) and then fed through a pre-amplifier and fast-filter amplifier to the discriminator and finally to the zCoBo.

The events above the discriminator threshold are activating the trigger. The scheme of used trigger is depicted in the Figure 3.6. The value of the discriminator was establish for every unique GEM amplification point in order to minimize the contribution of electronic noise. The obtained signal was monitored by a number of scalers, scopes and analyzers both during the tests of setup installation as well as online during the experimental runs. The data from analyzers was stored for offline analysis.

Additionally in order to have a separate beam intensity online-preview independent of the HI $\gamma$ S DAQ, the signal from MPAD was duplicated and recorded by a TUKAN analyzer [37].







# Chapter 4

## Reconstruction

The event reconstruction is a step in which the low-level measured data is being transformed into collection of high-level variables usually with a physical interpretation. A typical example of event reconstruction is identifying the particles and their momenta based on a photo of tracks left in a bubble chamber.

Since the algorithms used to transform the data can vary greatly depending on the problem, there is no universal expectation on the high-level output variables quantities. For instance some reconstruction algorithms may produce the particle identification, energy, momenta and positions while other may produce only the positions and rely on statistical analysis to calculate other quantities of interest.

The common aspect of all the reconstructions algorithms is the data reduction.

To support the technical aspect of the event reconstruction from the WARSAW TPC data a dedicated software package called TPCReco has been written (Appendix D).

### 4.1 Data preprocessing

#### 4.1.1 Waveform corrections

As the WARSAW TPC DAQ system is based on GET [27] the data processing starts with waveform correction pipeline specific to the GET-based systems [38], although not every step has been implemented yet for the WARSAW TPC pipeline.

An example uncorrected electronic waveform from a single electronic channel is depicted in the Figure 4.1. The features of the waveform that might negatively impact the data and should be corrected are:

- relatively high noise,
- non-flat baseline shape,
- extreme values at the beginning and end of the recorded window.

The features identified for a single channel are typical and observed for other channels, as depicted in the Figure 4.2. In addition a need for another correction has been noted as the average baseline value seem to vary across different channels.

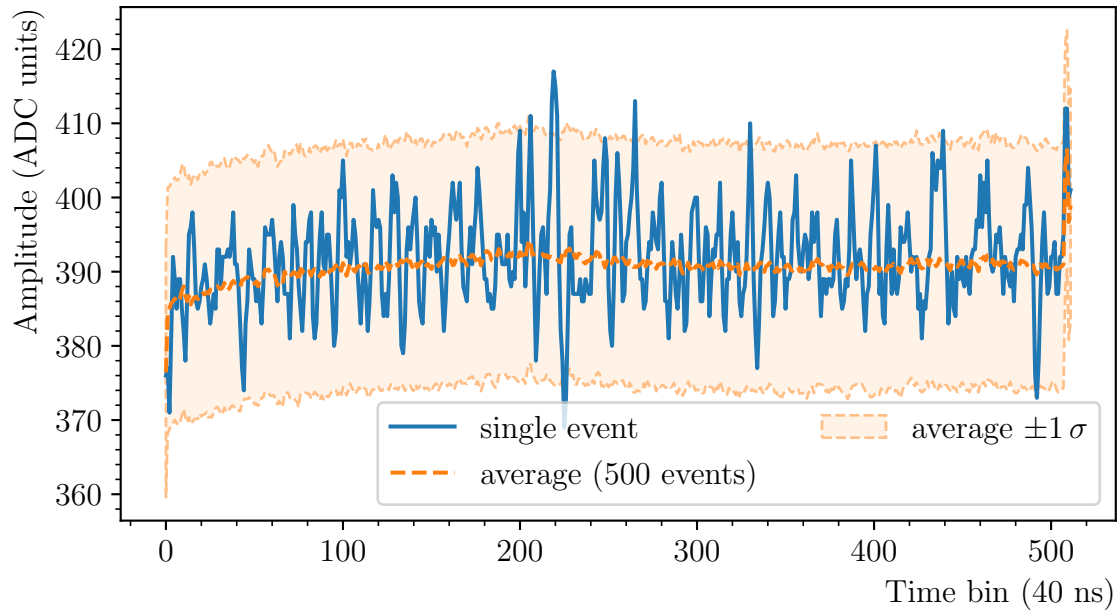


Figure 4.1: Raw electronics waveform. An electronic background with any physical events registered is presented. The waveform is characterized by relatively high noise, and curved baseline and extreme values at the beginning and end of the window.

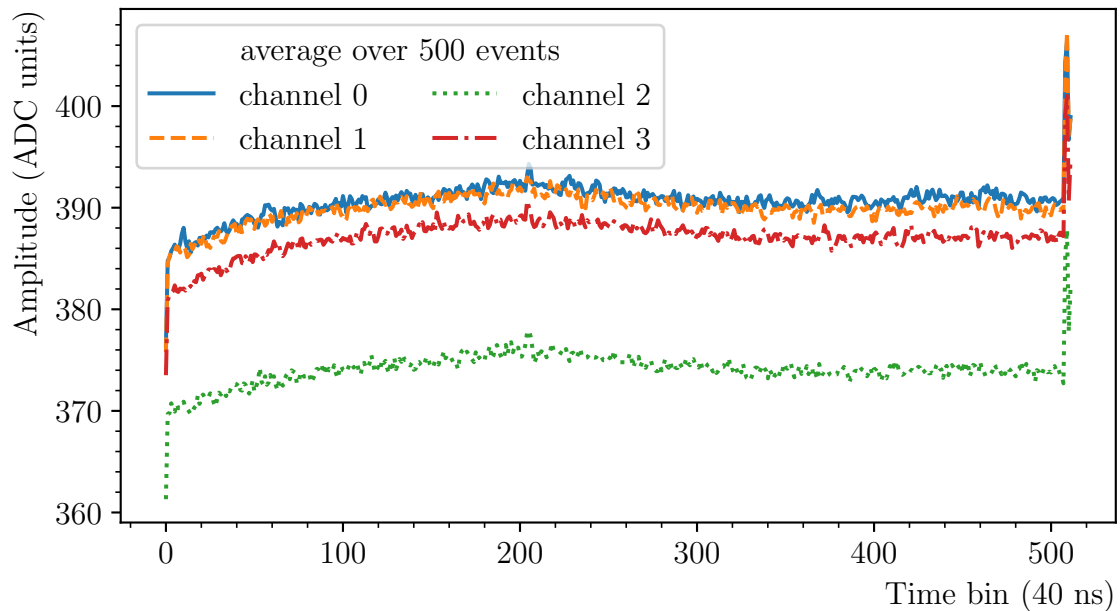


Figure 4.2: Average electronics waveforms for different channels. The baseline level can vary significantly between channels.

### Fixed-pattern noise correction

A Fixed-Patern Noise (FPN) is a pattern of noise specific to the given chip due to manufacturing process. While in principle hard to estimate and correct from channels under load, the GET designer thought ahead of the problem and equipped every 64-channelled AGET with extra 4 FPN-channels not connected to any load with the purpose of measuring the electronic noise. Two forms of the correction has been considered:

1. Subtracting from every channel in a given AGET the average of FPN channels,
2. Subtracting from every channel in a given AGET the value of the closest FPN channel.

For the current analysis the first form of subtracting the average FPN was chosen.

### Baseline correction

For experimental data two forms of the correction has been considered:

1. Internal - the baseline calculated from time cells 5–25 (out of 512 available) called “pedestal region”. The few first time cells are expected to not contain the signal if the event was correctly triggered. Events with signal in the “pedestal region” will result in the overestimation of the baseline but can be removed during the analysis step. The range of time cells included in the “pedestal region” can be adjusted according to the experimental needs.
2. External - a library baselines can be constructed based on the so called “pedestal runs” — runs without physical signal, triggered artificially with constant rate on the electronic background. Collecting such “pedestal runs” before and after a set of physics runs is part of the WARSAW TPC workflow.

The internal baselines were used for the current analysis.

### Circular buffer correction

The circular buffer correction described in [38] as a correction for characteristic signal effect due to switching at the end of the GETs circular buffer memory has not been implemented in the current WARSAW TPC set of corrections.

### Shaping-time deconvolution

Another possible correction is a so-called shaping time deconvolution. The aim of this correction is to recover original shape of a waveform knowing the electronic response. In practice the correction can be realized with numerical deconvolution or statistical unfolding algorithm [39].

The importance of this correction varies greatly depending on the shaping-time constant configured for each channel. The choice of shaping-time is a tradeoff between lowering the electronic noise level due to filtering and signal deformation. Comparison of waveforms collected with different shaping-times is Figure 4.3.

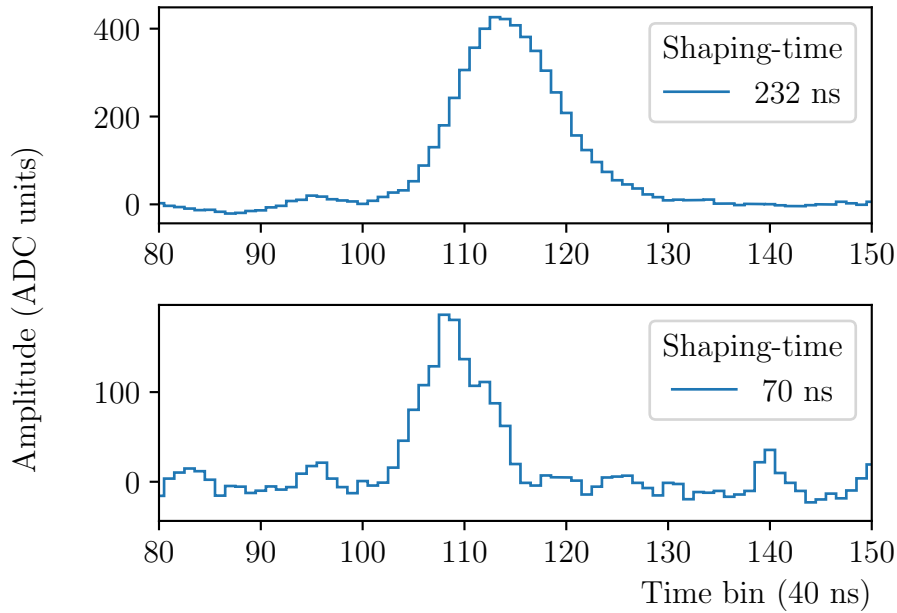


Figure 4.3: Comparison of shaping times. Waveforms from single strips are presented on an example  $\alpha$  particle passing transversal to the strip. The setting differs only by an electronics shaping time. Bigger shaping time filters the noise better but produces non-symmetric signal with long tail. FPN and baseline corrections were applied.

For previous experiments [21] with the WARSAW TPC the shaping-time constant of a low values of 70 ns has been used, resulting in a noisy but minimally deformed data. For that reason the shaping time deconvolution correction has been ruled out as a diminishing return and not implemented. During the experiment at HI $\gamma$ S a shaping-time constant of higher value of 232 ns has been used and a need to apply the deconvolution has been recognized after reconsideration. While a robust algorithm has not been read for the current analysis a proof of concept has been already accomplished [35].

## Corrected data

An electronic waveform after applying the FPN and baseline corrections is presented in the Figure 4.4. The corrections were able to correctly reduce the noise, flatten the baseline and shift it to zero, so that all the channel corrected waveforms are centered around the same value.

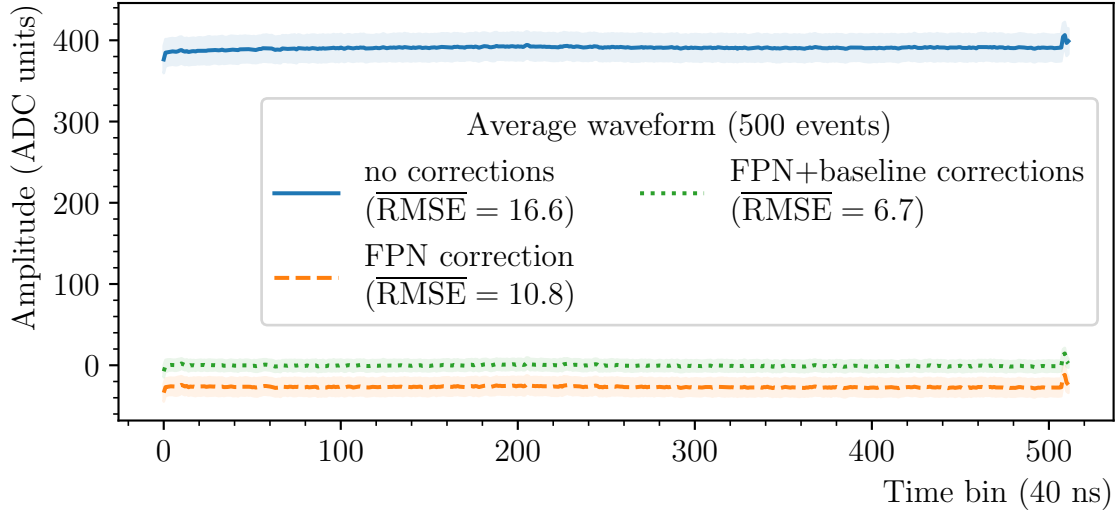


Figure 4.4: Electronic waveform corrections. The same event as in Figure 4.1 is depicted after the FPN and baseline corrections. The corrections result in waveform of lower noise, flat baseline and centered around 0. The extreme values at the beginning and end of the window survived the corrections.

The corrections were unable to correctly remove the abnormal values at the beginning and end of the time window. To mitigate this problem a mask is applied over the time bins that invalidates the time bins in range  $[0, 5]$  and  $(506, 511]$  where the abnormal values occur. The loss of 10 time bins over 512 is not critical, but the fact that the available time window is smaller should be taken into account when optimizing the sampling and experimental length for given desired event vertical length. Note in case of internal baseline correction the additional padding with “pedestal region” is required. The region left after applying all necessary masking is known as “signal region”.

Although the corrections discussed corrections are capable of normalizing the average baseline levels across different boards and chip, the normalization of noise levels may not be possible. The comparison of average noise levels for each AsAd and AGET used with the WARSAW TPC DAQ chain is presented of Figure 4.5.

Even though the unique characteristics of every chip and board acquired due to the manufacturing process has been taken into account with the FPN correction, the boards are part of the experimental setup and are part of the more complex system including connection to the ZAP boards and the readout PCB. For instance the length of the wiring at the PCB as well as the number of the interconnected pads building a readout strip to which a given channel is connected can vary significantly.

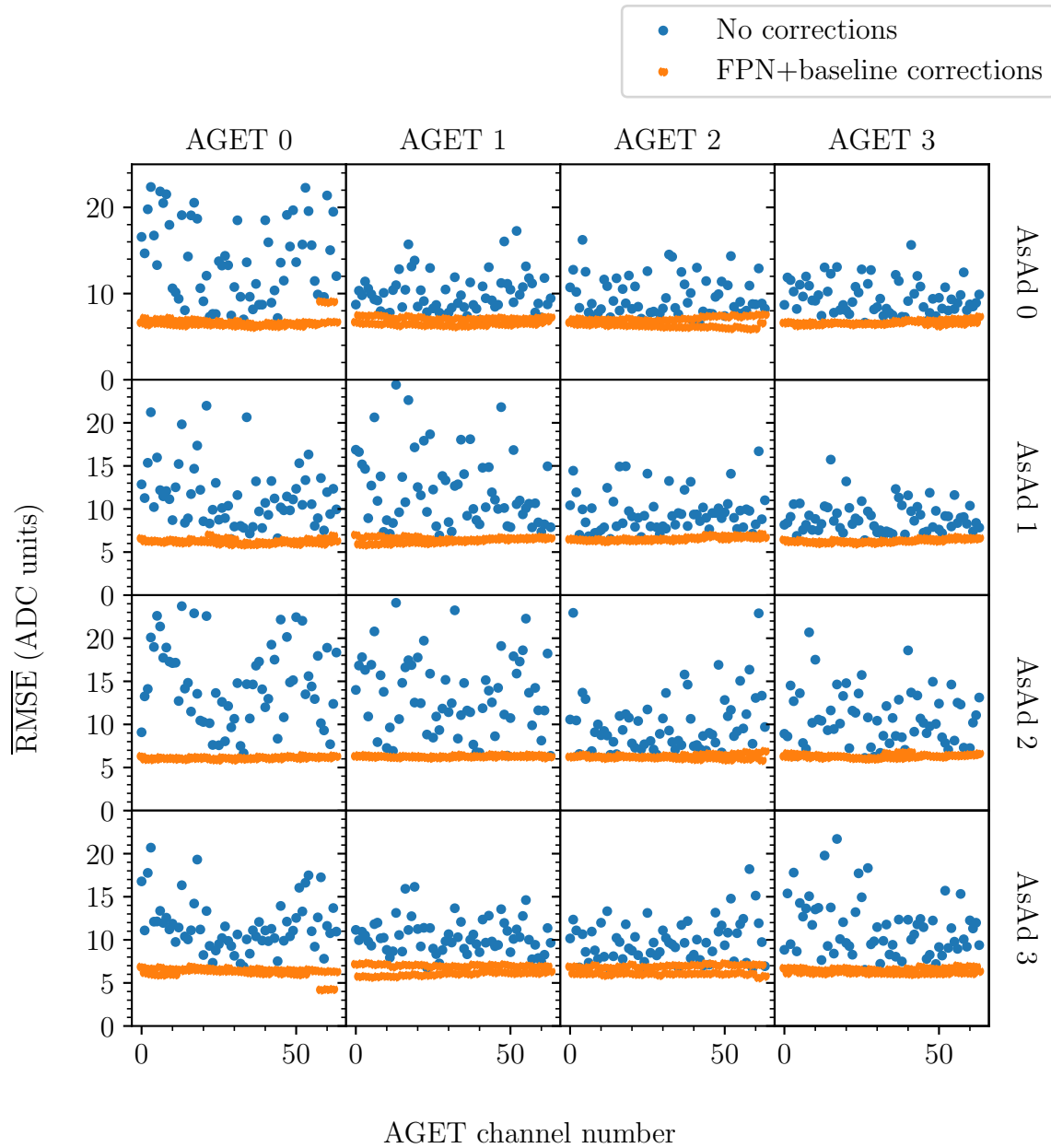


Figure 4.5: Noise reduction with electronics signal corrections. The figure displays the average noise levels for all the electronic channels used during the experiment. The blue series shows the noise levels without any kind of corrections. The orange series shows noise reduced to the level of 6.7(6) ADC units after applying the FPN and baseline corrections. In case of AGET 0 of AsAd 0 and AsAd 3 the three channels (channel numbers 58, 60, 62) can be seen with significantly different noise level. These are auxiliary channels not connected to the readout board and unused during the experiment.

### 4.1.2 Channel mappings

#### Electronic mapping

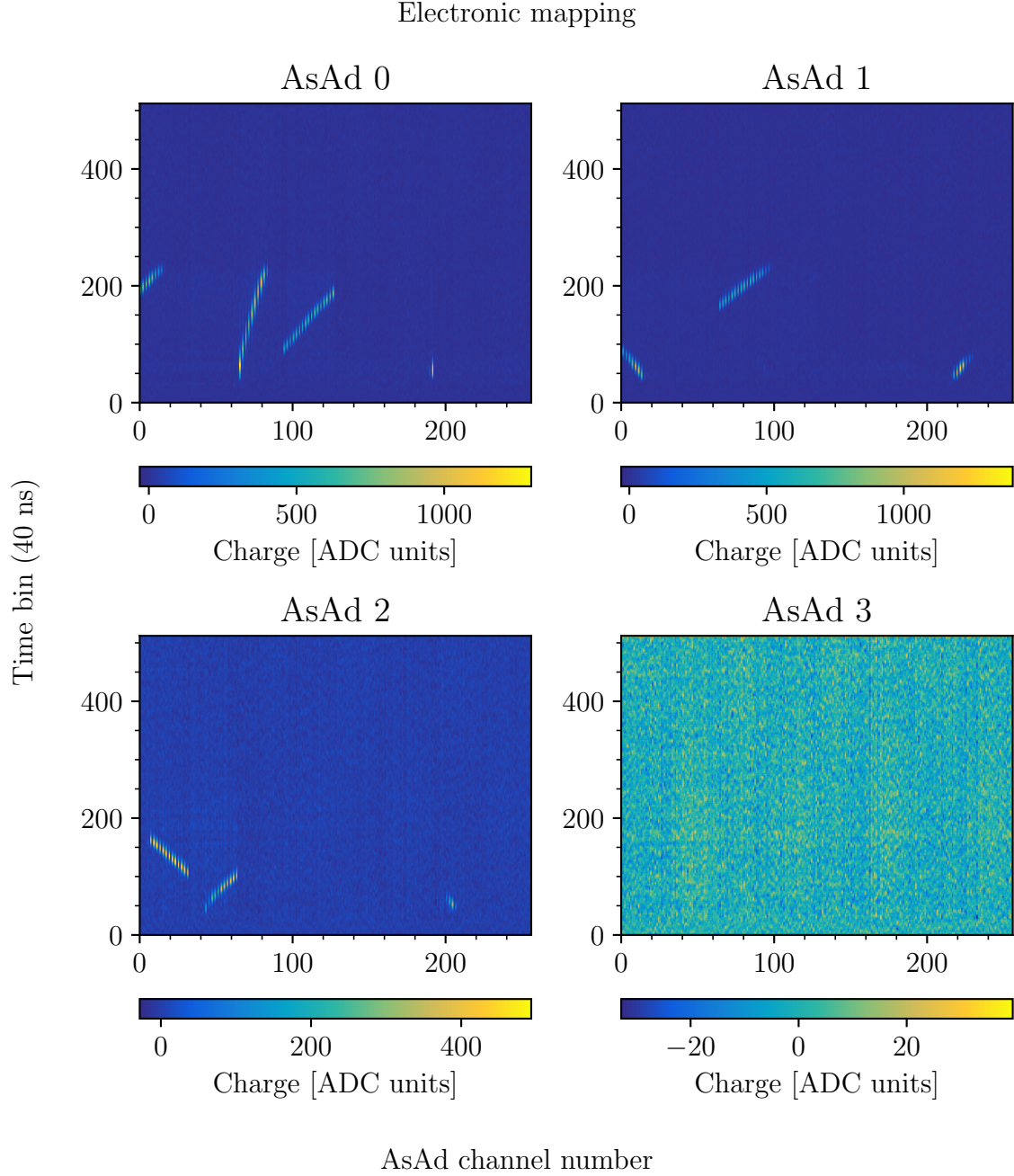


Figure 4.6: Electronic waveform event representation. The data corrected for electronic effects does not reflect the structure of the readout and a mapping from electronic channels to logical channels is needed.

While the initial event reconstruction step of signal processing and correction is done on the lowest level of electronic waveforms, the structure of that data does not reflect the structure of physical problem. As an illustration to this statement, the Figure 4.6 shows a single example event in a electronic channels representation.

The WARSAW TPC data in this representation correspond to a tensor with following indices: [AsAd number][AGET number][Channel number][Time cell].

### Logical mapping

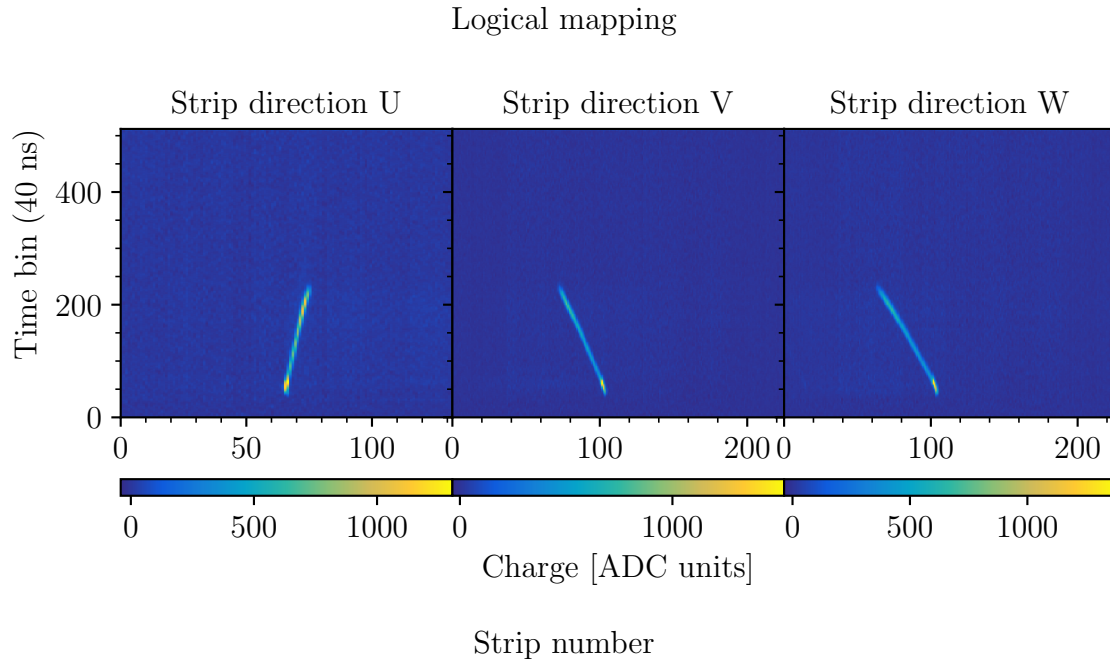


Figure 4.7: Logical channel mapping from electronic channels to readout strips. The same event as in the Figure 4.6 is presented. This representation reflects the structure of readout and first view at the physical event is possible.

To address that problem an electronic to logical channel mapping is used. The mapping is constructed by following the wiring of the electronic channels to the structures characteristic to the readout — in case of WARSAW TPC readout strips. The data after this mapping has a representation as a tensor with indices: [Strip direction][Strip section][Strip number][Time Cell]. To ease a visualization such data is usually plotted after reducing the [Strip section] axis with a sum. Similar procedure of reducing the [Strip section] can be applied during the reconstruction if the strip sections are not used in the algorithm.

The Figure 4.7 shows the logical mapping applied to the event from Figure 4.6. It is worth mentioning that with logical representation all the inherent limitations of the readout becomes apparent. Since the WARSAW TPC employs a strip readout the data in logical representation maps natively to a set of projections of 3D events on the strip directions.

Note that the projections on the strip directions is a lossy representation of a 3D physical space and due to that it is not possible to obtain the complete information about a 3D charge cloud left by the particles in the detector active volume (as opposed to similar readouts built that employ as a readout readout structure pixels instead of strips. In such readout the sampling of readout will result in voxels. The precision of representing a 3D charge cloud in that case is limited only by the voxels granularity).



## Physical mapping

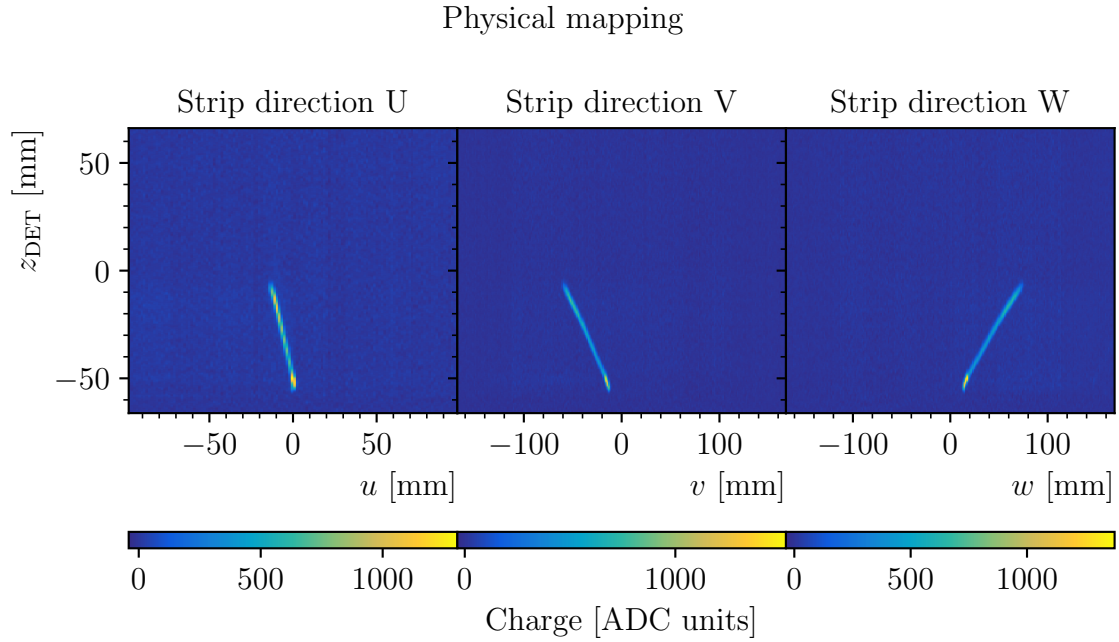


Figure 4.8: Physical channel mapping from logical channels to physical coordinates. Note the change from logical units such as strip number to physical units (mm) with respect to the same event depicted in the Figure 4.7

Finally, readout structures can be expressed in terms of coordinates in physical space in order to obtain so called physical representation. In case of the WARSAW TPC the strip identifiers can be replaced with their position on the readout plane.

Since the strip readout is a lossy representation of a 3D space the data can't be expressed immediately in the 3D cartesian coordinate system, instead the UVW coordinate system is used (Appendix B). With the use of the UVW coordinate system the physical mapping becomes just the replacement of a strip number with a UVW coordinate expressed in the mm.

Note that during the design of the detector the strips identifiers were ordered according to their position so that the strips with next strip identifier are also the next strips in the physical space, the physical mapping is reduced to just changing the ticks on the axes (with a possibility of reflection). The Figure 4.8 presents the physical mapping applied to the same event as in the Figures 4.6 and 4.7.

## 4.2 Event classification

After applying the necessary channel mappings it is possible to establish a connection between a type of physical reaction and its representation as the TPC data.

A natural way to divide the types of observed event is by their topology understood as the number of tracks:

- 0-prong events - events with point-like charge deposits or noise. A typical noise event is depicted in the Figure 4.9,
- 1-prong events - events with visible one track or dot-like. The background  $\alpha$ -particle events depicted in the Figure 4.11 as well as dot-like  $(\gamma, n)$  recoil events depicted in the Figure 4.10 belong to this class. In addition, although producing two charged particles with visible tracks, the  $^{16}\text{O}(\gamma, p)^{15}\text{N}$  events depicted in the Figure 4.13 are also classified as 1-prongs, since their  $^{15}\text{N}$ -tracks are represented as a point like deposit rather than a full prong,
- 2-prong events - events with visible two tracks. The  $^{16}\text{O}(\gamma, \alpha)^{12}\text{C}$  reactions as well as reactions on other isotopes  $^{17,18}\text{O}(\gamma, \alpha)^{13,14}\text{C}$  belong to this class of events. A typical  $\text{O}(\gamma, \alpha)\text{C}$  is depicted in the Figure 4.12,
- 3-prong events - events with visible three tracks. A  $^{12}\text{C}(\gamma, 3\alpha)$  reaction depicted in the Figure 4.14 belong to this class,
- “exotic” events - events with multiple tracks or multiple connected vertices.

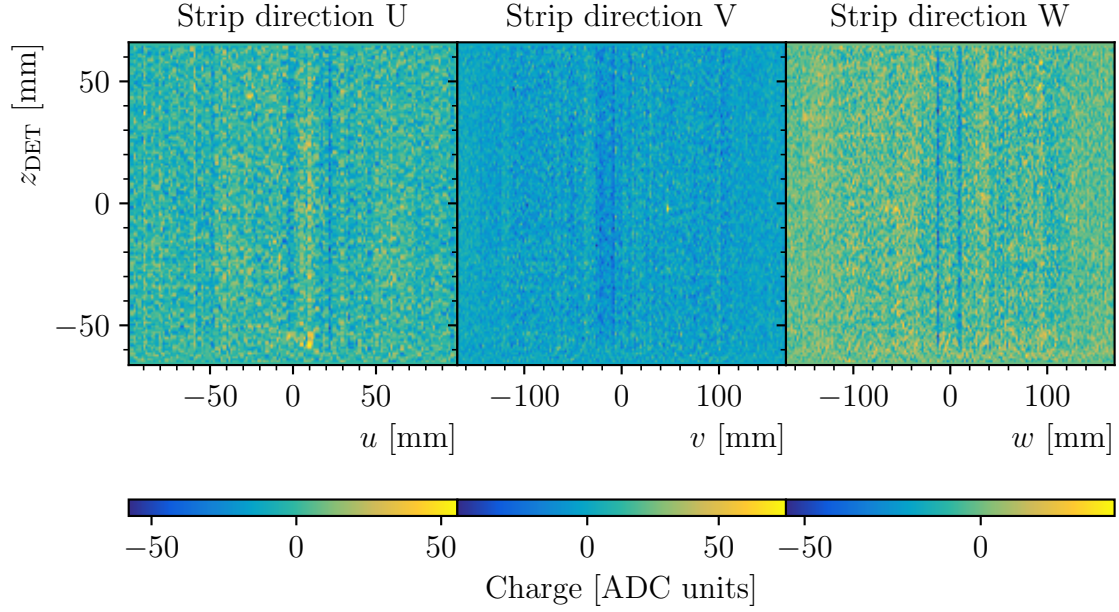


Figure 4.9: Typical noise event. The DAQ triggered either on a high fluctuation of electronic noise indicating that the online filter threshold could be higher or on very faint scattering on the edge of detection. The event depicts a typical 0-prong topology.

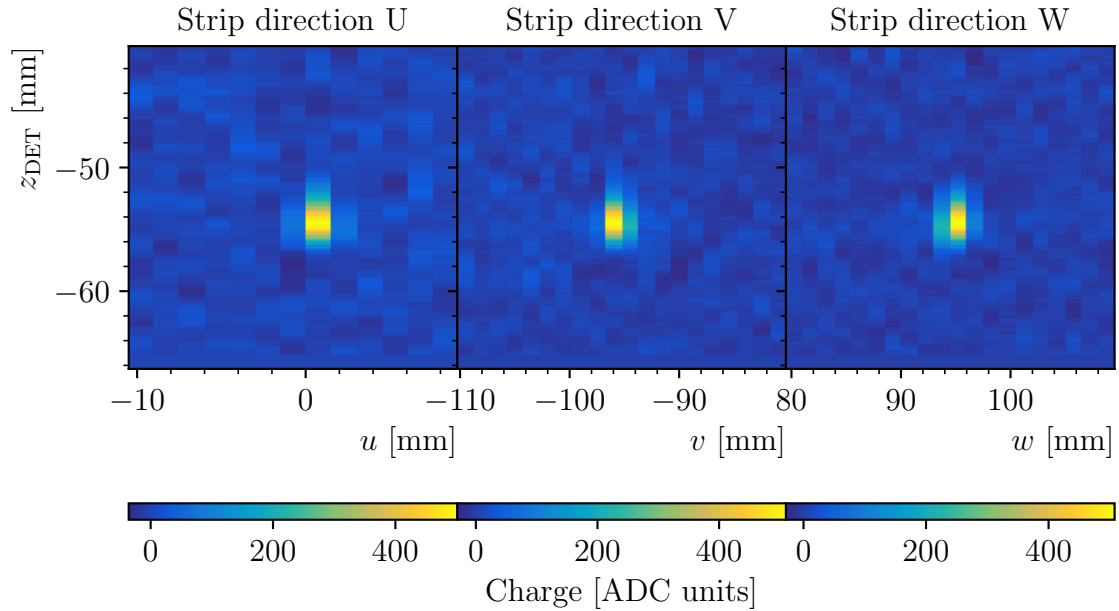


Figure 4.10: Typical dot-like event produced as by a recoil of  $(\gamma, n)$  reactions. The event is characterized by a dot-like or an elongated dot. The position of event in space can be determined, but marking the vertex or an endpoint is impossible. For technical reasons such event is recognized as a 1-prong topology.

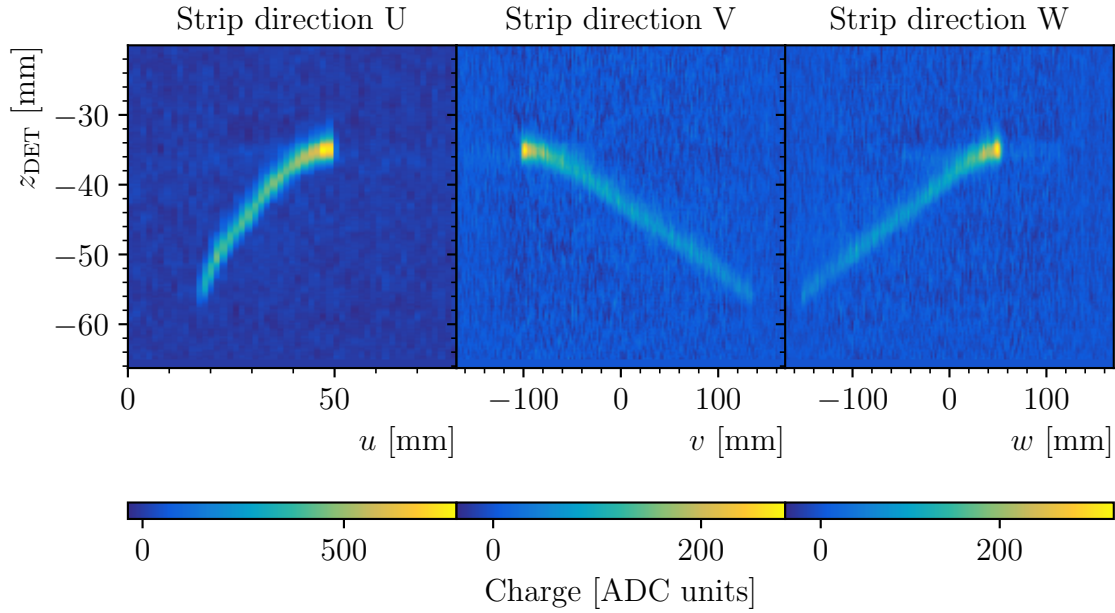


Figure 4.11: Typical 1-prong  $\alpha$  event. The  $\alpha$  particle originates from the decay at the chamber's vacuum vessel. The event is characterized by a single relatively long track ending with a high-deposit due to a Bragg peak. The event is expected to be not related with the beam position in space.

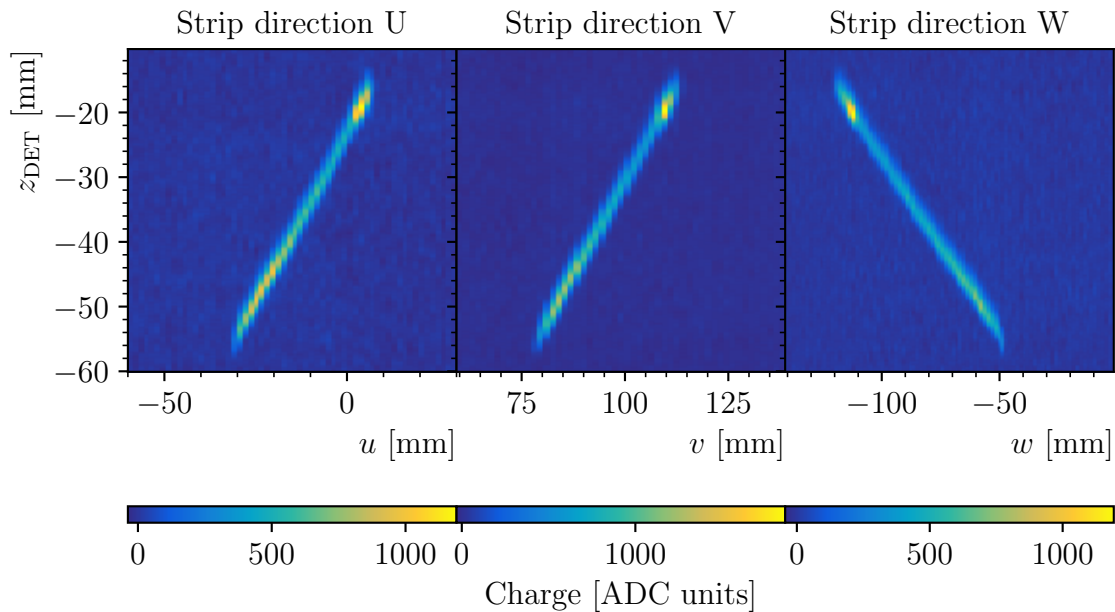


Figure 4.12: Typical  $O(\gamma, \alpha)C$  event. The event is characterized by a long, well-defined  $\alpha$ -particle track, and a short but very intense  $C$  track. This event represents a typical 2-prong topology. Note that all the reactions with isotopes  $^{16,17,18}\text{O}(\gamma, \alpha)^{12,13,14}\text{C}$  will produce similar geometries of tracks with differing lengths.

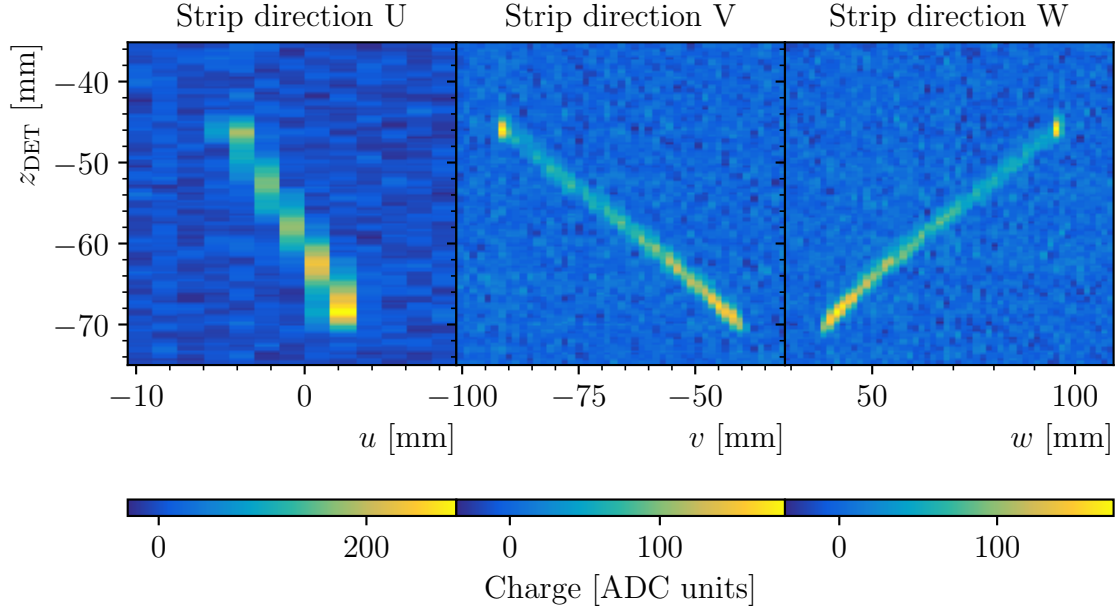


Figure 4.13: Typical  $^{16}\text{O}(\gamma, p)^{15}\text{N}$  event. Such events are characterized by a long but faint  $p$  track and a point-like  $^{15}\text{N}$  track. Due to that characteristic those event stand apart from the  $\text{O}(\gamma, \alpha)\text{C}$  events from Figure 4.12. Due to a point-like  $^{15}\text{N}$  track the event is classified as a 1-prong, to avoid the large error of reconstructing the  $^{15}\text{N}$  track.

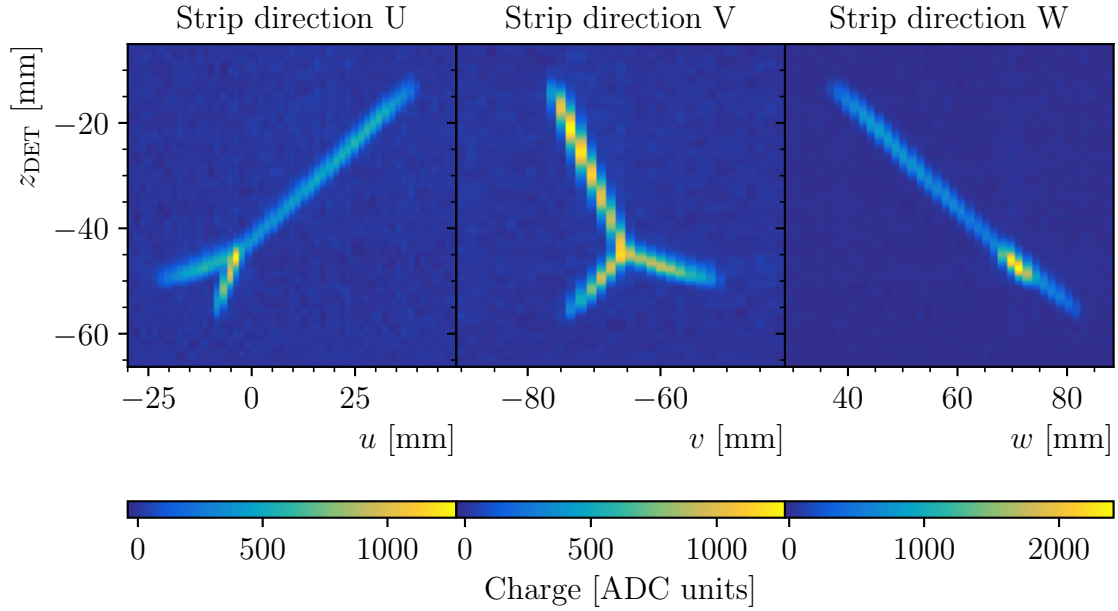


Figure 4.14: Typical  $^{12}\text{C}(\gamma, 3\alpha)$  event. Three tracks coming out from a common vertex is the 3-prong topology case. At the W-strip projection two of the three tracks are overlaid, but thanks to the strip redundancy a reconstruction is possible with the remaining U and W-strip projections.

## Pile-up

As any other trigger-based detector there is a certain probability that two random events will arrive during the same time window resulting in one recorded event including two or more physical events. In some cases the separation of the physical events is trivial due to different spatial positions, in other cases the events are overlaid and the separation may pose significant problem.

A pile-up event of two 2-prongs with good separation is given in the Figure 4.15. For high rate reactions the pile-up event may constitute a significant fraction of data and depending on the capabilities of the event reconstruction be a significant problem.

For the current reconstruction the pile-up rates were estimated to be below 3‰ for any  $\gamma$ -beam energy (without differentiating between pile-up constituents such as 2-prong-2-prong or 2-prong-3-prong pile-ups). Such low rates do not pose a problem for the experiment but become a nuisance and correction is required when calculating the reaction absolute cross-sections.

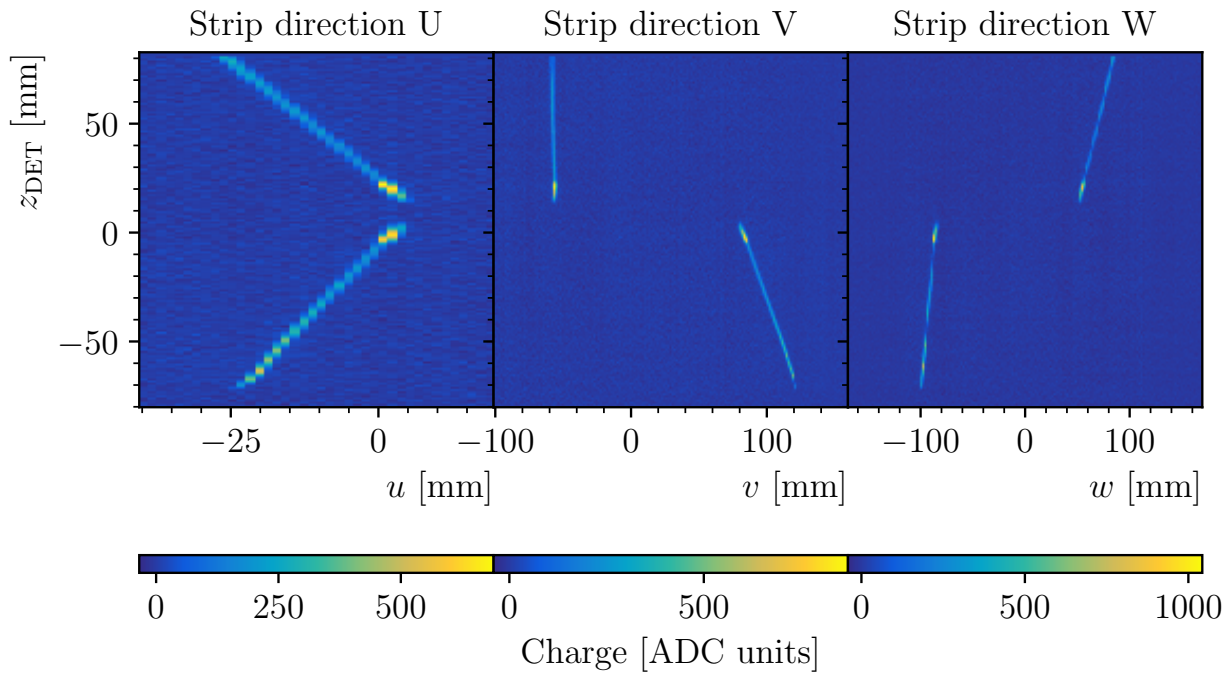


Figure 4.15: Two 2-prong event pile-up example. The detector was triggered by the track originating around  $z_{\text{DET}} = -70$  mm. The two 2-prong are completely separated, but another case with partial overlay of some tracks and mimicking a 4-prong event is also possible.

## 4.3 Manual reconstruction

At the time of conducting the study a machine reconstruction algorithm for the WARSAW TPC was not ready. In order to reconstruct a data a human based so called manual reconstruction procedure was used. The manual reconstruction or scanning was a typical method of reconstruction in the past with a tradition ranging to the scanning the photographs of the bubble chambers. The method was later augmented with mechanical equipment [40, 41] and finally replaced with the software algorithms such as Hough transform [42].

In order to proceed with the study the WARSAW TPC collaboration decided to fallback to this method. Contrary to the information stated in [22] the WARSAW TPC automatic reconstruction is still under development and hadn't been studied to the point. The possible machine reconstruction algorithms and started work is discussed in Chapter 7. The manually reconstructed material beside being used for analysis can be used to some degree as a replacement for realistic simulations till until such framework is available.

### 4.3.1 Experts & datasets

The manual reconstruction was conducted by a group of 7 human experts. Each expert was an active member of the WARSAW TPC collaboration with a technical insight into the workings of the detector and the physical aspects of the measurement. Not every expert participated in reconstruction of every run.

In order to monitor the quality of the manual reconstructions experts were working on two datasets:

- Paired dataset — the same events reconstructed by multiple experts. The existence of this dataset allows to monitor the discrepancies introduced by the human factor on event by event basis.
- Unpaired dataset — events reconstructed by only one experts. Any discrepancies introduced by the human factor can be studied only on whole sample level, eg. comparing the shape of distributions.

The proportion of the paired and unpaired datasets reflects a compromise between monitoring the quality of reconstruction (paired dataset) and the need to process high amounts data (unpaired dataset).

Given the limitations of the human recognition the main aim of the manual reconstructions was identifying the number of tracks in the event as well as providing the position of event vertex and endpoint. In addition the experts made annotation about any exotic events or pileups. The information provided by the experts can be seen in two ways:

1. Classification using only the number of tracks. The events were labeled as belonging to the 0-prong, 1-prong, 2-prong, 3-prong classes.
2. Regression. After selecting a given class the distribution of that class characteristics can be given, such as position of vertex or length of the shortest track.

### 4.3.2 Procedure

The events for reconstruction were presented to the expert in a form of three images each one depicting the projection of an event on different strip UVW strip direction (the physical mapping described in the previous sections, such as Figures). The experts were tasked to mark the positions of vertex and all the track endpoints. A specific graphical application (discussed in Appendix D) was written to augment the process.

The reconstruction as a whole was coordinated in the following fashion:

1. For every run all participating experts were tasked with reconstruction exactly the same 500 events. Events reconstructed this way created paired datasets.
2. The paired dataset classification was investigated and any differences in event classification were discussed with the experts.
3. One expert reconstructed additional 500 events. Both these events and the 500 events from the first point were used to establish the offline trigger used for the current run (offline trigger discussed later in Section 4.5).
4. Every expert has been assigned independent portion of events from that run. The events were first processed by the offline trigger and only events passing the offline trigger were subjects of reconstruction. Events reconstructed this way created un-paired datasets.

As the paired dataset contains duplicated events, the final dataset used for data analysis was constructed by merging for event reconstructed run:

- the 1000 events used for establishing the offline trigger,
- all the unpaired dataset reconstructed for that run.

## 4.4 Reconstruction quality

The manually reconstruction quality was assessed in a multiple ways. Given the different characteristic of the paired and unpaired datasets the appropriate statistical analysis methods were used. Note, a physical analysis of the reconstructed is presented in Chapter 5.

Due to the unavailability of a WARSAW TPC simulation framework at the time of the study it was not possible to investigate the manual reconstruction quality on a simulation dataset with known classes of events and positions of endpoints, instead only a statistical analysis of consistency of the obtained distributions on the unpaired dataset, or a cross-check between multiple experts with the paired dataset was possible.

The presented partial results were subjects of the pseudonymization to protect the experts' identity.



#### 4.4.1 Misidentification

The misidentification rates were estimated from the paired data. The maximal misidentification probability taken over the experts, runs is estimated to be 3%. Beside the numerical estimation each case of identification was studied in order to establish the correct classification of the event (by a democratic voting by at group of at least two experts) and improve further studies.

An observation has been made that the misidentification rate between two classes is not symmetric, usually the classes with higher number of tracks are mispredicted to contain lower number of tracks, than the opposite. The particular case of such phenomenon is mislabeling a 3-prong  $^{12}\text{C}(\gamma, 3\alpha)$  to be a 2-prong when the opening angle between two of the produced  $\alpha$  particles is small. An example 3-prong to 2-prong misidentification is depicted in the Figure 4.16. This particular misidentification is not an inherent problem of the manual reconstruction as similar problems has been observed by other groups employing machine reconstruction [34].

The misidentification at this step should be possible to detect and correct later during physical analysis step step when studying the event characteristic such as energy and momentum distributions.

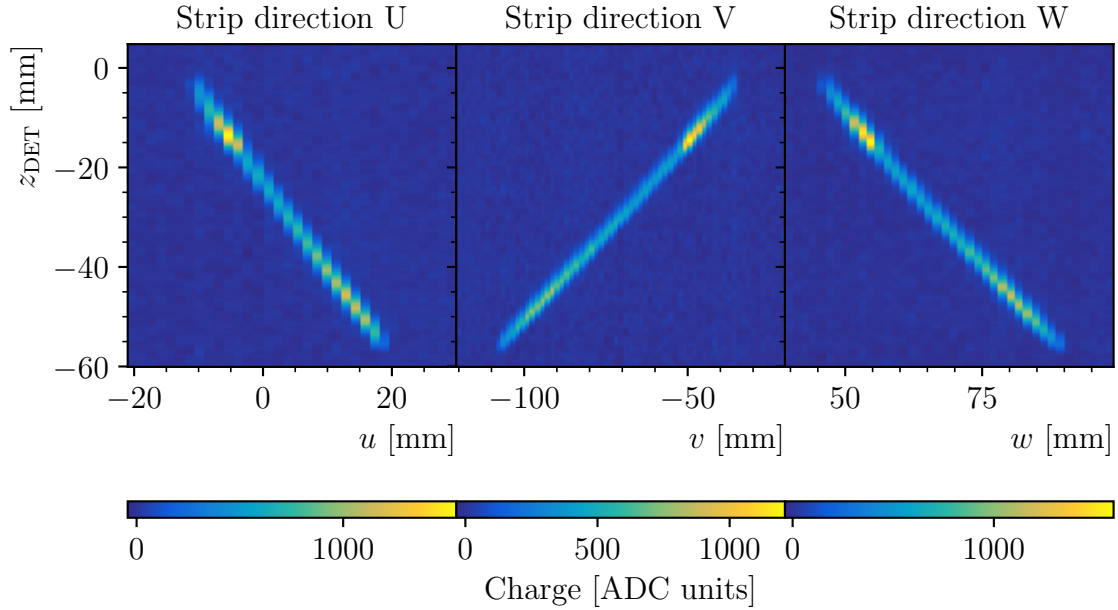


Figure 4.16: Example 3-prong event misidentified as a 2-prong. Two  $\alpha$  particles of a  $^{12}\text{C}(\gamma, 3\alpha)$  event due to a small opening angle between them were mistaken for an C from O  $(\gamma, \alpha)$  C event. Note the subtle difference by comparing with typical O  $(\gamma, \alpha)$  C from Figure 4.12 and  $^{12}\text{C}(\gamma, \alpha)$  from Figure 4.14. The misidentification can be visible during the analysis as the event characteristics will be different, for instance the track length will be different than expected.

### 4.4.2 Reconstruction resolution

With the absence of simulations the reconstruction resolution was estimated as a variance between the same events reconstructed by different experts. While this method reflects the differences between different experts, the merged dataset used for physical analysis may constitute of non-equal contributions of events reconstructed by multiple experts and therefore the resolution calculated on the paired dataset may not reflect directly the resolution on that merged dataset.

The estimated resolutions for the length and angle  $\theta_{\text{BEAM}}$  (polar angle in BEAM coordinate system discussed in the Appendix B) for the longest track for the 2-prong event class is 1.3(4) mm and 1.0(3) $^\circ$  respectively.

Due to the limited size in the available samples the presented values were estimated over the whole samples and don't reflect the possible resolution dependence on particle energy and orientation in space due to different granularity of segmentation in readout plane (fixed readout-pad size) and along the drift direction (flexible with drift velocity and electronics sampling frequency).

### 4.4.3 Unpaired dataset

The unpaired datasets were analyzed two-fold: for the classification of events and for regression of events characteristics. The numbers of events of given classes present in a fixed-size sample reconstructed by a single expert should follow a binomial distribution. Assuming the stability of a beam, the samples presented to all the expert should be drawn from the same multinomial distribution.

Therefore the consistency of event classification was investigated using a Pearson's- $\chi^2$  test for the multinomial distribution. The results of a test for an example run are presented in Table 4.1. The portions on data with high discrepancies (a portion of the data scoring below the test size of  $\alpha = 5\%$ .) were removed from further studies and not merged to the final dataset for the physical analysis.

Table 4.1: Event classification consistency for a run with nominal  $\gamma$ -beam energy  $E_\gamma = 13.1$  MeV. The occurrences of event classes were calculated for each data-shard ( $k_i$  for  $i$ -prong class). The parameters of the multinomial distributions were estimated using all the data-shards with the result  $p_2 = 0.212$ ,  $p_3 = 0.002$  ( $p_i$  as a probability of  $i$ -prong class). The results of Pearson's- $\chi^2$  test to the distribution  $\mathcal{M}(k_2, k_3, n - k_2 - k_3 | n, p_2, p_3, 1 - p_2 - p_3)$  are presented. The p-value for the run shard 2 is very small, therefore the run was removed further processing.

run shard	expert id	$n$	$k_2$	$k_3$	p-value
0	A	1000	240	2	1.1e-01
1	A	3852	852	5	3.2e-01
2	B	3852	619	8	3.3e-14
3	C	3852	859	7	2.8e-01
4	C	3852	864	5	1.6e-01
5	A	3852	876	8	7.3e-02

In case of examining the distributions of event characteristics such as track lengths or angles a nonparametric treatment is preferable, because the shapes of the distribution are not obvious. For comparing multiple number samples (run-shards) a k-sample Anderson-Darling<sup>1</sup> test [43] was chosen with the null hypothesis  $H_0$  stating that all the samples were drawn from the same distribution.

The track length and angle  $\theta_{\text{BEAM}}$  for each run were analyzed with the test. In every run the test results in the rejection of the null hypothesis  $H_0$  for the track length distribution and non-rejection in case of  $\theta_{\text{BEAM}}$ . An example track length distributions analyzed with the test are presented in the Figure 4.17.

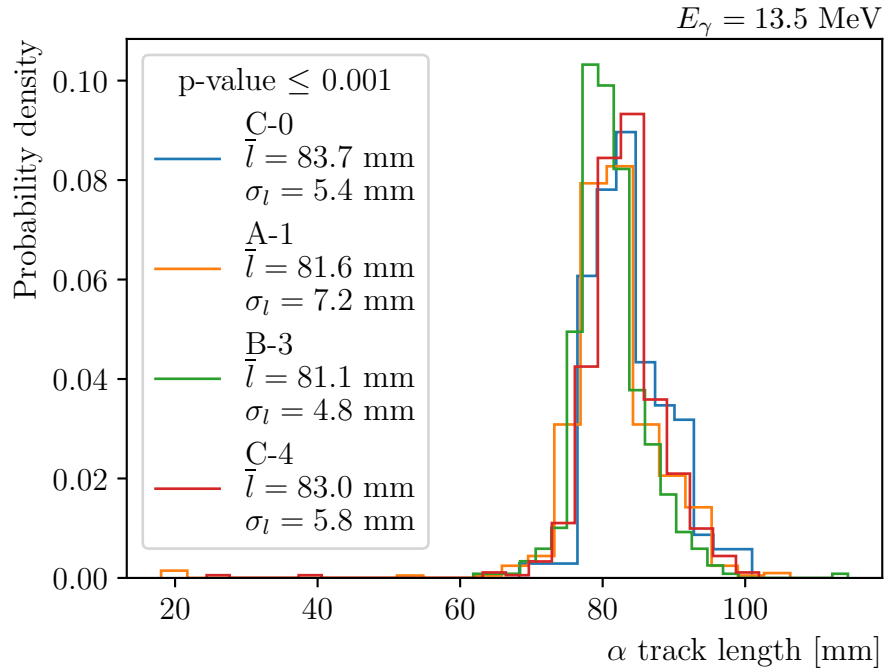


Figure 4.17: Reconstructed track length consistency on example unpaired dataset for nominal  $\gamma$ -beam energy  $E_\gamma = 13.5$  MeV. For visualization the distributions for all the samples are plotted. The experts are encoded with letter, the run-shard is encoded by number, for instance C-0 reads as shard 0 of the current run that was reconstructed by experts C. A k-sample Anderson-Darling test is done with a null hypothesis that all the samples come from the same distribution. The obtained p-value is smaller than 0.1% the assumed significance level  $\alpha = 5\%$  and the null hypothesis is rejected.

<sup>1</sup>The Anderson-Darling test is a nonparametric test from the family of Kolmogorov-Smirnov (K-S) tests [43].

To find the potentially offending samples a post hoc analysis with a pairwise Anderson-Darling test was done. The typical results of the post hoc analysis are presented in the Figure 4.18. A common trend for all the runs was observed a sample reconstructed by a given expert is consistent with other samples reconstructed by the same expert, while the consistency with other experts seem to be random across different experts, samples and runs.

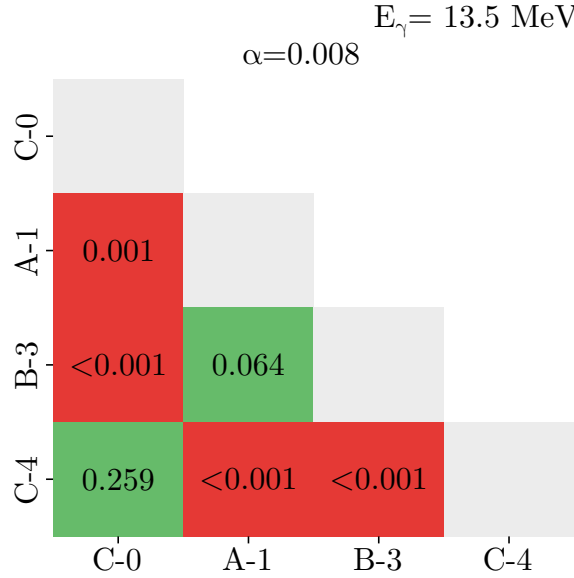


Figure 4.18: Post hoc analysis of  $\alpha$  track length on example unpaired dataset for nominal  $\gamma$ -beam energy  $E_\gamma = 13.5 \text{ MeV}$  (same as distributions depicted in Figure 4.17). A pairwise Anderson-Darling test is done in order to find which samples are not compatible. A p-value is listed for each pair. The experts are encoded with letter, the run-shard is encoded by number. Different shards reconstructed by the same expert are consistent, while the consistency between experts seems to be random. Note a Bonferroni method is used to adjust the significance level for multiple comparisons.

This result indicates that an expert keeps the same quality over time and gives a prospect that even though the results obtained by the different experts differ a systematic “expert correction” may be possible. The length distributions obtained by merging data reconstructed by multiple experts without any correction will result in broader distributions than if only one expert was reconstructing. The practicality of creating “expert correction” an expert correction at this time is limited as only limited number of samples are available for each expert. An alternative approach would be calculating the “expert correction” from a simulation data.

For the current work the decision has been made to proceed without the “expert correction” and include all the samples not rejected by other tests in the analysis.

As a clarification a similar compatibility study could be accomplished on a paired dataset with statical tests appropriate for repeated measurements (such as utilizing the Friedman test with a Nemenyi test post hoc in place of Anderson-Darling tests as with unpaired data). In the current study the size of the paired dataset was small and studying the much bigger unpaired dataset was prioritized.

## 4.5 Offline trigger

Offline trigger is a process of event selection in order to lessen the size of data to be processed similarly to the online trigger (Section 2.5). While the online trigger is used during the data taking and usually implemented in hardware due to the fast processing requirement, the offline trigger is applied to the data that is already stored and is usually implemented in software since the more complex criteria are easier to implement and slower processing times are allowed without negative impact on the system.

The need for applying an offline trigger in the current reconstruction has been identified due to a large single event processing times achieved by human experts (ranging from single seconds to minutes in complex cases).

### 4.5.1 Implementation

An offline trigger discriminating the general event topology (number of tracks in the events) has been proposed in order to remove the 0- and 1-prong background from the data reconstructed by the experts.

Since proper track detection is relatively time consuming task and a robust algorithm for the WARSAW TPC has not been available at the time it was not possible to construct criteria operating on the detected number of tracks directly.

Instead, given that at this step only an information about the number of tracks and not necessary their locations were needed a criterion based on a features highly correlated to the desired number of tracks could be used. An offline trigger operating on two features was proposed:

1. Total (or integrated) charge deposited in the event.
2. Maximal charge deposited in the event in a single time cell.

The Figure 4.19 depicts a construction of offline trigger operating on total and maximal charge in event. Both the signal and background classes are separating to different clusters with little overlay between the clusters. Note the prong label used to construct the trigger came from the manual reconstruction meaning they were assigned by a human expert.

Other offline triggers based on different features such as event multiplicity (defined as number of channels above some threshold or other) or spatial size of event (estimated as the diagonal of the area of interest after applying a clustering algorithm) were considered. The maximal-total charge trigger was used due to its simplicity and sufficient separation of 1- and 2-prong events.

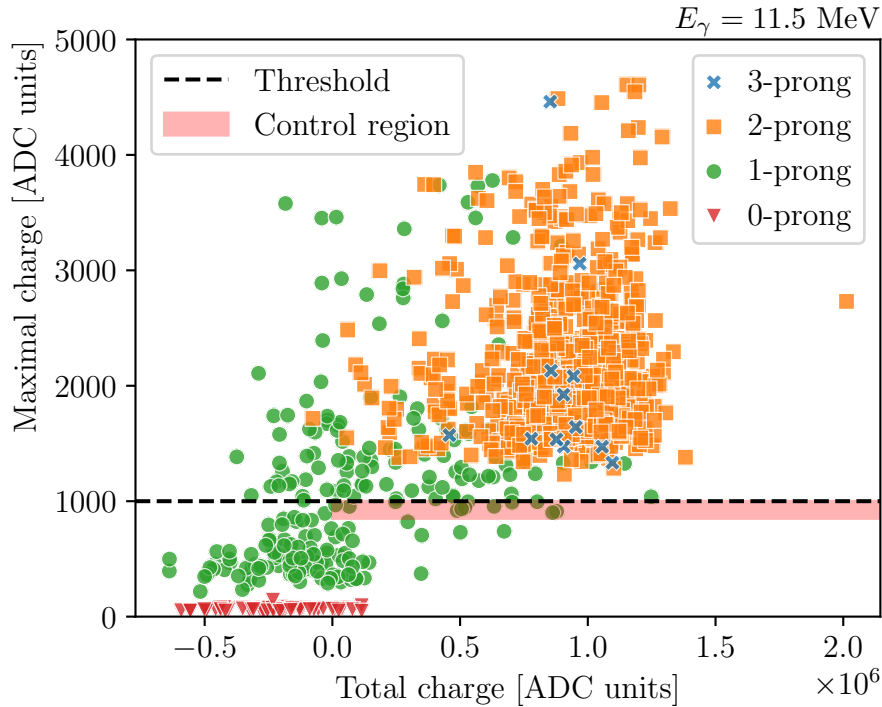


Figure 4.19: Level-2 offline trigger operating on maximal charge deposit and total charge deposit in an event. The dashed line depicts the threshold, events below the threshold are considered background and rejected from further reconstruction. The data point depicts the values of variables used by the threshold for events classified by experts. The aim of the trigger was to reduce the number of 0- and 1-prongs in the samples.

### 4.5.2 Trigger Tuning

Since the deposit of charge is closely related to the energy of the detected particles and working point of the detector (medium density, electronic sampling rate, etc.) that can vary on run basis, the trigger had to be tuned for each operational point used.

In order to tune a offline trigger parameters an expert had to manually label a given number of events (1000 in the current study), then a map of event features including the labeling was constructed. The trigger threshold were chosen basing on that map (example map presented in the Figure 4.19).

The requirement put on the trigger was to achieve maximum sensitivity<sup>2</sup>, that is to all events identified as a signal were passing the signal.

In order to achieve the maximum sensitivity while allowing possibly small number of background events passing two triggers were prepared accepting events in two different region in the feature space:

1. Above given threshold - to be used during ordinary reconstruction,

<sup>2</sup>The use of sensitivity name stems from the statistical classification [44] where the sensitivity is defined as the fraction of the signal entries that were predicted by a classifier to be signal to the total number of signal entries.

2. Narrow area below the threshold, so called “control region” - to be used for cross-check.

In order to verify the sensitivity of the trigger, one of the experts was tasked in evaluating the possibility of occurrence of any 2- or 3-prong events in the “control region” in a sample of 3852 events (size used for convenience as it corresponds to 1 shard of a run stored on a disk). In case of occurrence of any 2- or 3-prong events in the “control region” the trigger threshold would be lowered and the procedure repeated. Once the sensitivity of the trigger was established the first trigger parameters were delivered to the experts to be used during the reconstruction of runs from the given  $\gamma$ -beam energy. The compositions of samples before and after the trigger are depicted in the Figure 4.20.

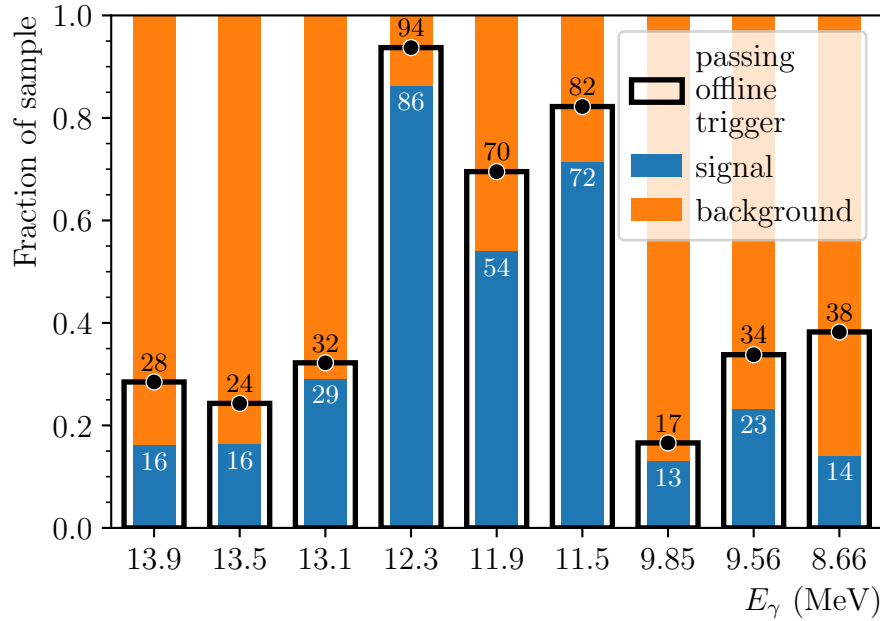


Figure 4.20: Sensitivity of offline trigger. For every reconstructed run an estimated fractions of signal (2- and 3-prong) events is listed (white text) as well as estimated composition and percent of events passing the offline trigger (black text). Note that in all cases the trigger accepts all the signal achieving maximal sensitivity.

### 4.5.3 Trigger efficiency

The trigger efficiency understood as the fraction of events rejected by the trigger to total number of events in a sample, varies with the energy as the fractions of classes of events change with the  $\gamma$ -beam energy. While from the construction the sensitivity of the trigger is assumed to be maximal, the poorer efficiency does not indicate a problem with a trigger, just that the decrease of load is not substantial.

The estimated composition of samples by number of prongs as well as the trigger efficiency for each  $\gamma$ -beam nominal energy is given in Table 4.2.

Table 4.2: Offline trigger efficiency and event class distribution. The fractions of events of a given class were estimation on a sample of a 1000 events classified by a single expert.

$E_\gamma$ (MeV)	Fraction of event class in %				Efficiency %
	0-prong	1-prong	2-prong	3-prong	
13.9	0.10	83.80	12.40	3.70	71.52
13.5	0.40	83.30	15.80	0.50	75.70
13.1	0.20	70.70	28.80	0.30	67.78
12.3	1.10	12.60	85.50	0.80	6.28
11.9	13.30	32.70	52.80	1.20	30.48
11.5	4.90	23.60	70.30	1.20	17.78
9.85	47.05	24.79	15.03	13.13	83.41
9.56	53.37	23.37	15.84	7.43	66.20
8.66	13.40	72.50	11.80	2.30	61.76



# Chapter 5

## Analysis

The following analysis was done using Scientific Python ecosystem (SciPy [45], NumPy [46], Matplotlib [47], pandas [48], SymPy [49], scikit-learn [50]) Scikit-HEP ecosystem (Python packages for HEP [51]: uproot [52], iminuit [53], hist [54]) supported with the TPCReco package (Appendix D). This choice is justified by the relatively small by today's standards size of dataset used in the study (total of size of experimental data from the main detector of approximately 4 TB), and low computational intensity of the problems.

### 5.1 Beam monitoring

The beam monitoring plays an important role during the experiments as it both allow for energy calibration of the data and is essential for intensity and rate studies required to provide absolute cross-sections of measured reactions.

While a number of specialized equipment for monitoring the has been used during the experiment some of the beam characteristics can be extracted or calculated with the TPC data.

#### 5.1.1 Intensity

While the beam intensity has been monitored during the experiment and recorded for offline analysis, analyzing in order to study and calculate the absolute cross-sections of the reactions is outside of scope of this work. In present analysis the beam intensity time series data has been treated only as a reference for beam stability, as a sudden change of the beam intensity could signalize a change of other beam characteristics that might be difficult to notice with other sensors that presents their measurements integrated over time.

For the beam stability in time estimation the beam intensity measured with the MPAD and collected with the TUKAN scaler has been studied. An example beam intensity time series is depicted on 5.1.

After inspection no unusually behaviors — such as intensity spikes or drops — has been observed in the reconstruct events' time-window for any of the analyzed runs with a notable exception that for  $E_\gamma = 9.85$  and  $E_\gamma = 12.3$  the beam intensity was increased shortly after the beam started.

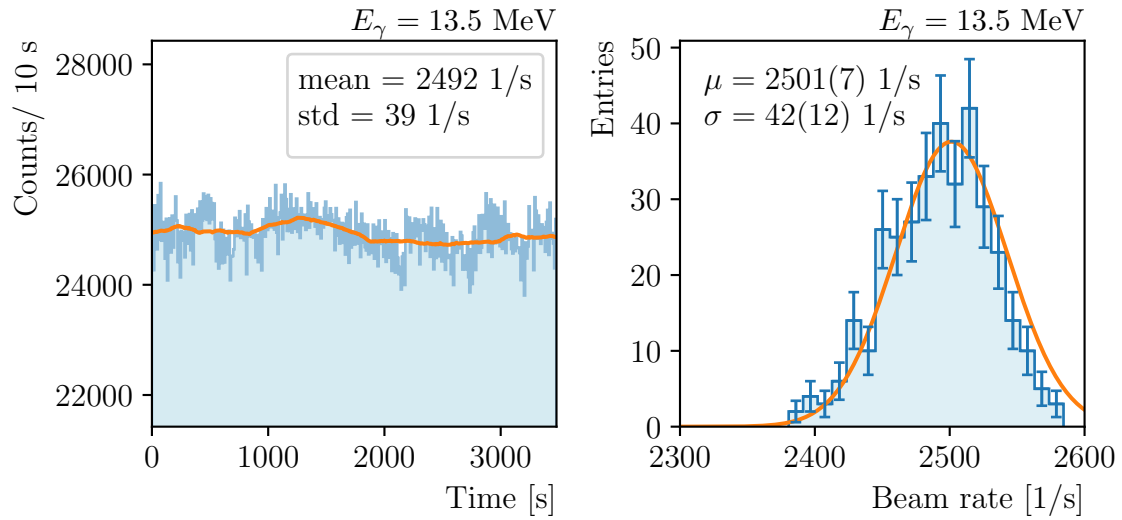


Figure 5.1: Stability of beam rate measured by MPAD with TUKAN scaler. Left: time evolution of beam rate. An average over 600 s window is annotated. Right: histogram of beam rate with a fitted normal distribution  $\mathcal{N}(x | \mu, \sigma^2)$ .

As an another method to address the stability the online-trigger rates were investigated. An example trigger rate history and stability estimation is presented in the Figure 5.2. The results obtain by both methods can be compared quantitatively after a calibration. Both methods gave the same qualitative results. The estimated trigger rate dead time was consistent with electronics dead time.

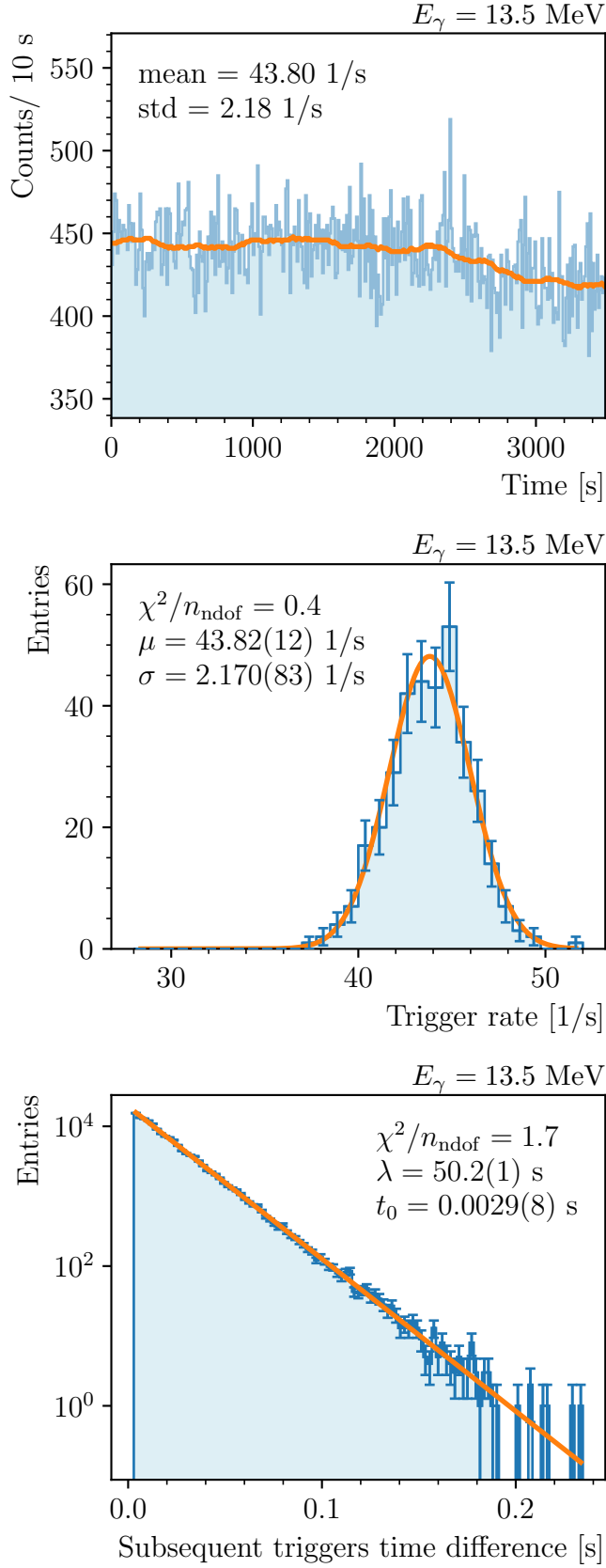


Figure 5.2: Trigger rate stability for example run with nominal energy  $\gamma$ -beam  $E_\gamma = 13.5$  MeV (the same as depicted in the Figure 5.1).

Top: time evolution of the trigger rate. An average over 600 s time windows is displayed.

Center: histogram of trigger rate with fitted normal distribution  $\mathcal{N}(x | \mu, \sigma^2)$ .

Bottom: time difference between the subsequent triggers. An exponential distribution with an offset  $\text{Exp}(t | \lambda, t_0)$  is fitted. The value of offset  $t_0$  is consistent with the detector dead time.

### 5.1.2 Energy

As noted in Section 3.4.2 the energy of the  $\gamma$ -beam was measured by the independent HPGe detector. An example spectrum measured by the detector is presented in the Figure 5.3.

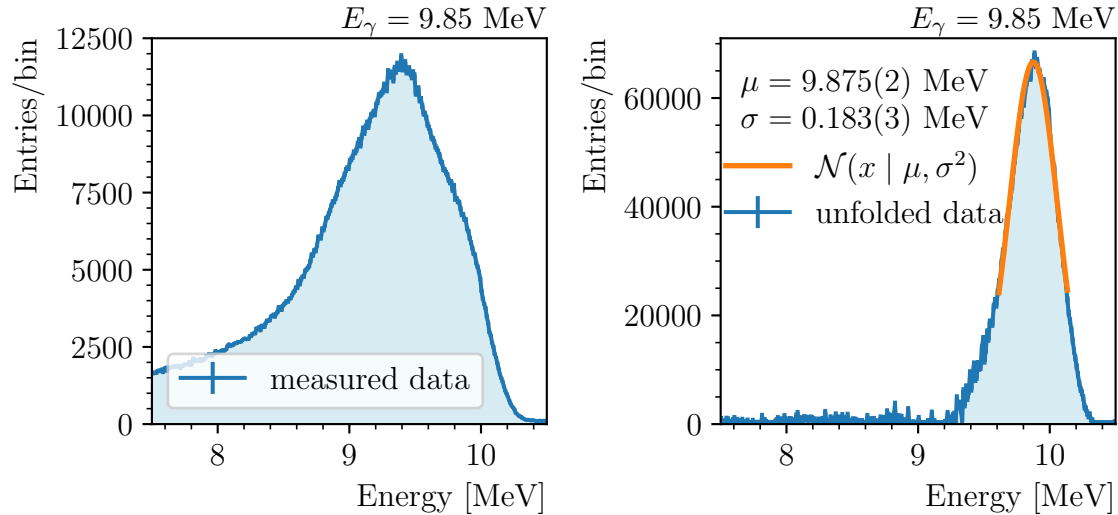


Figure 5.3: HPGe spectrum unfolding with `horst`. Left: raw HPGe spectrum. Right: same spectrum after unfolding with the HPGe response. The unfolded spectrum is skewed in the direction of lower energies. A non-skewed normal distribution is fitted to approximate the parameters of the spectrum.

As discussed in 3.4.2 the  $\gamma$ -beam energy measurements were accomplished in separate experimental runs with the use of up to 39.45 cm copper attenuators to decrease the beam intensity. The HPGe data measured this way may contain additional scattering on the attenuators event that were not present during the experimental runs with the TPC. This possibility could be studied in a separate simulation in order to correct for this effect.

At the measured energies range the measurements taken directly from the HPGe have to be statistically unfolded with the detector response is needed in order to obtain the  $\gamma$ -beam.

At the time of conducting the analysis the HPGe response matrix has been constructed only for  $\gamma$ -beam energies up to 10 MeV. The runs with energies below the 10 MeV were unfolded Magdalena Kuic, University of Warsaw with a top-down algorithm[55] using `Horst` application [56]. An example spectrum unfolding is presented in the Figure 5.3. The unfolded spectra were skewed in the direction of lower energies. As mentioned at the beginning of the section the skewness might be an artifact of a measurement method or unfolding method.

In case of energies above the 10 MeV a series of Geant4 [57] HPGe Monte Carlo simulations done by Zenon Janas, University of Warsaw were used to estimate the beam parameters with a fit. The simulation was limited to non-skewed normal distributions of  $\gamma$ -beam energies. The obtained parameters of  $\gamma$ -beam are listed in a Table 5.1.

Table 5.1: Beam distributions measured with HPGe. Results of normal distribution fit  $\mathcal{N}(E_{\gamma}^{\text{LAB}}|\mu, \sigma^2)$  to unfolded HPGe  $\gamma$ -beam energy spectrum ( $E_{\gamma} < 10$  MeV) or Monte Carlo simulation by Zenon Janas, University of Warsaw are listed ( $E_{\gamma} > 10$  MeV). The  $\gamma$ -beam nominal  $E_{\gamma}$  is used as a run identifier.

$E_{\gamma}(\text{MeV})$	Campaign	$\mu$ (MeV)	$\sigma$ (MeV)
13.5	Apr	13.47(2)	0.20(3)
13.1	Apr	13.06(2)	0.20(3)
12.3	Apr	12.26(2)	0.19(3)
11.9	Apr	11.87(2)	0.20(3)
11.5	Apr	11.48(2)	0.19(3)
9.85	Apr	9.782(2)	0.203(3)
9.85	Aug	9.875(2)	0.183(3)
9.56	Aug	9.602(2)	0.170(3)
9.36	Aug	9.390(3)	0.178(3)
8.86	Aug	8.897(2)	0.160(3)
8.66	Aug	8.690(1)	0.164(2)

### 5.1.3 Alignment

Knowing the beam alignment is not only important for correctly establishing the coordinate system and reaction kinematics but also for removing background events not associated with the beam by means of fiducial cuts or calculating acceptance corrections.

While the beam alignment is taken into a careful consideration during setting up the experiment and a significant effort is taken in order to minimize the chamber misalignment with respect to the beam axis using available equipment (Section 3.4.1), any apparent misalignment prevailing these corrections can be measured and corrected from the experimental data during the offline data analysis step.

Since in case of self-triggering mode (as used during the experiment) only relative position along the drift axis is measured, in that mode it is impossible to assess the beam misalignment or width in drift direction — the estimates from the experimental data are limited to the projection of beam direction on the readout plane. Figure 5.4 presents an example beam tilt fit to the experimental data.

After estimating the beam tilt parameters a transformation to a coordinate system associated with the beam is possible (Appendix B). This system is convenient to study the distributions of events along and transversal to the beam axis in order first to confirm the correctness of used parameters and second find the characteristics of the beam such as beam width or possible loss of intensity in the medium. The distributions are presented in the Figure 5.5. The obtained beam width is consistent with the diameters of the used collimator (10.5 mm collimator at approximately 10 m from the chamber resulting in around 14 mm width at the chamber.)

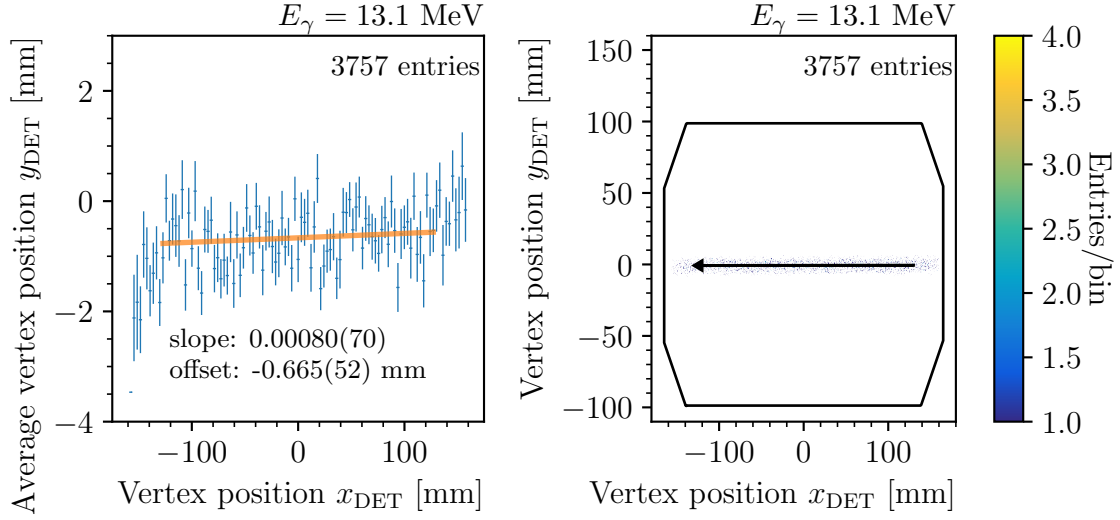


Figure 5.4: Beam tilt correction. Left: beam tilt fitted to the 2-prong event's vertex distribution profile along  $x_{\text{DET}}$  (nominal beam direction). Right: beam direction including fitted beam tilt correction. The beam direction arrow is overlaid on 2-prong event's vertex distribution on the readout plane.

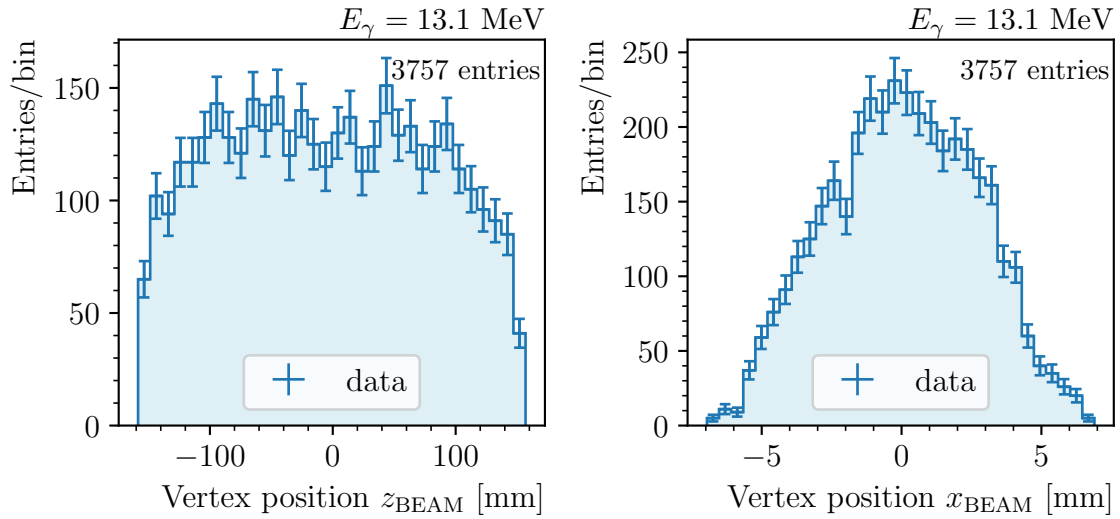


Figure 5.5: Beam spatial distributions after beam tilt correction. Left: distribution of 2-prong events' vertices along  $z_{\text{BEAM}}$  (along the projection of the beam direction on the readout plane). The lower number of entries at the ends of the distributions are expected due to fiducial cuts rejection of not-fully-contained events at the edges of the active volume. Right: distribution of 2-prong events' vertices along  $x_{\text{BEAM}}$  (perpendicular to the projection of the beam direction on the readout plane). The distribution corresponds to the measured beam width on the readout plane.

## 5.2 Data quality

Data quality analysis tries to assess all kinds of effects and possible corrections to the data. Although it does not provide any result of direct physical importance, the obtained information is valuable on its own as it provides the insight into workings of the experimental setup and creates opportunity to early detect problem that would arise later during the physical analysis.

A very important aspect of the data quality studies is building the confidence for the results of the physical importance. The role of the data quality assessment in this work is even more significant as due to the novelty of the detector it is done on the data from one of the first physical experiments conducted with the WARSAW TPC [21, 58]. It is also the first data analysis of this depth done in the scope of the WARSAW TPC.

### 5.2.1 Drift velocity correction

One of the assumptions taken during the reconstruction of data is the value of drift velocity. While the value can be simulated or measured in dedicated laboratory test its value at the time of the experiment can only be estimated as it depends on the experimental settings and environment such as stability of gas flow affecting the medium density or stability of the output HV affecting the electric field. The nominal values used during the reconstruction were simulated with Magboltz [59] by Magdalena Kuich, University of Warsaw. The obtained drift velocity dependence on electric field is presented in the Figure 5.6.

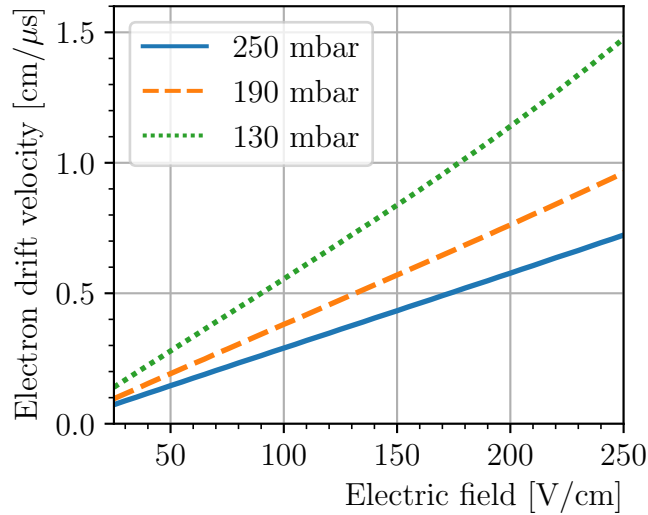


Figure 5.6: Electron drift velocity in  $\text{CO}_2$  simulation with Magboltz [59]. The assumed temperature is 293 K. The displayed series corresponds to the nominal pressure values the detector was operating with during the experiment. A small variation of real drift velocity with the regards of the simulation is possible given the uncertainties of characteristics of electric components used in the experimental setup and finite gas-flow stability.

The post-experiment offline analysis presents an opportunity to examine and possibly corrected the drift velocity estimate. The basis of this correction is the fact that the drift velocity affect only the position of tracks along the drift axis, the other planar coordinates are unaffected by it. Assuming the correct drift velocity the events endpoint should be distributed on a sphere (for a given energy), or when projected on a plane normal to the beam direction on a circle. In case of wrong drift velocity the coordinate along the drift will be affected and the circle would be deformed into an ellipse.

The drift velocity has been examined using the described technique and an example ellipse fit is presented in the Figure 5.7.

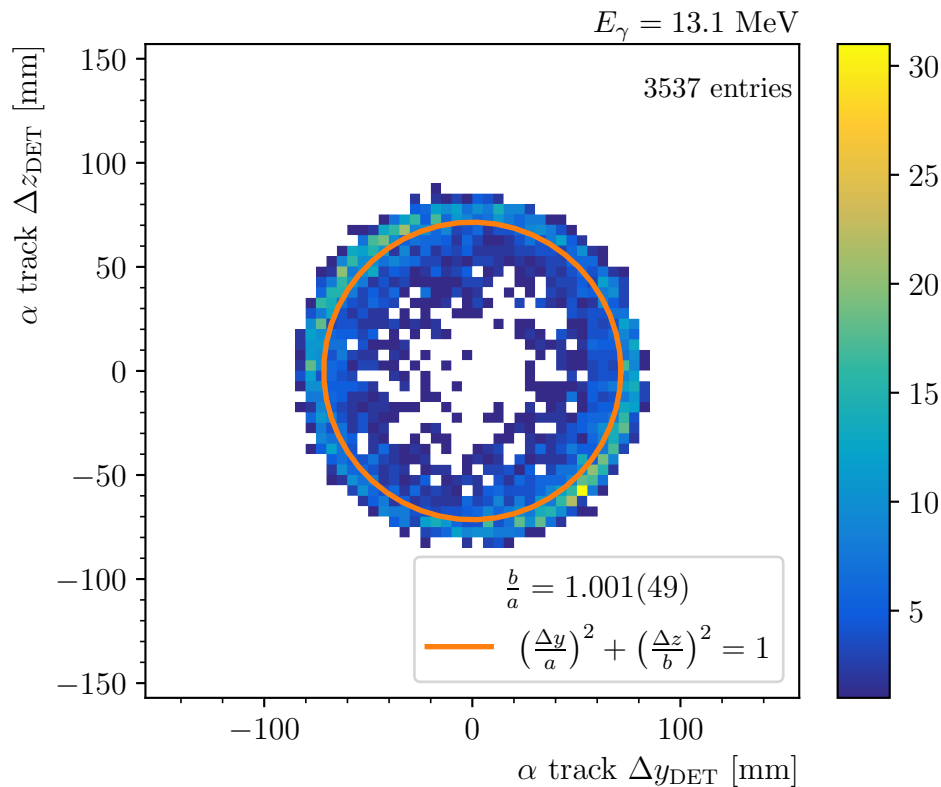


Figure 5.7: Drift velocity correction estimation. A circular distribution of event endpoints is deformed by wrong drift velocity into an ellipse. An ellipse is fitted in order to correct the drift velocity. Due to the use of self-triggering the  $z_{\text{DET}}$  component is measured only with relative precision, since the plot is presented as the difference of track endpoint coordinate with respect to the vertex coordinate. The distribution of events around the circle is described in Section 5.6.2.

The drift correction was expressed as a multiplicative factor and listed in Table 5.2. Note that in all cases the resulting correction is small and the uncorrected values are within the  $\pm 1\sigma$  statistical uncertainties.



Table 5.2: Drift velocity correction factors. The nominal value used during the reconstruction is listed as well as a correction expressed as a multiplicative factor.

$E_\gamma$ (MeV)	drift velocity cm/ $\mu\text{s}$	correction factor
13.5	0.405	1.002(77)
13.1	0.405	1.000(48)
12.3	0.646	0.982(50)
11.9	0.646	0.977(37)
11.5	0.646	1.022(42)
9.85	0.500	1.01(10)

## 5.2.2 Fiducial cuts

Fiducial cuts are applied in order to select a specific region of the detector volume where the detector’s performance is well understood and reliable. This helps to reduce the influence of edge effects, uncertainties in detector response near the boundaries, and background contamination from events occurring outside the fiducial volume and not correlated with the beam.

The fiducial region is defined within the detector volume based on geometric considerations and the knowledge of the detector’s response characteristics. It is typically chosen to be away from the detector’s physical edges or other regions with potential artifacts.

For the current studies following fiducial cuts were used:

1. Vertex position — only events with vertex within a given distance from the beam axis are accepted. The parameters of the cut are adjusted for the beam tilt and estimated beam width. This cut is presented and discussed in the Figure 5.8.
2. Border padding — only events with the vertex and all the endpoints farther than a given distance from the active area border are accepted. A conservative 5 mm padding is used. This cut is presented and discussed in the Figure 5.9,
3. Global Z-span — only events with the vertex and all the endpoints withing the signal region are accepted. This cut is related to the event preprocessing method Section 4.1.1 relaying on a “pedestal region” for the baseline correction. This cut is presented and discussed in the Figure 5.10,
4. Relative Z-span — only events contained within half of the drift cage are accepted. This cut is aimed to remove events that could hit cathode or the GEM plane. This cut is presented and discussed in the Figure 5.11

The fiducial cuts were applied in an “all of” sequence, that means an event rejected by any of the fiducial cut in the sequence will be removed from further analysis. For practical reasons the sequence was ordered and following a short-circuit evaluation logic where only events accepted by a fiducial cut are passed to the next cut in sequence, thus potentially reducing the number of entries with every successive fiducial cut. The

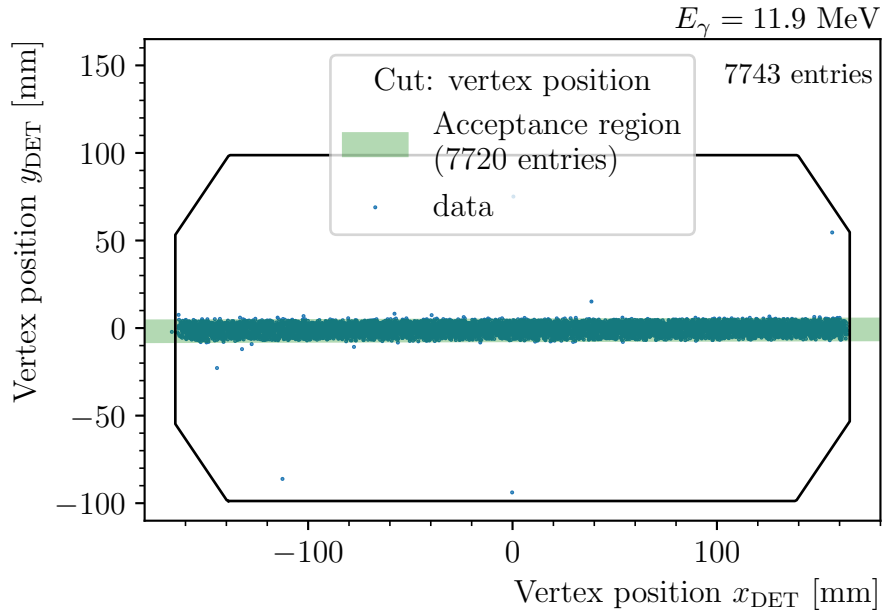


Figure 5.8: Fiducial cut: vertex position. Only events with vertex along the beam line are accepted. The beam line position assumed by the cut is corrected for the beam tilt and offset for every run. The main purpose of this cut is to remove the events not originating from the  $\gamma$ -beam such as background  $\alpha$ -particles for the detector walls.

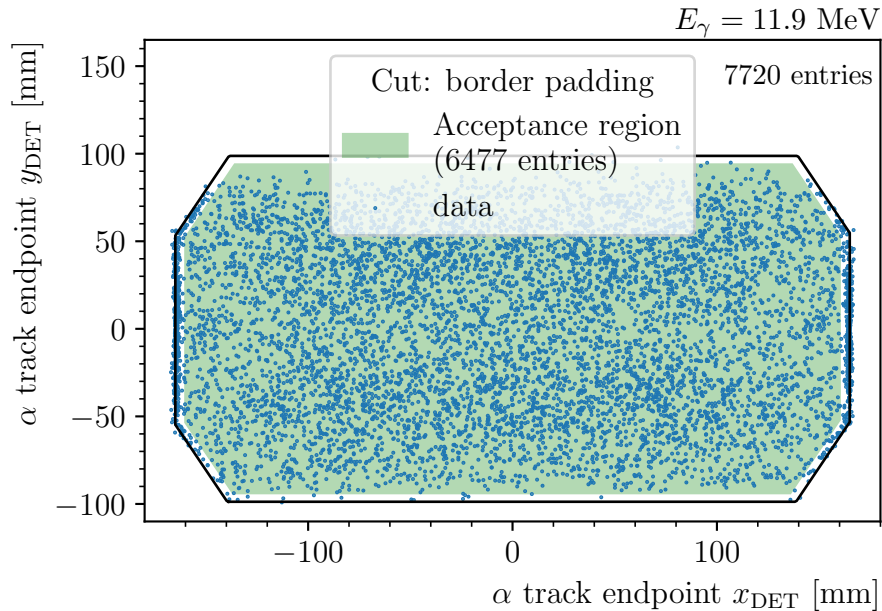


Figure 5.9: Fiducial cut: border padding. Only events with vertex and all track end-points within minimal distance of 5 mm millimeters to readout border are accepted. The main purpose of this cut is to reject the events that might be not-fully contained within the detector XY-plane.

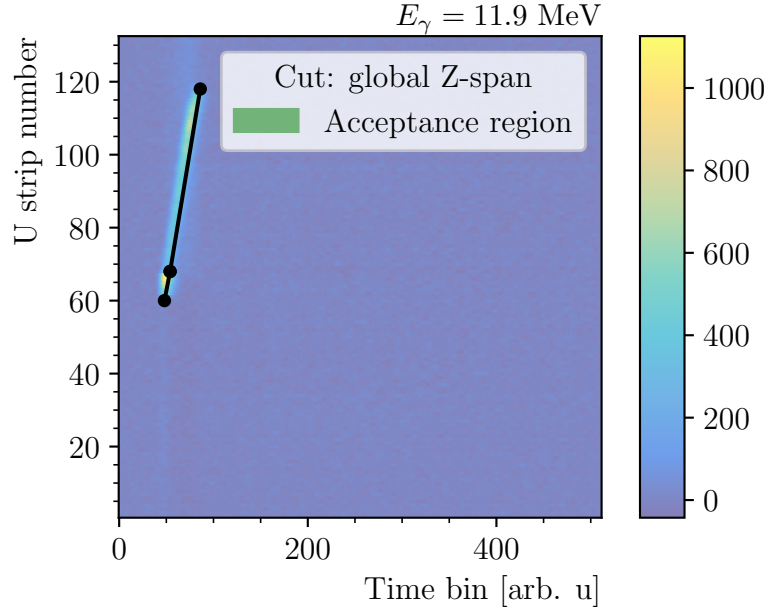


Figure 5.10: Fiducial cut: global Z-span. Only events with vertex and all track endpoint inside the signal region are accepted. The main purpose of this cut is to reject the events that might be not fully contained in the electronics buffer, affected by high electronics noise at the end of buffer history or might have incorrectly subtracted the pedestal (baseline). The figure shows only the U-strip direction projection of an example event.

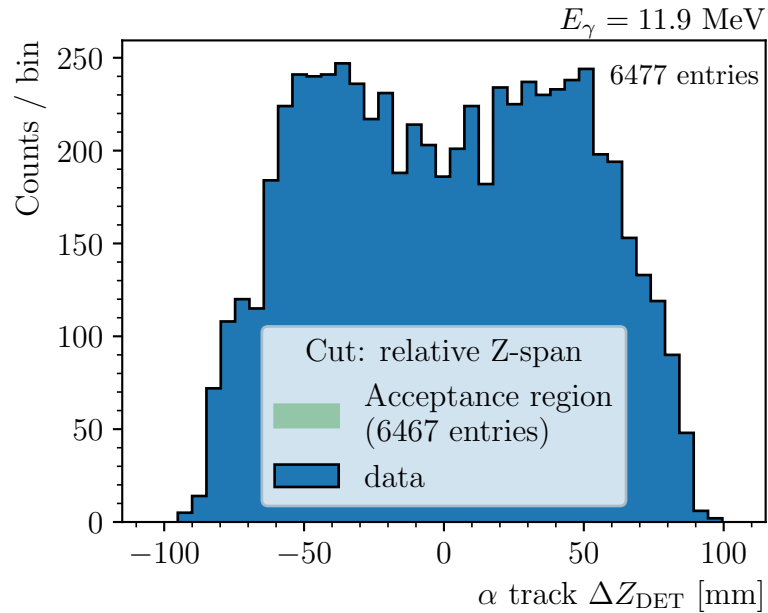


Figure 5.11: Fiducial cut: relative Z-span. Only events with relative vertical distance between the endpoints and vertex lower than half of the drift cage length are accepted. This cut ensures that the events did not hit the cathode nor the GEM plane.

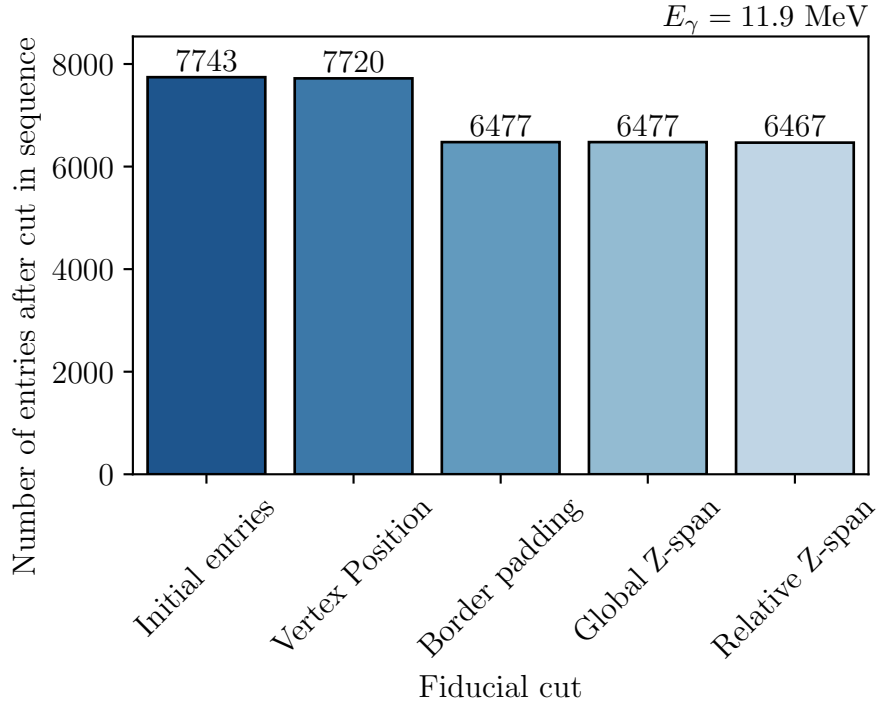


Figure 5.12: Fiducial cuts sequence. A number of events after each cut in the sequence is given. The border-padding cut removes the most events.

number of events from an example run after every fiducial cut in a sequence is presented in the Figure 5.12.

While the final number of events passing the cut sequence is independent on the sequence order, the cut ordering can be optimized for shorter processing time by putting the most restrictive cuts earlier in the sequence. Given the limited number of events in this study the ordering was not optimized as the event processing times were not considered a limiting factor.

### 5.2.3 Acceptance correction

While the purpose of the fiducial cuts is to remove the events that can't be properly studied due to the limitations of detector design and used method, they don't address the problem that the distribution of such events is not uniform. For instance the geometrical cuts aiming to select only events fully contained inside the detector volume inherently prefer the events that can be contained on smaller physical volume — with a practical implication that a fraction of lower energy events removed by the cuts will be smaller than a fraction of higher energy events with longer tracks. Depending on the physicists' community this problem is called either acceptance or efficiency of the detector.

Given different characteristics of the fiducial cuts applied estimating their exact influence on the event distributions can be hard to predict and therefore is usually studied by means of the Monte Carlo simulations. In case of the current analysis a general trend can be predicted that the vertex position and border padding cuts will be

the most actively removing the events at the active area border resulting in preference for lower energies and hard to express analytically effect on the angular distributions.

The problem of acceptance is usually addressed in two ways:

1. Select a subsample of the data not affected by the acceptance. The distributions of important event characteristics should be unaffected by the acceptance and therefore no extra corrections for that effect are needed. The disadvantage of this method is the further reduction of total number of entries. Another possible shortcoming of this method is that the unaffected region can be difficult to determine without adaptational simulations.
2. Numerical correction. Instead of working on an unaffected subsample a correction to the whole sample can be applied to adjust the acceptance effect. The effect of acceptance is usually studied over a series of simulations from which the acceptance correction matrix is established. The correction matrix is then applied to the sample in order to estimate the real distributions of the events' characteristics.

In the current analysis the first approach of selecting unaffected subsample was chosen. The choice was dictated by the fact that the availability of a proper simulation framework is only a very recent addition (May 2023) and framework has not been adapted for the acceptance studies yet.

In order to select the acceptance-unaffected region the density of event was studied. The Figure 5.13 presents the number of events with vertex within a range from the detector center. The decrease of the event density at the active area indicates the need to address the acceptance problem. Similarly a region of constant event density can be expected to present distributions not affected by the acceptance.

In practice the limited acceptance has been addressed by after fiducial cuts applying another cut on vertex position and accepting only vertices within a given distance from the detector center. The illustration of this cut is depicted in the Figure 5.14. The exact values of the limiting distance and the resulting reduction of events is presented in the Table 5.3.

Table 5.3: Acceptance unaffected subsample selection. The subsamples were selected by accepting only events with vertex  $x_{\text{DET}}$  coordinate within limiting distance from the detector center. The fraction of events removed by the cut is listed.

$E_\gamma$ (MeV)	limiting distance (mm)	number of entries reduction
13.5	120	16%
13.1	115	20%
12.3	100	27%
11.9	110	20%
11.5	115	16%
9.85	100	29%
9.56	130	14%

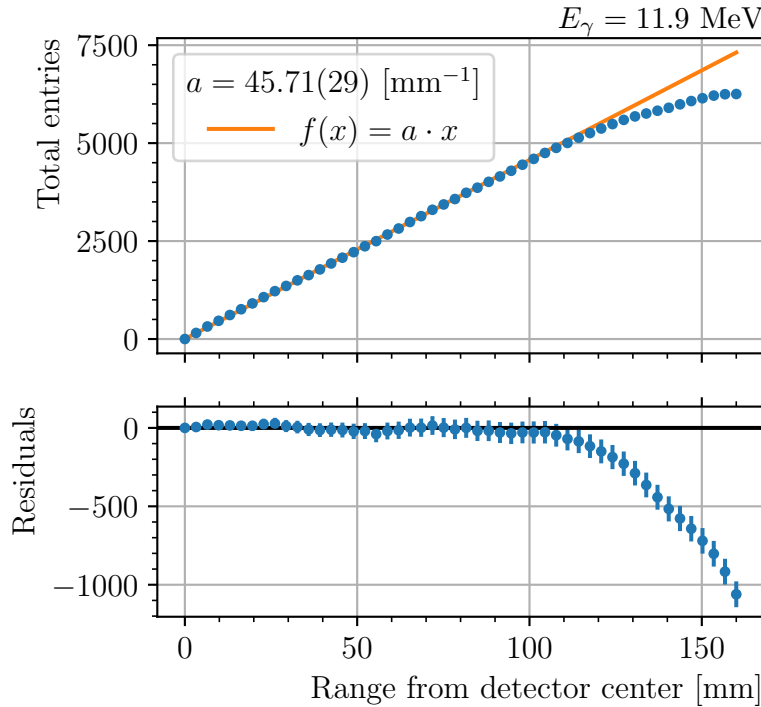


Figure 5.13: Density of reconstructed events. Number of events with vertex within window from a detector center is presented. The density of events is lower at the edges as the events are removed from the border padding fiducial cut. The distributions of event characteristics such as angular distributions are expected to be non-uniformly affected.

### 5.3 Event selection

The method of choice for distinguish the nuclear reaction including distinguishing similar reactions with different isotopes is by comparing their characteristic Q-value. The Q-values for considered reactions are listed in Table 5.4. Given that the current event reconstruction provides only information about tracks position and no information about momenta and energies needed to calculate the Q-value another approach had to be taken.

Basing on the available information two selection criteria were proposed:

1. Discrimination by topology (number of prongs) - the total number of reconstructed in an event can be used to differentiate between  $O(\gamma, \alpha)C$ , the  $^{12}C(\gamma, 3\alpha)$ , scattering events and background  $\alpha$  emission as they differ by the number of charged particles involved. This criterion is not enough for isotopic selection.
2. Discrimination by track length - the criterion is related to the Q-value with the advantage of operating without an energy scale and explicit hypotheses. An isotopic selection is possible as this selection is derived from the Q-value differences.

As the  $^{16}O(\gamma\alpha)^{12}C$  reaction is the main point of the current work, an event selection for a 2-prong events was used given that the reaction produces two charged products.

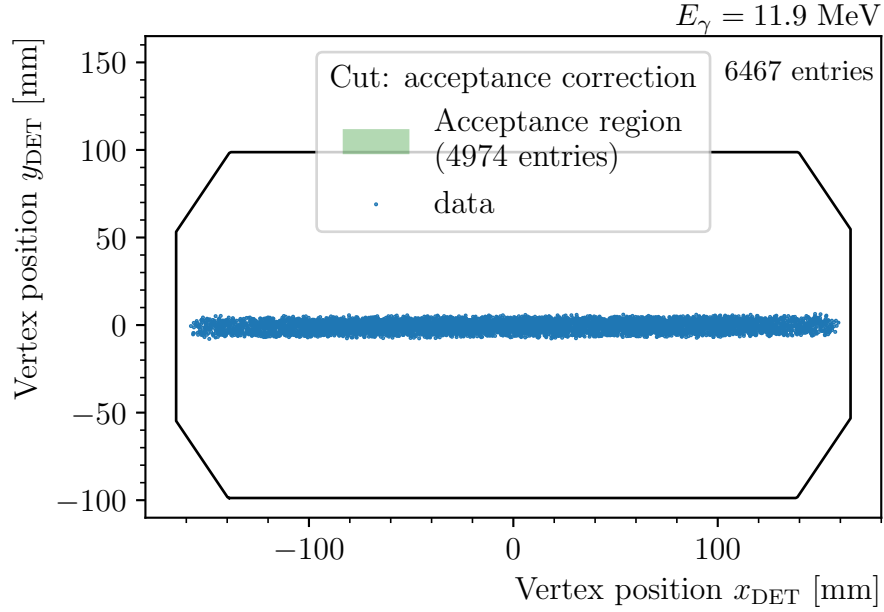


Figure 5.14: Acceptance cut. A sample unbiased by the acceptance effects at the edges of the active area is achieved by selecting events with vertex  $x_{\text{DET}}$  coordinate withing given distance from the detector center. The density of vertex  $x_{\text{DET}}$  is constant after the selection.

Table 5.4: Q-values for selected photodisintegration reactions. Reconstructing the Q-value is the method of choice to differentiate between different reactions.

Reaction	Q-value (MeV)
$^{16}\text{O}(\gamma, \alpha)^{12}\text{C}$	-7.162
$^{17}\text{O}(\gamma, \alpha)^{13}\text{C}$	-6.359
$^{18}\text{O}(\gamma, \alpha)^{14}\text{C}$	-6.227
$^{16}\text{O}(\gamma, p)^{15}\text{N}$	-12.128
$^{12}\text{C}(\gamma, 3\alpha)$	-7.274
$^{12}\text{C}(\gamma, \alpha)^8\text{Be}$	-7.367

Afterwards, in order to differentiate between a  $^{17,18}\text{O}(\gamma\alpha)^{12,13}\text{C}$  that are described the same two-charged-products topology but is characterized by different masses, a track selection was used. To achieve this a map of track length has been constructed and a cluster corresponding to oxygen-16 photodisintegration hypothesis has been found. An example selection by track length is depicted in the Figure 5.15.

The Table 5.5 lists the reactions identified by the track-length selection on 2-prongs selection, the fractions of events belonging to given reaction cluster over the total number of 2-prong events are given. Note that the 2-prong sample could be contaminated by the 3-prong events due to mis-reconstruction of number of the track number. A small contamination of  $^{12}\text{C}(\gamma, 3\alpha)$  events is visible. This contaminated is the direct effect of the event misidentification discussed in Section 4.4.1.

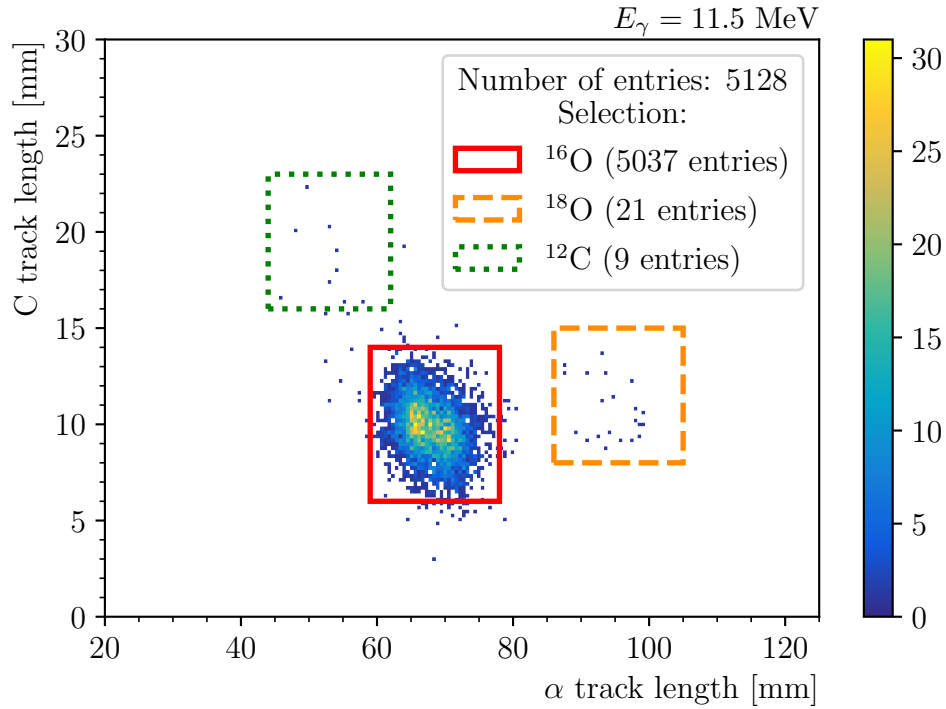


Figure 5.15: Isotope selection on events reconstructed as 2-prongs. The following reactions can be selected from a 2-prong sample:  $^{16}\text{O}(\gamma, \alpha)^{12}\text{C}$  ( $^{16}\text{O}$  series),  $^{17,18}\text{O}(\gamma, \alpha)^{13,14}\text{C}$  ( $^{18}\text{O}$  series), and misidentified 3-prong  $^{12}\text{C}(\gamma, 3\alpha)$  ( $^{12}\text{C}$  series) reaction.

Table 5.5: Percentages of reactions selected by track lengths in a 2-prong sample. The  $^{12}\text{C}(\gamma, 3\alpha)$  reaction is a misidentification of 3-prongs.

$E_\gamma$ (MeV)	Sample selection in %		
	$^{16}\text{O}(\gamma, \alpha)^{12}\text{C}$	$^{17,18}\text{O}(\gamma, \alpha)^{13,14}\text{C}$	$^{12}\text{C}(\gamma, 3\alpha)$
13.5	82.0	0.0	0.0
13.1	94.1	0.0	0.0
12.3	95.4	0.0	0.0
11.9	96.7	0.9	0.5
11.5	98.2	0.4	0.2
9.85	70.1	18.6	4.2
9.56	45.0	42.8	2.2
8.66	3.4	84.8	1.8

Given that the limited number of entries was reconstructed and in the  $E_\gamma = 8.66$  MeV runs the desired  $^{16}\text{O}(\gamma, \alpha)^{12}\text{C}$  constitutes only a small fraction of total events, the available number of entries was not enough to conduct a meaningful studies for the  $^{16}\text{O}(\gamma, \alpha)^{12}\text{C}$  reaction and these runs were not further analyzed in that regard.



## 5.4 Energy scale

### 5.4.1 Energy reconstruction

Given the particle energy and momentum are not provided during the reconstruction step, their values had to be established during the analysis step. In principle the particle energy could be obtained from an information about the track in two ways:

1. From a Bragg curve to the reconstructed charge along the track.
2. From an energy-range table and the reconstructed track length.

Both of these methods rely on a used model of ion transport in matter such as SRIM [14]. In case of the manual reconstruction only track length information is produced, so the energy-range table calculation can be used. A SRIM based energy-range table used in this study is presented in the Figure 5.16.

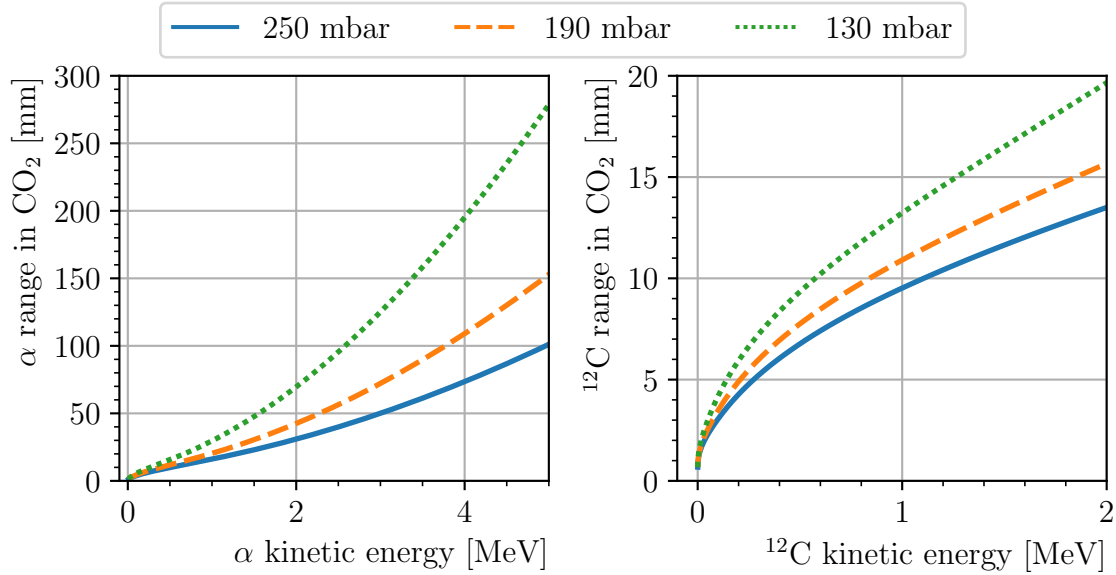


Figure 5.16: Ion range vs energy dependence in CO<sub>2</sub> for pressures used during the experiment and temperature of 293.15 K. Left: Dependence for  $\alpha$  particle. Right: dependence for  $^{12}\text{C}$ . Values obtained from SRIM [14] and corrected for range cut-off at 1 keV ion energy threshold to accommodate for limited sensitivity of the detector.

The energy reconstruction was applied to the  $^{16}\text{O}(\gamma, \alpha)^{12}\text{C}$  selected 2-prong data. An observation has been made that the distribution of energies in case of  $\alpha$  and  $^{12}\text{C}$  have significantly different variances, that can impact the resolution of quantities depending on them such as excitation energy  $E_x$  or center of mass energy  $E_{\text{CM}}$ . To calculate such quantities two procedures were proposed:

1. Calculate energies and momenta for both  $\alpha$  and  $^{12}\text{C}$  tracks using the energy-range tables.
2. Calculate energy and momentum only for  $\alpha$  tracks using the energy-range tables and obtain the energy and momentum for  $^{12}\text{C}$  using the energy-momentum conservation law in a CM.

The variances of excitation energy  $E_x$  obtained with the two methods has been compared. A comparison for an example  $\gamma$ -beam energy is depicted in the Figure 5.17. As the distribution obtained using the conservation law resulted in much lower variances of excitation energy  $E_x$ , it was chosen that this method will be utilized in the present analysis.

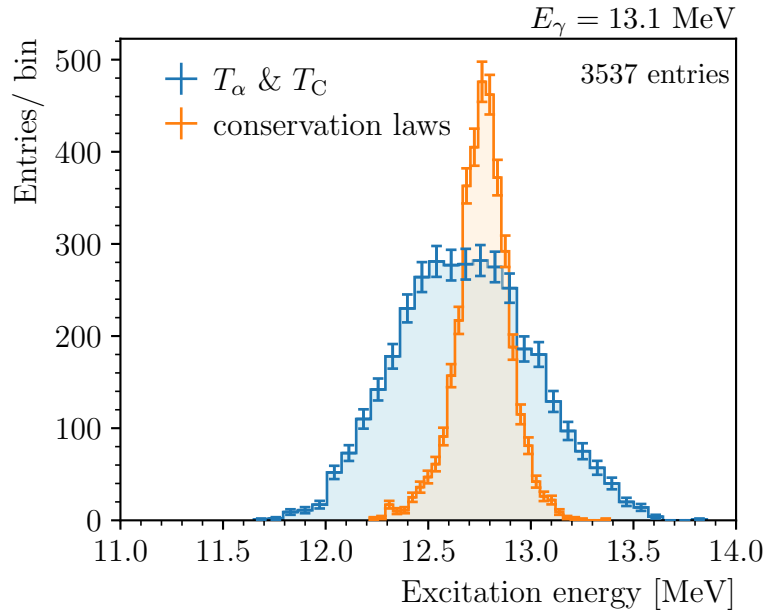


Figure 5.17: Energy reconstruction methods for 2-prong events. The first method assumes obtaining kinetic energies for both particles from energy-range tables. The other “conservation laws” method assumes obtaining the kinetic of the  $\alpha$  particles (the longer track in an event) and calculating the the other from energy-momentum conservation principles. As the resolution of reconstruction the length is better for the  $\alpha$  particles the “conservation laws” method also results in better resolution.

### 5.4.2 Energy calibration

It was noted that the values of energy obtain for  $\alpha$ - $^{12}\text{C}$  candidates differ significantly from the values obtain from kinematics calculation for a given  $\gamma$ -beam energy. The values obtained from the energy-range tables seemed to be lower by 100-200 keV for all  $\gamma$ -ray beam energies investigated. Possible explanations for this effect include:

- Reconstruction method systematic error. With the manual reconstruction experts were tasked with finding the end of the tracks on displayed representation of events.
- Charge collection sensitivity limits and DAQ electronics limits (for instance the ADC range). The detection and DAQ processes results in an effective lower limit on the charge that can be detected, which results in cut-off deposited charge at the end of the tracks and this smaller track lengths (ion ranges).

- Underestimation of ranges in SRIM tables. A number of works [60] mentioned various discrepancies between measurements and SRIM, and identified further need to recalibrate the obtained values.

A linear correction to the  $\alpha$  particle kinetic energy of selected  $^{16}\text{O}(\gamma, \alpha)^{12}\text{C}$  events was proposed. The excitation energies of selected resonance nuclear states in  $^{16}\text{O}$  were used to calculate the nominal  $\alpha$  particle kinetic energies for the fit. The resonance states chosen used for the calibration are listen in Table 5.6.

A fit of energy calibration parameters is presented in the Figure 5.18. Note the obtained calibration values are valid only for the used event reconstruction method, energy reconstruction method and selected reaction. For instance the parameters obtained with this procedure might not be directly applicable for establishing energy scale of  $^{12}\text{C}(\gamma, 3\alpha)$  events.

Table 5.6: Resonance states of  $^{16}\text{O}$ . Only the states used in the energy calibration are listed. The excitation energy  $E_x$ , width  $\Gamma$ , and spin and parity  $J^\pi$  are given. The values taken from [61].

$E_x$ (MeV)	$\Gamma$ (keV)	$J^\pi$
13.090(8)	130(5)	$1^-$
11.520(4)	71(3)	$2^+$
9.8445(5)	0.625(100)	$2^+$

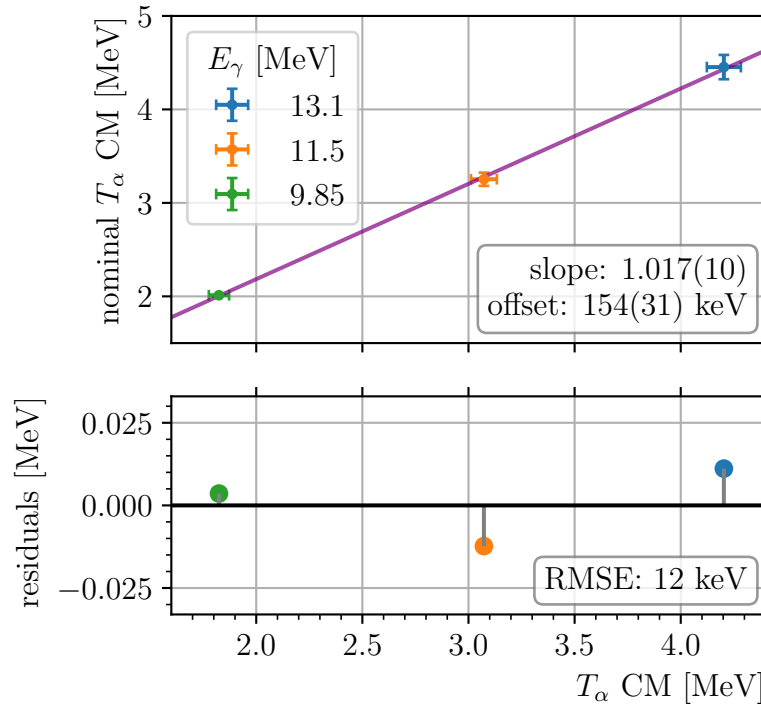


Figure 5.18: Energy calibration. A linear calibration was obtained for oxygen-16 photodisintegration events between the  $\alpha$  particle kinetic energy  $T_\alpha$  in CM obtained from experimental data and nominal values of  $\alpha$  particle kinetic energies calculated for corresponding resonance states from Table 5.6.

### 5.4.3 Energy resolution

With the energy scale established the energy resolution can be estimated. The value can be estimated as a variance between reconstructed  $\alpha$  tracks between different experts on the paired dataset (Section 4.4.2). The estimated alpha kinetic energy resolution is equal 47(14) keV. Due to limited size of the paired dataset only an averaged estimate is provided for all the energies, that does not include any dependency on the  $\gamma$ -beam energies or orientation in space. The estimated resolution may differ from the resolution of the full dataset as the contributions of experts are different. The resulting excitation energy resolution is 63(19) keV.

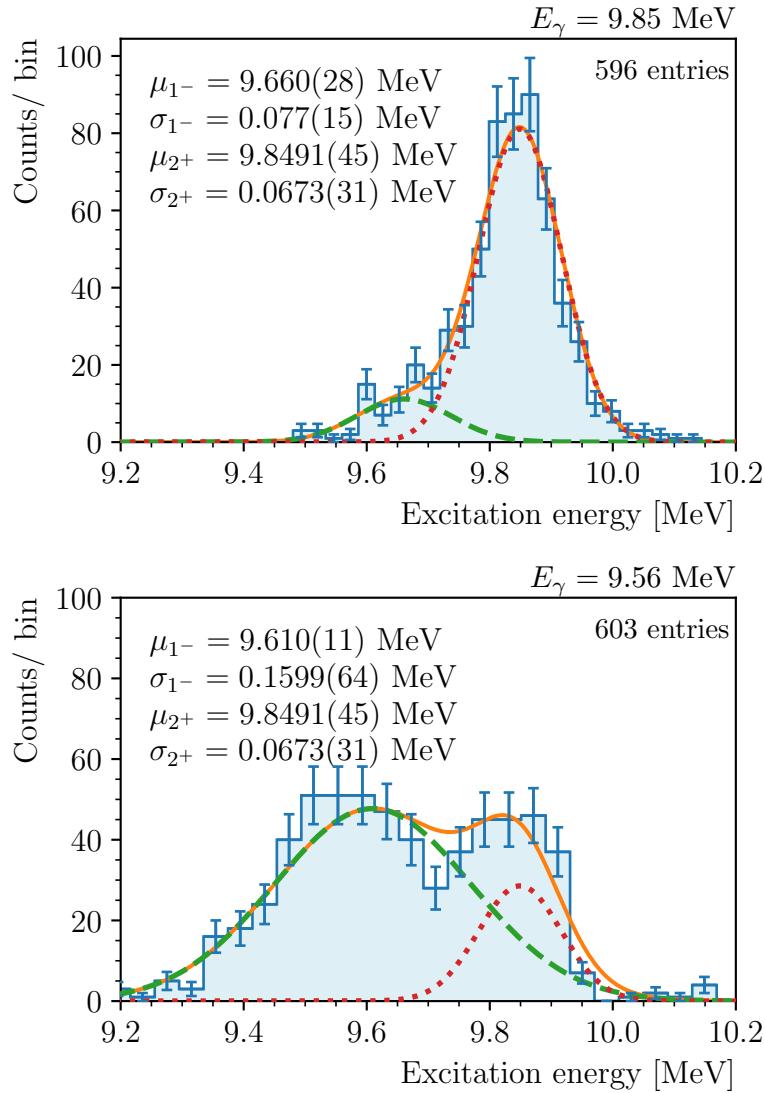


Figure 5.19: Energy resolution obtained from the fit to the reconstructed data on a narrow ( $\Gamma = 0.625(100)$  keV) resonance  $2+$  at  $E_x = 9.8445(5)$  MeV. The fit was done on two runs  $E_\gamma = 9.85$  MeV and  $E_\gamma = 9.56$  MeV simultaneously. The position of the second peak from  $1-$  is different in each run as width of the state isn't narrow and the peak is deformed with the shift of  $\gamma$ -beam energy. The estimated energy resolution is 67(3) keV. The estimated resolution includes both the resolution of the measurement and reconstruction method.

As another estimate a width of the peak at a narrow resonance can be taken. The dataset contain such resonance at  $E_x = 9.8445(5)$  MeV (see Table 5.6) in runs  $E_\gamma = 9.56$  MeV and  $E_\gamma = 9.85$  MeV. In both datasets the measured spectrum contains another peak of other broad resonance states ( $E_x = 9.585(11)$  MeV,  $\Gamma = 420(20)$  keV,  $J^\pi = 1^-$ ) [61].

The result of the fit to the resonance is presented in the Figure 5.19. The excitation energy resolution estimated this way has value of  $67(3)$  keV and takes into account both the resolution of the measurement as well as the resolution of reconstruction. The resolutions obtained with both methods are compatible with each other.

It is worth emphasizing that the obtained detector energy resolution is much better than the width of the  $\gamma$ -beam spectrum. The importance of this fact is that the measured events can be selected by the energy to achieve better coarsening than the beam spectrum width, so every experimental point can contribute with several energy points instead of providing just one energy point averaged on a broad  $\gamma$ -beam spectrum measured by an auxiliary detector.

With the limited number of entries in the present study this energy selection may be not very practical, with a very notable exception of the run with the nominal  $\gamma$ -beam energy  $E_\gamma = 11.9$  MeV. In this particular run the broad  $\gamma$ -beam spectrum is located in a valley of cross-section between two resonance states of  $^{16}\text{O}$  and events in a very broad energy range were detected. The energy distribution observed during this run is depicted in the Figure 5.20

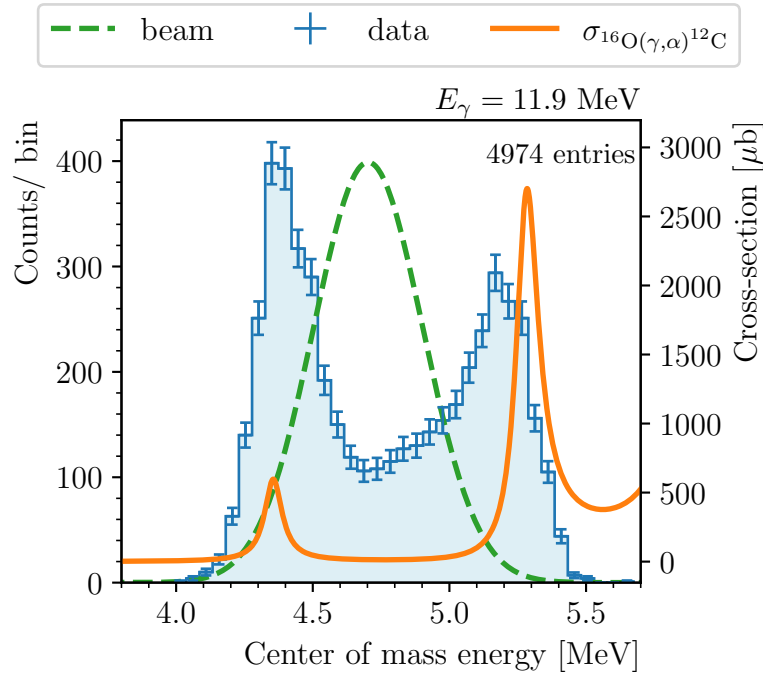


Figure 5.20: Energy spectrum measured during run  $E_\gamma = 11.9$  MeV. The broad  $\gamma$ -beam spectrum is in the cross-section valley region between two resonance state, resulting in a very broad energy range of detected events. The detector resolution ( $67(3)$  keV) is significantly better than the width of  $\gamma$ -beam spectrum and event selection by energy is possible. This experimental point can be split into several energy points. The cross-section taken from [1]. The  $\gamma$ -beam parameters are given in Table 5.1.

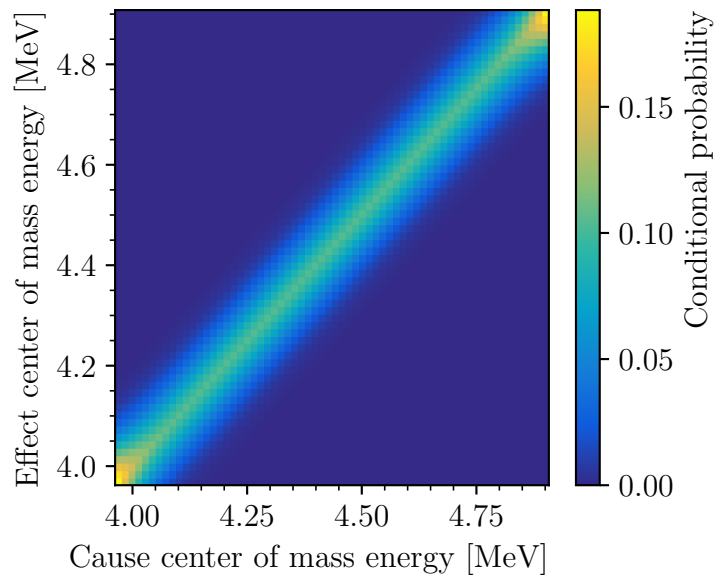
### 5.4.4 Energy unfolding

In order to reduce the influence of non-fundamental detector and reconstruction effects or artifacts an unfolding [39] can be employed.

For recovering the energy a simple response matrix was constructed assuming the constant resolution 67(3) of keV for all the energies and operating on data after acceptance correction, energy reconstruction and calibration.

A number of unfolding algorithms implemented in RooUnfold [62], ROOT's TSpec-trum and TUnfold [63], PyUnfold [64] was considered. The iterative Bayesian [65] approach was chosen due to its stability on the set of simple statistical Monte Carlo simulations of experimental distributions. An example of normalized response matrix used in the study is presented in the Figure 5.21.

Figure 5.21: Normalized detector response matrix used for iterative Bayesian unfolding. Only resolution effect is included as all other corrections were expected to be handled separately. A resolution of 67(3) keV is modelled with 10 keV granularity.



Once the response functions of the detector and reconstruction method is more thoroughly studied with a Monte Carlo simulations or increased dataset of experimental data, the response matrix can be updated with resolution depending on the energy and incorporate other aspect such as energy correction and acceptance. Usually a unified approach is preferred over splitting all the unfolding effects into separate components in order to simplify the handling of uncertainties.

The results of the energy unfolding applied to all the analyzed experimental runs are presented in the Figure 5.22.

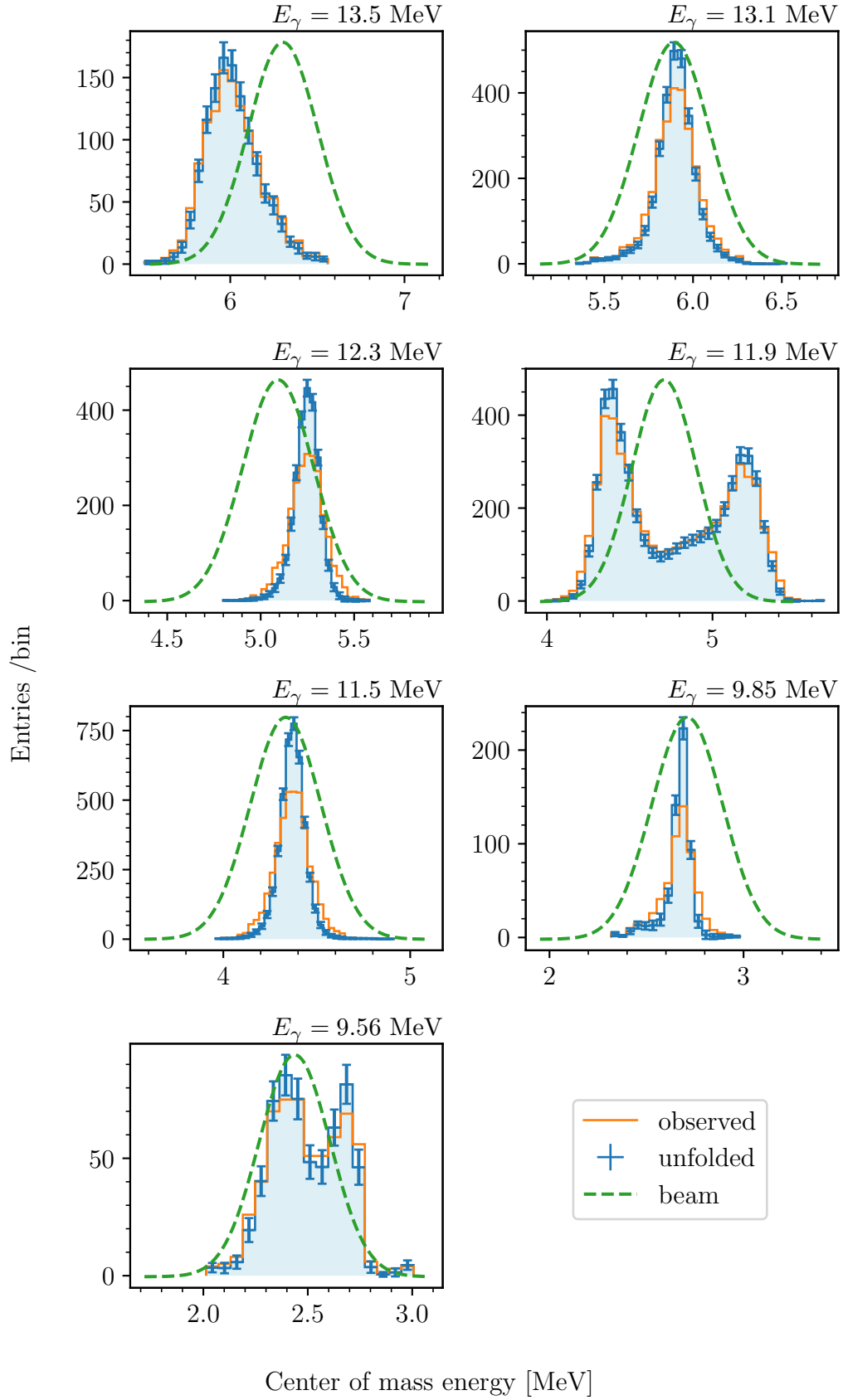


Figure 5.22: Center of mass energy after applying energy reconstruction, calibration and unfolding. The corresponding  $\gamma$ -beam energy spectra are presented for each run.

## 5.5 Response uniformity

The uniformity of the detector response is an important data quality concern. The uniformity of response touches many different aspects such as distribution of the reactions across the chamber or unexpected relations between observables and position. For instance the event reconstruction quality may depend on the orientation in space if the granularity of the readout is different in some directions, which is the case of the WARSAW TPC readout.

Some of the uniformity aspects were already mentioned in the earlier parts of this work, such as the distributions of event vertices along the beam direction (Figure 5.5) or distribution of the event endpoints across active area (Figure 5.9).

Another type of the uniformity is the uniformity in azimuthal  $\phi_{\text{BEAM}}$  angle. While the distribution of events does not have to be uniform itself, a  $180^\circ$  symmetry is expected. Beside the distribution of events other observables such as event energy should not have a dependence on the  $\phi_{\text{BEAM}}$ .

To study the uniformity in  $\phi_{\text{BEAM}}$  angle for the  $^{16}\text{O}(\gamma, \alpha)^{12}\text{C}$  two complementary selections were used:

- Selection to two subsamples “up/down”:
  1. Events with the  $\alpha$  track in a direction towards the readout plane ( $\phi_{\text{BEAM}} < 0$ , geographically up).
  2. Events with the  $\alpha$  track in a direction against the readout plane ( $\phi_{\text{BEAM}} > 0$ , geographically down).
- Selection to two subsamples “left/right”:
  1. Events with the  $\alpha$  track in a direction towards “detector right side” ( $-\frac{\pi}{2} < \phi_{\text{BEAM}} < \frac{\pi}{2}$ ).
  2. Events with the  $\alpha$  track in a direction towards “detector left side” ( $\phi_{\text{BEAM}} < -\frac{\pi}{2} \cup \frac{\pi}{2} < \phi_{\text{BEAM}}$ ).

The number of entries in each subsample was tested with a two-sided binomial test, with the null hypothesis that none of the directions is favored ( $p = 50\%$ ). In both cases, the null hypothesis was not rejected (test p-value = 7% for “up/down” subsamples and p-value = 21% for “left/right” subsamples) signifying that the probability of detection an event does not depend on the orientation in space.

In addition the consistency among each of these selections has been investigated with the 2-sample K-S test [43, 66] on:

- $\alpha$  kinetic energy distribution in CM (prior to unfolding Section 5.4.4),
- $\alpha$  track  $\theta_{\text{BEAM}}$  angular distribution in CM,

with the hypothesis that the distributions for both subsamples are the same and an alternative that they are not the same. Assuming the importance level of 5% it was not possible to reject the null hypothesis in case of  $\theta_{\text{BEAM}}$  angular distribution for “up/down” and “left/right” subsamples respectively, as well as rejecting the null hypothesis for  $\alpha$  kinetic energy distribution for “left/right” subsamples.



In case of  $\alpha$  kinetic energy distribution for “up/down” subsamples the null hypothesis had to be rejected in every run. Figure 5.23 presents example comparison of such a case. Another 2-sample K-S test has been done with the null hypothesis that the  $\alpha$  kinetic energy of “up” subsample is systematically shifted towards higher energies than the same distribution for “down” subsample. This time the null hypothesis could not be rejected with the significance level of 5% for any energy tested. These two tests show strong evidence against the uniformity and for energy-azimuthal angle dependence.

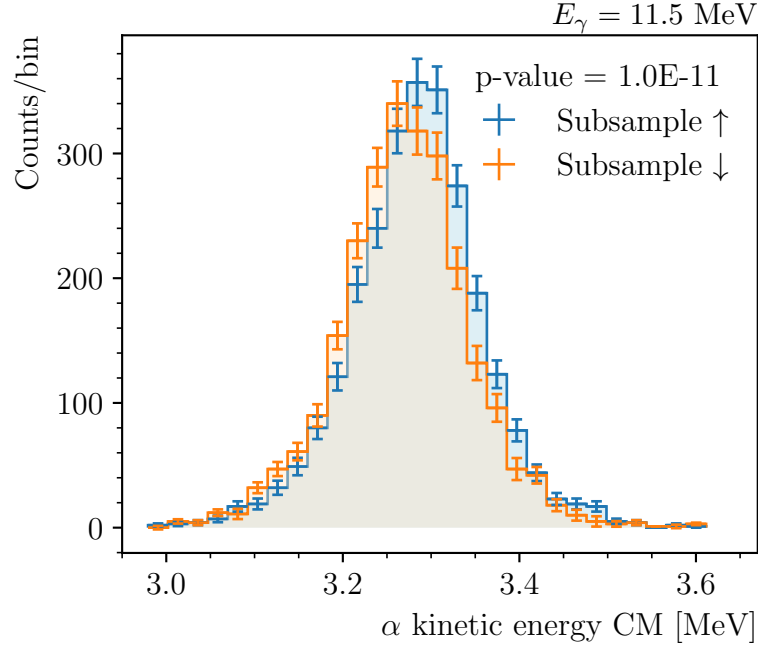


Figure 5.23: Comparison of  $\alpha$  kinetic energy for subsamples “up” and “down”. The consistency of subsamples has been examined with a 2-sample K-S test with a null hypothesis that both subsamples were drawn from the same distribution. A test p-value ( $1.0\text{E} - 11$ ) smaller than the significance level of 5%, shows a strong evidence against the uniformity hypothesis. Similar behavior was observed for other energies. The binned data is shown just as an illustration as the K-S test was done on unbinned data.

The apparent  $\alpha$  track  $\theta_{\text{BEAM}}$  vs energy dependence can be taken into account with the next iteration of establishing the energy calibration for the experiment. A finer dependence might be found with greater number of entries. The exact physical explanation for this dependence is yet to be studied. At the time of writing two physical effect are considered due to the difference of expected drift length of “up” and “down” subsamples:

1. Longer drift length results in higher charge diffusion.
2. Longer drift length results in higher charge losses.

## 5.6 Angular distributions

The angular distributions of the reaction products follow the angular dependence describing the differential cross-section.

The differential cross-sections of  $^{12}\text{C}(\alpha, \gamma)^{16}\text{O}$  and  $^{16}\text{O}(\gamma, \alpha)^{12}\text{C}$  are related by the same multiplicative factor as their total cross-section in Equation 1.7 with a minor nuisance coming from a the possible polarization discussed by Brune [67].

As shown by [67] the  $^{12}\text{C}(\alpha, \gamma)^{16}\text{O}$  reactions produces linearly polarized  $\gamma$ -ray. In case of the photodisintegration the polarization is described the fraction of linear polarization  $f$  polarization angle  $\phi_0$  and the photon wave number  $k_\gamma$  of the delivered  $\gamma$ -beam and affects the angular distribution of the reactions products:

$$\frac{d\sigma_{\gamma\alpha}(\theta, \phi)}{d\Omega} = \frac{1 + f \cos(2(\phi - \phi_0))}{16k_\gamma^2} \cdot \frac{d\sigma_{\gamma\alpha}(\theta)}{d\cos(\theta)} \quad (5.1)$$

Note the cross-sections disussed in this part of the work are already expressed in the CM and no further correction for center of mass energy is required [67].

### 5.6.1 Angular resolution

Unlike the energy resolutions the experimental data does not provide any additional means to asses the angular resolution beside the angular resolution estimated from the comparison of reconstructions done by different experts.

The angular resolution can be taken into account in two ways:

1. Unfolding. The distributions can be unfolded with the estimated resolution in order to retrieve unbranded experimental distributions that can be fitted directly. Usually the unfolding is performed on the binned data and the procedure is applicable only if the resolution is worse than the bin size.
2. Folding. The fitted distributions can be convolved and broadened by the estimated resolution or the resolution can be a free parameter. This approach requires either having a solid estimation or significant size of data to fit an additional parameters responsible for a small correction.

The application of any of these methods pose a problem as the angular resolution is estimated roughly as a single number and does not include dependencies on energy or angle. Due to limited sample size a reasonable binning of the sample (e.g. following Freedman-Diaconis or square-root rule) is slightly bigger (typical values 3-5°) than estimated value of 1°.

Taking into account the above reasons the current study proceeds without applying an angular resolution correction. A correction can be applied in further studies when a bigger number of entires is available and more precise estimation of the resolution is possible.

### 5.6.2 Azimuthal angle

The experimental azimuthal angle distribution in the BEAM coordinate system can be derived from the Equation 5.1:

$$W(\phi) = 1 + f \cdot \cos(2(\phi - \phi_0)) \quad (5.2)$$

The azimuthal angle distribution is related with the beam polarization expressed as a Stokes vector  $\mathbf{S}$  [68]:

$$\mathbf{S} = \begin{pmatrix} 1 \\ S_1 \\ S_2 \\ S_3 \end{pmatrix} \quad (5.3)$$

$$S_1 = \frac{W(0) - W(\pi/2)}{W(0) + W(\pi/2)} \quad (5.4)$$

$$S_2 = \frac{W(\pi/4) - W(-\pi/4)}{W(\pi/4) + W(-\pi/4)} \quad (5.5)$$

$$S_3 = \sqrt{1 - S_1^2 - S_2^2} \quad (5.6)$$

The relationship between the basis of the Stokes vectors  $\mathbf{S}$  and the polarization states is given in the Table 5.7. Through the equation it is possible to find the relative degrees of circular and liner polarizations of the beam. Note, it is not possible to deduce the degree of polarized to unpolarized just from this data.

Table 5.7: Common polarization states expressed as a Stokes vectors.

Polarization	$\mathbf{S}^\top$
Unpolarized	(1 0 0 0 )
Linear horizontal	(1 1 0 0 )
Linear vertical	(1 -1 0 0 )
Linear 45°	(1 0 1 0 )
Linear -45°	(1 0 -1 0 )
Circular right-handed	(1 0 0 1 )
Circular left-handed	(1 0 0 -1)

In order to make a fit to the experimental data using the Maximum Likelihood Estimation (MLE) one has to construct a probability distribution for the beam polarization. A Probability Density Function (PDF) of such distribution takes the following form:

$$W(\phi | f, \phi_0) = \frac{1}{2\pi} (1 + f \cdot \cos(2(\phi - \phi_0))) \quad f \in [0, 1], \phi_0 \in [0, \pi] \quad (5.7)$$

The Figure 5.24 presents the PDF and Cumulative Density Function (CDF) of the azimuthal angle probability distribution  $W(\phi | f, \phi_0)$  for an example set of parameters.

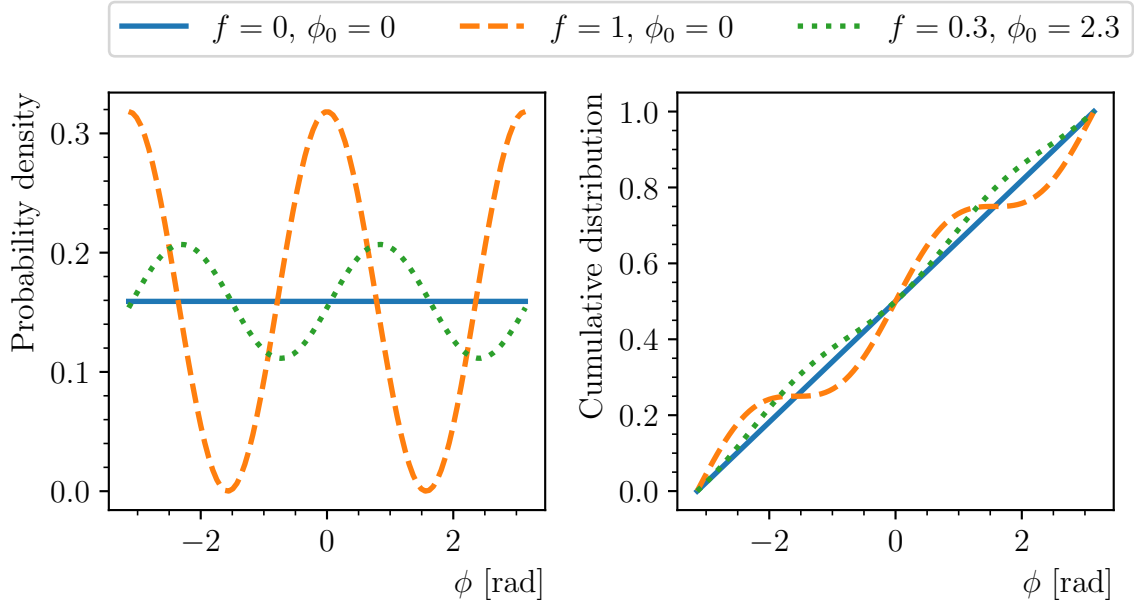


Figure 5.24: Probability distribution  $W(\phi | f, \phi_0)$  corresponding to the beam polarization. On the left PDF is shown, on the right CDF. Note the two edge cases: first  $f = 0$  for pure circular polarization for a beam, second  $f = 1$  for pure linear polarization of a beam. The  $\phi_0$  controls the axis of linear polarization.

The discussed distribution was fitted to each reconstructed experimental run. The results of the fits to selected  $^{16}\text{O}(\gamma, \alpha)^{12}\text{C}$  events are listed in Table 5.8, while the example fit plots are presented in the Figure 5.25.

All the runs collected during April campaign shown consistent circular polarization on the level of around  $S_3 = 0.93$ . In case of the runs collected in August/September experiment the circular polarization is again consistent but on the level of  $S_3 = 0.99$ . The levels of circular polarization with a small addition of linear polarization obtained through the fit are in good agreement with the beam diagnostics [69].

Table 5.8:  $\gamma$ -beam polarization parameters and resulting beam circular polarization obtained from a  $W(\phi | f, \phi_0)$  fit to selected  $^{16}\text{O}(\gamma, \alpha)^{12}\text{C}$  events. The degree of circular polarization  $S_3$  changed during the August campaign (runs  $E_\gamma = 9.85$  MeV and  $E_\gamma = 9.56$  MeV).

$E_\gamma$ (MeV)	$f$	$\phi_0$ (rad)	$S_3$
13.5	0.430(37)	2.332(47)	0.903(17)
13.1	0.362(25)	2.444(37)	0.9321(94)
12.3	0.345(27)	2.496(41)	0.9387(97)
11.9	0.362(19)	2.501(28)	0.9320(72)
11.5	0.318(21)	2.482(34)	0.9480(69)
9.85	0.096(58)	0.59(30)	0.9953(60)
9.56	0.118(58)	0.70(24)	0.9930(72)

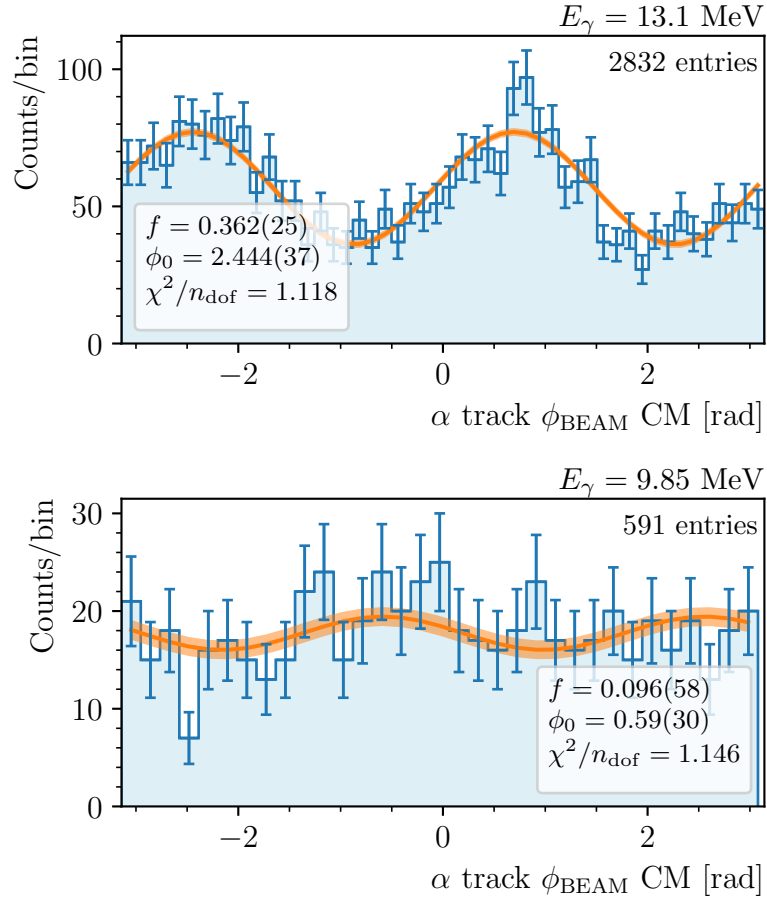


Figure 5.25: Beam polarization fit  $W(\phi | f, \phi_0)$  to the experimental data. Top: fit to an example run from April campaign. Bottom: fit to an example run from August campaign. Note the change of  $f$  parameter responsible for degree of linear polarization.  $\pm 1\sigma$  fit error bands are displayed.

### 5.6.3 Polar angle

The polar angle dependence of the  $^{16}\text{O}(\gamma, \alpha)^{12}\text{C}$  reaction is given by [5]<sup>1</sup> :

$$\frac{d\sigma(\cos(\theta))}{d\cos(\theta)} = \frac{\sigma_{E1}}{2} W_{E1}(\cos(\theta)) + \frac{\sigma_{E2}}{2} W_{E2}(\cos(\theta)) + \frac{\sqrt{\sigma_{E1}\sigma_{E2}}}{2} \cos(\phi_{12}) W_{12}(\cos(\theta)) \quad (5.8)$$

The Equation 5.8 consists of three terms: first describing the E1 multipolarity, second describing the E2 multipolarity and third being the effect of interference between E1 and E2 and control by the so-called E1–E2 mixing phase angle  $\phi_{12}$ . The terms can be expressed with following formulas:

$$W_{E1}(\cos(\theta)) = P_0(\cos(\theta)) - P_2(\cos(\theta)) \quad (5.9)$$

$$W_{E2}(\cos(\theta)) = P_0(\cos(\theta)) + \frac{5}{7}P_2(\cos(\theta)) - \frac{12}{7}P_4(\cos(\theta)) \quad (5.10)$$

$$W_{12}(\cos(\theta)) = \frac{6}{\sqrt{5}} (P_1(\cos(\theta)) - P_3(\cos(\theta))) \quad (5.11)$$

where the  $P_l(\cos(\theta))$  are Legendre polynomials. For convenience the standard representation of the polynomials are listed in Table 5.9. Note that both  $W_{E1}$  and  $W_{E2}$  are symmetric, while  $W_{12}$  is antisymmetric.

Table 5.9: Legendre polynomials in standard representation.

$l$	$P_l(\cos(\theta))$
0	1
1	$\cos(\theta)$
2	$\frac{1}{2}(3\cos^2(\theta) - 1)$
3	$\frac{1}{2}(5\cos^3(\theta) - 3\cos(\theta))$
4	$\frac{1}{8}(35\cos^4(\theta) - 30\cos^2(\theta) + 3)$

In order to fit the angular distributions using the maximum likelihood estimation method one can construct a corresponding probability distribution with the PDF:

$$W\left(\cos(\theta) \mid \frac{\sigma_{E1}}{\sigma_{E2}}, \phi_{12}\right) = \frac{\frac{\sigma_{E1}}{\sigma_{E2}} \cdot W_{E1}(\cos(\theta)) + W_{E2}(\cos(\theta)) + \sqrt{\frac{\sigma_{E1}}{\sigma_{E2}}} \cdot \cos(\phi_{12}) \cdot W_{12}(\cos(\theta))}{2\left(1 + \frac{\sigma_{E1}}{\sigma_{E2}}\right)} \quad (5.12)$$

The relative contributions of the E1 and E2 can be parametrized also as a fraction of a total cross-section:

$$\frac{\sigma_{E1}}{\sigma_{\text{tot}}} = \frac{\frac{\sigma_{E1}}{\sigma_{E2}}}{1 + \frac{\sigma_{E1}}{\sigma_{E2}}} \quad \frac{\sigma_{E2}}{\sigma_{\text{tot}}} = \frac{1}{1 + \frac{\sigma_{E1}}{\sigma_{E2}}} \quad (5.13)$$

<sup>1</sup>Note a slight difference with respect to the equation used by [5] as the attenuation factors  $Q_l$  are missing. Such factor are relevant for measurements with detectors with limited solid angle such as arrays of HPGe. In case of an active-target TPC with  $4\pi$  solid angle the attenuation is not required.

A plot of the  $W\left(\cos(\theta) \mid \frac{\sigma_{\text{E1}}}{\sigma_{\text{E2}}}, \phi_{12}\right)$  distribution is given in the Figure 5.26. The parameter  $\frac{\sigma_{\text{E1}}}{\sigma_{\text{E2}}}$  controls the ratio of E1 and E2 components. The distribution has two notable limits corresponding to pure E1 or E2 with no dependence on the E1–E2 mixing phase angle  $\phi_{12}$  parameter:

$$\lim_{\frac{\sigma_{\text{E1}}}{\sigma_{\text{E2}}} \rightarrow \infty} W\left(\cos(\theta) \mid \frac{\sigma_{\text{E1}}}{\sigma_{\text{E2}}}, \phi_{12}\right) = 0.5 \cdot W_{\text{E1}}(\cos(\theta)) \quad (5.14)$$

$$\lim_{\frac{\sigma_{\text{E1}}}{\sigma_{\text{E2}}} \rightarrow 0} W\left(\cos(\theta) \mid \frac{\sigma_{\text{E1}}}{\sigma_{\text{E2}}}, \phi_{12}\right) = 0.5 \cdot W_{\text{E2}}(\cos(\theta)) \quad (5.15)$$

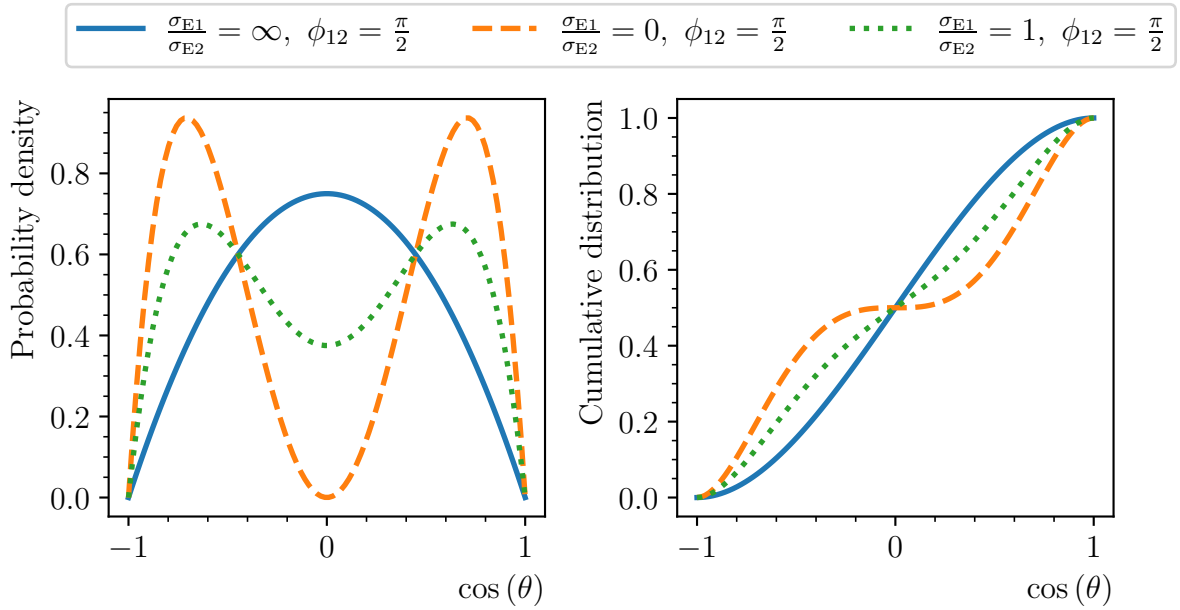


Figure 5.26: Probability distribution  $W\left(\cos(\theta) \mid \frac{\sigma_{\text{E1}}}{\sigma_{\text{E2}}}, \phi_{12}\right)$  corresponding to the angular distribution. On the left PDF, on the right CDF. Note the two edge cases: 1.  $\frac{\sigma_{\text{E1}}}{\sigma_{\text{E2}}} \rightarrow \infty$  when only the E1 component is present, 2.  $\frac{\sigma_{\text{E1}}}{\sigma_{\text{E2}}} \rightarrow 0$  when only the E2 component is present.

The E1–E2 phase mixing angle  $\phi_{12}$  can be related to the elastic scattering  $^{12}\text{C}(\alpha, \alpha')$  phase shifts for  $l = 1$  ( $\delta_1$ ) and  $l = 2$  ( $\delta_2$ ) [67]:

$$\phi_{12} = \delta_2 - \delta_1 + \arctan \eta \quad (5.16)$$

where  $\eta$  is the Sommerfeld parameter. The scattering angles were established by Plaga [70] and are widely accepted by the community. A number of studies followed this path to use the theoretical prediction and reduce the number of free parameters to be found. As discussed by Gai [71] in some case a difference between the prediction and the experimental values were observed and the general validity of this approach was put in question. In order to provide more material to investigate this aspect the  $\phi_{12}$  was kept as a fit's free parameter.

The  $W\left(\cos(\theta) \mid \frac{\sigma_{\text{E1}}}{\sigma_{\text{E2}}}, \phi_{12}\right)$  was fitted to the experimental data selected for  $^{16}\text{O}(\gamma, \alpha)^{12}\text{C}$  reaction. An example fit results are presented in the Figure 5.27.

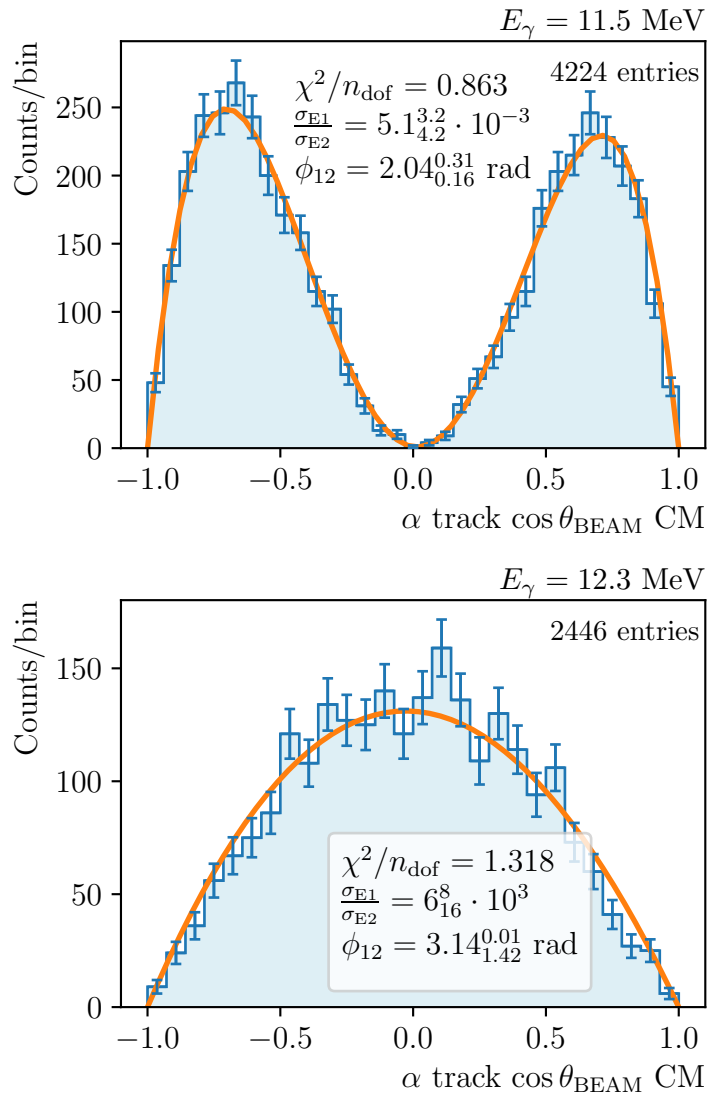


Figure 5.27: Fitted polar angle distributions. A MLE fit of  $W(\cos(\theta) | \frac{\sigma_{\text{E1}}}{\sigma_{\text{E2}}}, \phi_{12})$  was done the experimental data selected for  $^{16}\text{O}(\gamma, \alpha)^{12}\text{C}$  reaction in order to estimate the ratio of E1 cross-section to E2 cross-section  $\frac{\sigma_{\text{E1}}}{\sigma_{\text{E2}}}$  and E1–E2 phase mixing angle  $\phi_{12}$ . No energy selection was applied. Top: an E2 transition dominated sample is fitted. Bottom: an E1 dominated samples is fitted. Note the large uncertainties even though the reduced  $\chi^2$  value and visual inspection suggest the fit was successful.

In most of the experimental runs the measured energy distribution follows a bell-shaped curve. An additional selection by energy into too many energy regions would drastically decrease the already limited number of entries, especially on the energy distribution tails. A notable exception is the  $E_\gamma = 11.9$  MeV where a very broad continuous energy distribution is observed and energy selection can be used to obtain finer graining and investigate the evolution of E1 to E2 ratio in the region.



Taking into account that the  $\gamma$ -beam used in the experiment was not monoenergetic, the obtained values of the fit  $x$  corresponds to the physical values averaged over the reaction induced from a broad  $\gamma$ -beam energy spectrum:

$$x^{\text{eff}} = \frac{\int_0^\infty dE x(E) \sigma(E) P(E)}{\int_0^\infty dE \sigma(E) P(E)} \quad (5.17)$$

where  $P(E)$  is the probability distribution describing the  $\gamma$ -beam energy spectrum and  $\sigma$  is the cross-section of the reaction. As discussed in Section 4.4.2 the obtained energy resolution is much better than the resolution of the  $\gamma$ -beam and allows for energy selection on the measured data. In that case the values are averaged a smaller energy region:

$$x^{\text{eff}} = \frac{\int_{E_0}^{E_1} dE x(E) \sigma(E) P(E)}{\int_{E_0}^{E_1} dE \sigma(E) P(E)} \quad (5.18)$$

where  $E_1$  and  $E_0$  are the bounds of applied energy selection. The range of selected region is limited by number of entries required to make a fit. Often in order to place the effective values obtained by these procedures on the energy scale, an effective energy is used, being similarly the average energy over observed with the  $\gamma$ -beam spectrum:

$$E^{\text{eff}} = \frac{\int_{E_0}^{E_1} dE E \sigma(E) P(E)}{\int_{E_0}^{E_1} dE \sigma(E) P(E)} \quad (5.19)$$

The results of the fit illustrating the evolution of the E1/E2 ratio with the energy is presented in the Figure 5.28. The obtained parameters are listed along their effective energy in the Table 5.10.

Table 5.10: Obtained  $^{16}\text{O}(\gamma, \alpha)^{12}\text{C}$  cross-section ratios and E1–E2 mixing phase angle of  $^{16}\text{O}(\gamma, \alpha)^{12}\text{C}$  reaction. The effective center of mass energy  $E_{\text{CM}}^{\text{eff}}$  of every point, ratio of E1 and E2 component cross-sections  $\frac{\sigma_{\text{E1}}}{\sigma_{\text{tot}}}$ , fraction of E1 to sum of E1 and E2 cross-sections are given. The fraction of E1 cross-section to the total cross-section is given. The run identifier by nominal beam energy  $E_\gamma$  and energy selection are listed.

$E_{\text{CM}}^{\text{eff}}$ (MeV)	$\frac{\sigma_{\text{E1}}}{\sigma_{\text{E2}}}$	$\frac{\sigma_{\text{E1}}}{\sigma_{\text{tot}}}$	$\phi_{12}$ (rad)	$E_\gamma$ (MeV)	Selection (MeV)
2.38(10)	$45_{21}^{19}$	$0.9783_{0.0098}^{0.0090}$	$0.01_{0.01}^{0.60}$	9.56	$2.00 < E_{\text{CM}} < 2.55$
2.678(57)	$0.175_{0.044}^{0.041}$	$0.149_{0.032}^{0.030}$	$1.486_{0.074}^{0.073}$	9.85	$2.55 < E_{\text{CM}} < 2.80$
4.238(57)	$0.0142_{0.0076}^{0.0063}$	$0.0140_{0.0074}^{0.0061}$	$2.13_{0.14}^{0.20}$	11.5	$3.90 < E_{\text{CM}} < 4.30$
4.375(40)	$0.0099_{0.0062}^{0.0046}$	$0.0098_{0.0060}^{0.0045}$	$1.95_{0.11}^{0.17}$	11.5	$4.30 < E_{\text{CM}} < 4.45$
4.448(29)	$0.0067_{0.0068}^{0.0046}$	$0.0066_{0.0067}^{0.0045}$	$1.43_{0.20}^{0.15}$	11.9	$4.40 < E_{\text{CM}} < 4.50$
4.583(59)	$0.086_{0.023}^{0.021}$	$0.080_{0.020}^{0.018}$	$1.461_{0.068}^{0.067}$	11.9	$4.50 < E_{\text{CM}} < 4.70$
4.805(57)	$1.26_{0.23}^{0.24}$	$0.558_{0.045}^{0.046}$	$1.541_{0.051}^{0.051}$	11.9	$4.70 < E_{\text{CM}} < 4.90$
5.249(70)	$85_{105}^{489}$	$0.9884_{0.0141}^{0.0659}$	$1.4_{1.4}^{0.1}$	12.3	$5.10 < E_{\text{CM}} < 5.40$
5.904(91)	$18.8_{5.6}^{7.5}$	$0.949_{0.014}^{0.019}$	$0.91_{0.16}^{0.09}$	13.1	$5.70 < E_{\text{CM}} < 6.10$
5.996(54)	$9.7_{4.0}^{5.9}$	$0.906_{0.035}^{0.052}$	$1.15_{0.14}^{0.09}$	13.5	$5.90 < E_{\text{CM}} < 6.10$

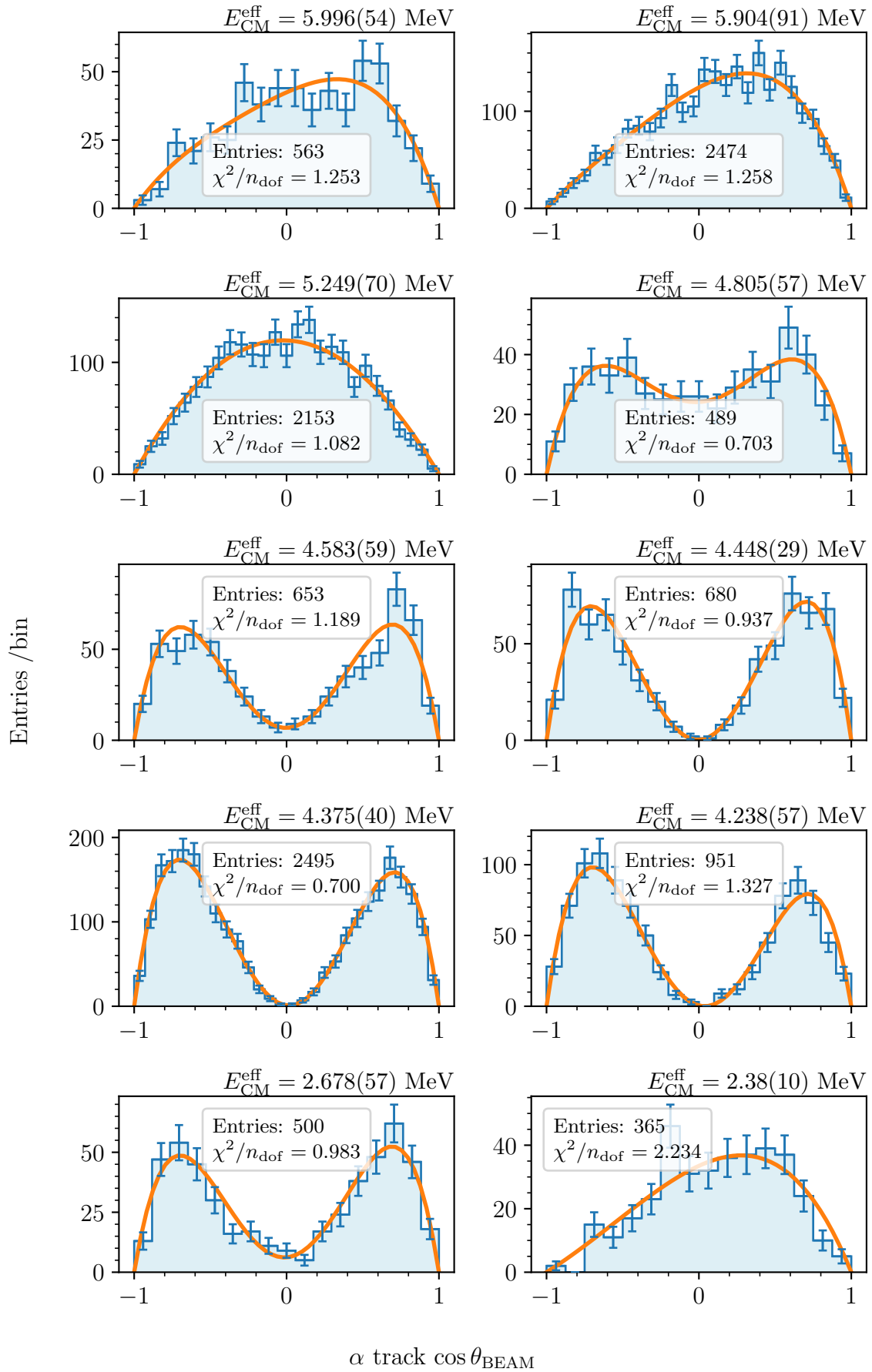


Figure 5.28: Polar angle distribution  $W(\cos(\theta) | \frac{\sigma_{E1}}{\sigma_{E2}}, \phi_{12})$  fitted to energy selected data.

### 5.6.4 Confidence regions

In multiple cases the obtained parameters were characterized by significant uncertainties. The confidence intervals can be investigated in order to identify possible problems. A plot of confidence intervals for energy point with regular uncertainties and another with abnormally large uncertainties is given in the Figure 5.29.

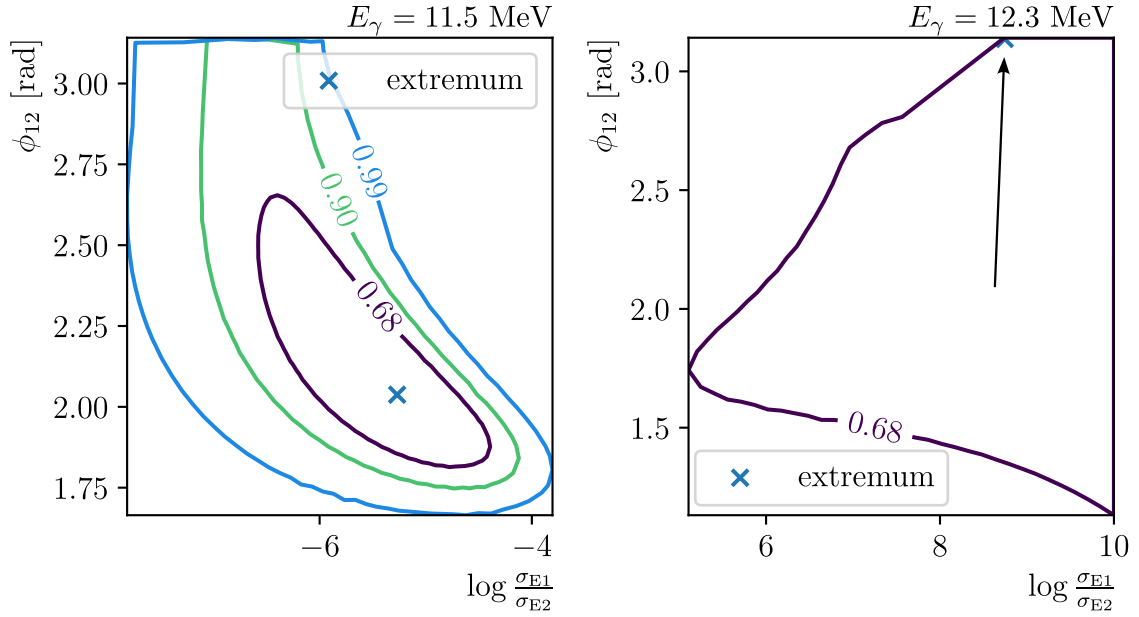


Figure 5.29: Example confidence regions for polar angle distribution MLE. The confidence regions were calculated with the likelihood ratio method for fits presented in the Figure 5.27. Left: regular confidence region shape. The estimated uncertainties from the fit could be to some degree approximated with a multivariate normal distribution and covariance matrix. The obtained uncertainties values are reasonably small. Right: peculiar confidence region shape. The uncertainties cannot be effectively described by a multivariate normal distribution and covariance matrix. The resulting values of uncertainties are significant as they poorly approximate the region.

In case of fit with large uncertainties a peculiar, highly correlated dependence between  $\frac{\sigma_{E1}}{\sigma_{E2}}$  and  $\phi_{12}$  is discovered. The shape of the confidence intervals strongly suggested the use of non-symmetric uncertainties. Another observation is that the large uncertainties are obtained predominantly for cases when E1 component is dominating.

### 5.6.5 Power analysis

Basing on the poor fit performance in cases of E1 dominated samples the limited number of entries available is a concern. In general the effects of sample size on a statistics can be addressed by a power analysis [43].

For instance in the light of an observation that the polar angle probability distribution  $W(\cos(\theta) | \frac{\sigma_{E1}}{\sigma_{E2}}, \phi_{12})$  has two limits that are independent on the second  $\phi_{12}$  parameter, one can investigate a problem of statistically distinguishing a distribution with given parameters from a limiting distribution.

Such study can be done by the use of a Likelihood Ratio Test (LRT) <sup>2</sup> [43]. In case of E1 dominated samples a test with with following hypotheses is considered:

$$H_0 : \frac{\sigma_{E1}}{\sigma_{E2}}, \phi_{12} = 0 \quad (5.20)$$

$$H_1 : \frac{\sigma_{E1}}{\sigma_{E2}} = +\infty, \phi_{12} = 0 \quad (5.21)$$

A similar test can be constructed for the case when the E2 component is dominating:

$$H_0 : \frac{\sigma_{E1}}{\sigma_{E2}}, \phi_{12} = 0 \quad (5.22)$$

$$H_1 : \frac{\sigma_{E1}}{\sigma_{E2}} = 0, \phi_{12} = 0 \quad (5.23)$$

A power analysis of the tests can be done in order to find the minimal number of entries required to achieve desired test power when differentiating between a fit parameters and limiting distribution or to find the range of parameters on which the tests achieves required power given the number of entries. An example test power analysis for the described tests is depicted in the Figure 5.30.

The tests' power is different for pure E1 and E2 alternatives with the test with pure E2 alternative achieving significantly bigger power. This result is compatible with the results of the fits when E2 dominated samples in general achieved better values of goodness-of-fit (GoF) statistics. A general conclusion that for  $\frac{\sigma_{E1}}{\sigma_{E2}}$  in range of 10-100 a sample size of order 10000 is needed or of order 100000 in cases of 100-1000 range. The sizes of samples used in the current studies are an order of magnitude smaller. The given values are just an estimates as the simple tests did not include the E1-E2 mixing phase angle  $\phi_{12}$  effect on the shape of the distribution.

Similar tests may be constructed without fixing the  $\phi_{12}$  or for testing in a vicinity of regions than the limiting distributions. For instance a vicinity of the parameters  $\frac{\widehat{\sigma_{E1}}}{\widehat{\sigma_{E2}}}, \widehat{\phi_{12}}$  obtained in a MLE may be scanned and tested with following hypotheses<sup>3</sup>:

$$H_0 : \frac{\sigma_{E1}}{\sigma_{E2}}, \phi_{12} \quad (5.24)$$

$$H_1 : \frac{\widehat{\sigma_{E1}}}{\widehat{\sigma_{E2}}}, \widehat{\phi_{12}} \quad (5.25)$$

<sup>2</sup>A LRT with simple hypothesis is also known as a Neyman-Pearson test.

<sup>3</sup>A LRT with compound hypotheses when one of them is a MLE estimate is also known as a Wilks test.

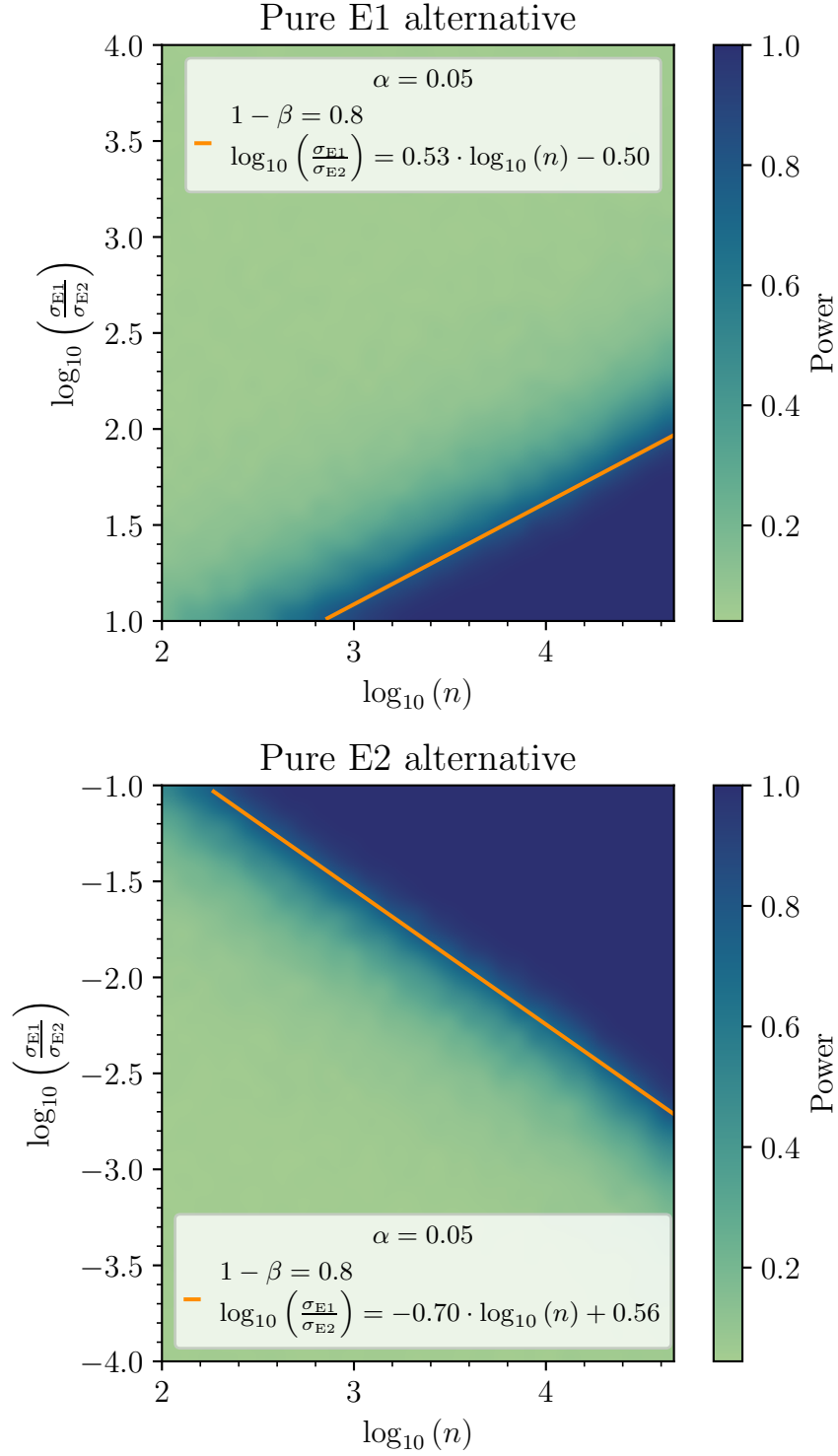


Figure 5.30: Power of a test against pure E1 and pure E2 alternatives for significance level  $\alpha = 5\%$  as a function on cross-section ratio  $\left(\frac{\sigma_{\text{E1}}}{\sigma_{\text{E2}}}\right)$  and sample size  $(n)$ . The lines mark the region when the power  $1 - \beta$  is equal 80%.



# Chapter 6

## Results

The results of the analysis in a form of the  $^{16}\text{O}(\gamma, \alpha)^{12}\text{C}$  reaction cross-sections for E1 and E2 transitions respectively, total cross-sections including the E1–E2 phase mixing angle  $\phi_{12}$  are meant to after further refinement and verification enrich the experimental knowledge on the highly important  $^{12}\text{C}(\alpha, \gamma)^{16}\text{O}$  reaction — similarly to studies [6–9] — that is much needed in order to improve the theoretical R-matrix fits [1].

### 6.1 Relative cross-section

While calculating the absolute  $\gamma$ -beam and obtaining the absolute cross-sections was outside of the scope of this work, the available relative cross-section can still be compared with the theoretical values.

Given the multiple possible ways of presenting similar information such as S-factors vs cross-sections or cross-sections of direct reaction vs photodisintegration, the choice was made to stay with the representation natural to the WARSAW TPC— the cross-sections of  $^{16}\text{O}(\gamma, \alpha)^{12}\text{C}$ . The choice was dictated by the novelty of the study and possible existence of detector effects that could be less visible with different representation. Having said that, the recalculation to the S-factor of  $^{12}\text{C}(\alpha, \gamma)^{16}\text{O}$  reaction that is more frequently used in the literature is possible.

### 6.1.1 Total cross-section

An experimental total relative cross-section (including both E1 and E2 transitions) of the  $^{16}\text{O}(\gamma, \alpha)^{12}\text{C}$  reaction was obtained by the division of the measured energy reconstruction by fitted  $\gamma$ -beam energy spectra (see Figure 5.22). Without an absolute  $\gamma$ -beam intensity a cross-section obtained this way is known with the respect to a multiplicative factor. For every experimental this normalization factor is expected to have a different values, while the energy points of the same run should follow the same factor with a possible correction for efficiency. Due to this a shape of the relative total cross-section can be qualitatively compared with a theoretical prediction.

The Figure 6.1 presents a comparison of relative total cross-section with a cross-section calculated basing on the R-matrix fit by deBoer [1]. No major contradictions were observed. The deviance from the R-matrix fit can might result from underestimation of the detector resolution or shortcomings of the deconvolution method. Another possibility is the discrepancy between the  $\gamma$ -beam energy spectrum delivered during the run and a spectrum measured during the calibration run.

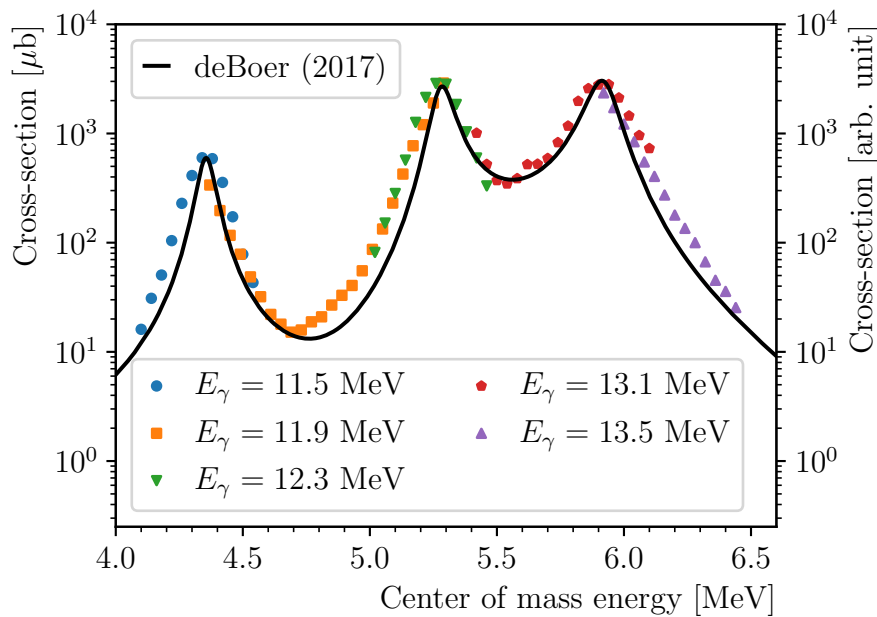


Figure 6.1: Relative total  $^{16}\text{O}(\gamma, \alpha)^{12}\text{C}$  cross-section qualitatively compared with deBoer's R-matrix fit [1]. Each group of energy points was scaled to align with the theoretical values. The deviance from the deBoer's R-matrix fit might be explained by underestimation of the detector resolution or discrepancy between deconvolved HPGe  $\gamma$ -spectrum and real spectrum delivered during the experimental run.



### 6.1.2 E1 and E2 cross-section fractions

Another possible presentation of the results is the fraction of cross-section for  $^{16}\text{O}(\gamma, \alpha)^{12}\text{C}$  E1 transition against the total cross-section including both E1 and E2 transitions. This presentation does not require any scaling in order to be compared with the theoretical values. The comparison of obtained E1 cross-section fraction (values from Table 5.10) with deBoer's R-matrix fit [1] is presented in the Figure 6.2. No major discrepancies are observed.

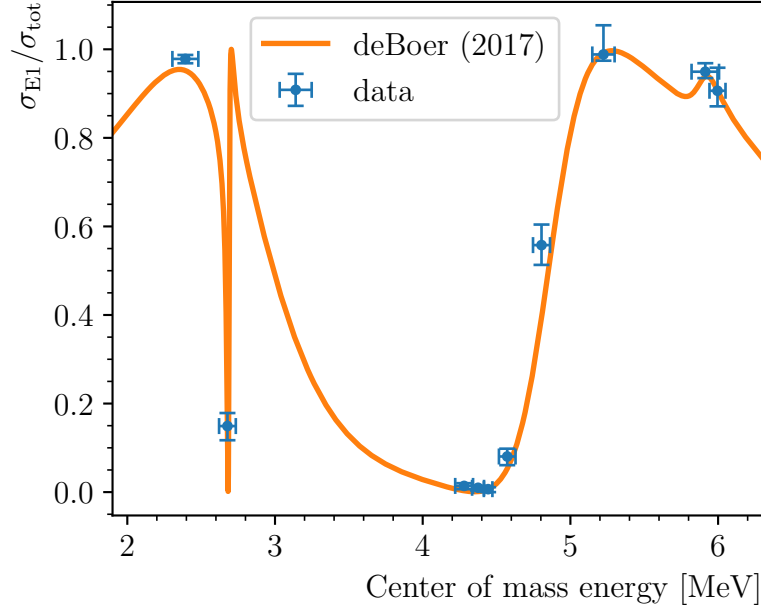


Figure 6.2:  $^{16}\text{O}(\gamma, \alpha)^{12}\text{C}$  cross-section of E1 component to the cross-section of sum of E1 and E2 components. The experimental data is compared with R-matrix fit [1].

## 6.2 E1–E2 mixing phase angle evolution

The validity of E1–E2 mixing phase angle  $\phi_{12}$  obtained from the experimental can be examine against the Equation 5.16 in order to address the concerns about the validity of the the relation [71]. The Figure 6.3 presents the comparison of obtained  $\phi_{12}$  and theoretical predictions [70, 72]. No significant deviations from the theoretical predictions were observed with the present uncertainties.

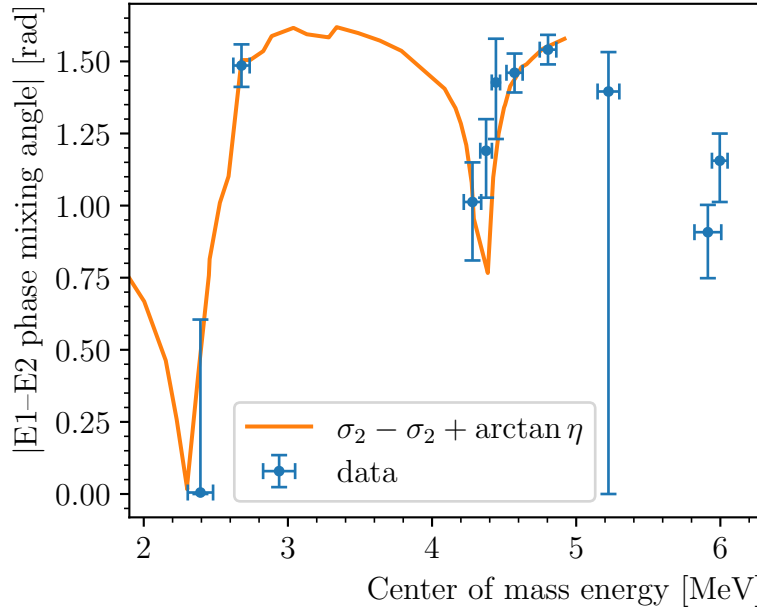


Figure 6.3: E1–E2 mixing phase angle  $\phi_{12}$  evolution. Theoretical prediction  $\delta_2 - \delta_1 + \arctan \eta$  based on elastic scattering [70, 72]. The E1–E2 mixing phase angle  $\phi_{12}$  range was normalized to  $(0, \frac{\pi}{2})$  rad.

The obtained E1–E2 mixing phase angles  $\phi_{12}$  don't require any further calibration with absolute  $\gamma$ -beam intensity like the other values, and are a valuable result on they own. For completeness the study can be repeated with  $\phi_{12}$  fixed on the theoretical values and compared with the present study with  $\phi_{12}$  as a free parameter. The fixing of values may improve the GoF for the cases when the large uncertainties due to the angular distribution approaching the limiting distribution.

### 6.3 $\gamma$ -beam energy–spatial position dependence

An unexpected non-symmetric dependence of  $\gamma$ -beam energy and spatial beam position has been observed. The dependence is presented in the Figure 6.4, where a two resonances of different energies are also separated in spatial position of the event vertex in a direction transverse to the  $\gamma$ -beam axis. Due to the shape of the cross-section only one experimental point ( $E_\gamma = 11.9$  MeV) happened in a large valley between two resonances where such dependence could be observed.

The observation was a novelty to the HI $\gamma$ S  $\gamma$ -beam operators [69] and to the knowledge no previous experiment at HI $\gamma$ S was sensitive to this effect or reported it. A dedicated experiment to thoroughly study the effect is being organized in late 2023. The result if confirmed might be applied to improve capabilities of the collimation system. The observed dependence does not affect the quality of other results.

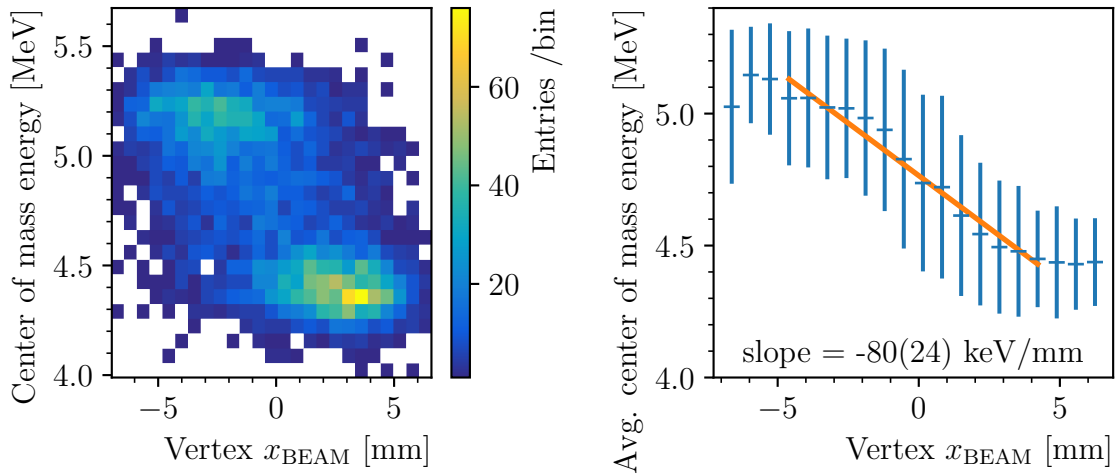


Figure 6.4: Reconstructed  $\gamma$  energy position dependence. A total difference of 716(88) keV in center of mass energy  $E_{\text{CM}}$  is observed over the entire beam width. Left: a two-dimensional histogram of event vertex  $x_{\text{BEAM}}$  (direction transverse to the beam axis) and center of mass energy  $E_{\text{CM}}$ . Right: profile plot showing the average  $E_{\text{CM}}$  vs vertex  $x_{\text{BEAM}}$  dependence.

### 6.4 Detector capabilities

The ability to obtain even with limited size of the experimental dataset, a meaningful physical results that are compatible with current knowledge is a main proof of the capabilities of the WARSAW TPC — both as a detector and together with accompanying data processing and analysis techniques — as a tool for studying nuclear reactions included with high intensity  $\gamma$ -beams. This result is very important to the WARSAW TPC collaboration given the novelty of the detector.



# Chapter 7

## Outlook

*Many people have suggested that a modern digital computer should be able to recognize a fairly complex pattern of tracks in a bubble chamber photograph.*

— P. V. C. Hough, 1959

While even with the limited number of events used in the current study it was possible to assess the WARSAW TPC as a detector for studying photonuclear reactions and moreover obtain results of physical importance it is worth noting the manually reconstructed data presents only a fraction of total number of events collected during the experiment at HI $\gamma$ S. It is expected the quality and precision of determination of cross-section ratios would greatly benefit from the increase of the dataset:

- the large statistical uncertainties of E1 and E2 cross-sections ratio and fractions due to insufficient number of entries has been a limiting factor for energies dominated by the E1 component,
- higher number of entries would allow for finer subsamples selection by energy and thus lower the energy uncertainties.

The estimation of total collected number of events based on the data reconstructed so far is presented in Table 7.1. Given the large size of the remaining unreconstructed dataset the manual reconstruction method seems to be unfeasible and other procedures should be pursued.

Table 7.1: Estimated available number of events collected during the WARSAW TPC experiment at HI $\gamma$ S in 2023. The manually reconstructed data was used to estimate the relative reaction trigger rate and fiducial cuts efficiency. Other runs measured during the experiment with nominal  $\gamma$ -beam energies different than the energies of recons are not presented. The estimated values listed are after fiducial cuts and present the number that would be available for the analysis.

$E_\gamma$ (MeV)	estimated total 2-prong events	number of available 3-prong events	% of data manually reconstructed
13.9	45000	10000	3.0
13.5	71000	2700	2.8
13.1	130000	1100	3.3
12.3	174000	1400	1.9
11.9	70000	2700	9.1
11.5	145000	2000	3.5
9.85	1300	1200	89.6
9.56	3000	2100	46.9
8.66	1600	300	55.9

## 7.1 Machine event reconstruction

Having identified the need to proceed with reconstructing all the collected experimental data, a two general approaches for machine reconstruction are proposed.

### 7.1.1 Classical event reconstruction

The so called classical event reconstruction is based on traditional image recognition techniques and statistical fits. The classical algorithm consists usually of the following steps:

1. Initial line detection with Hough transformation [42, 73] or RANSAC [74] algorithms. The general topology of event is determined at this point. Events can be selected for further reconstruction using criteria such as number of tracks.
2. Bragg curve model fits of all considered physical reactions. Either the lines found during the first step are used as the initial point of the fit or full Monte Carlo fit is employed.
3. Event classification based on GoF criteria (such as  $\chi^2$  statistics).

The initial work on the classical event reconstruction for the WARSAW TPC data based on the algorithm used by the Icarus experiment [25] was started [20, 75, 76] but the progress halted due to the lack of simulation framework needed in order to measure the quality of reconstruction and identify the weak points. With the recent addition of the simulations the works are expected to reassume.

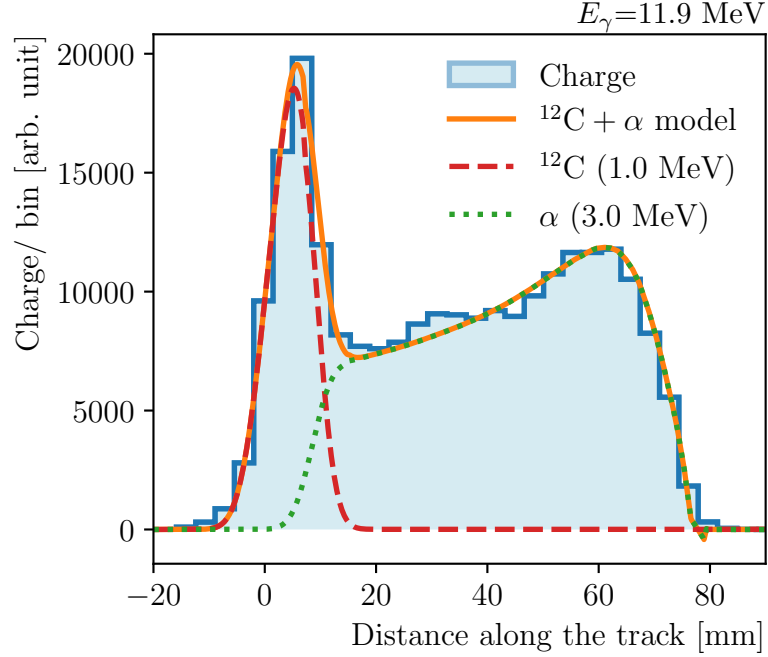


Figure 7.1: Classic machine event reconstruction for WARSAW TPC. The algorithm is using a Hough transform to identify lines followed up by a Bragg-curve fit. The algorithm is still under development as a simulation framework required to benchmark it was added only recently (May 2023).

### 7.1.2 Machine learning based event reconstruction

The utilization of Machine Learning (ML) based event classification or reconstruction has been already proven by a number of nuclear or HEP experiments. Even in the domain of TPCs the ML techniques were proven very successful [77–79]. A recent and very prominent example of Huangkai Wu *et al.* [80] presents the development of ML models and procedures for studying the  $^{12}\text{C}(\gamma, 3\alpha)$  with the future detector fMata-TPC. The same reaction was measured as a background during the WARSAW TPC experiment at HI $\gamma$ S.

Given that the WARSAW TPC is already represented as a tensor with an interpretation as a set of 3 two-dimensional projections, the use of Convolutional Neural Network (CNN) known for their outstanding renown for working with images is anticipated. To take advantage of the already developed CNN models the TPC data can be expressed as an image with the usual channels expressing RGB mapped to UVW projections. While the mentioned procedures enable using the TPC with already pre-trained models, a certain limitation is that the channels are not aligned and certain operations on the channels dimension (such as choosing the channel with highest values for a given pixel in image) have no clear interpretation.

Similarly to the development of the classical algorithms for the WARSAW TPC the main obstacle was lack of simulation framework. In case of supervised ML large datasets of labeled data are required for training of the model. Such datasets are usually created in realistic Monte Carlo simulations. Another possibility is the utilization of a

dataset created by experts, although a ML model trained from such dataset is prone to inherit the quality and possible shortcomings of a human expert. Another technical obstacle is that the framework developed for working with the WARSAW TPC data Appendix D (due to its legacy aspects) did not anticipate the need of highly performant data accesses and exports needed to prepare datasets required for ML models training and evaluation.

The prospects of employing ML based reconstruction for WARSAW TPC data has been studied by Robin Smith, Kristian C. Z. Haverson, Alex Shenfield, Sheffield Hallam University [35, 81]. The Figure 7.2 presents a confusion matrix[44] of one of the machine learning classification models trained on the manually reconstructed data. The confusion matrix depicts the fractions of a given class that the model predicted to be represents of other classes.

Confussion matrix

True label	1 prong	97%	0%	3.1%
	2 prong	1.9%	92%	5.7%
	3 prong	0%	5%	95%
		1 prong	2 prong	3 prong
		Predicted label		

Figure 7.2: Confusion matrix of a event classification model trained on manually reconstructed events. The model is using an ResNet-50 [82] convolutional neural network architecture. The confusion matrix presents estimated probability of predicting a chosen class (label) given the true class (label) of the input data. Figure taken from [81].

It is also worth mentioning that the event reconstruction is not the only field in the WARSAW TPC project that could benefit from the use of the ML techniques Other possible applications include problems such as fast simulation framework alternative as an alternative to the naïve toy-simulation models, waveform de-noising including electronic cross-talks between channels, realistic noise models.



## 7.2 Absolute cross-sections

While the scope of this thesis was limited to providing the initial look at the relative cross-section of the  $^{16}\text{O}(\gamma, \alpha)^{12}\text{C}$  E1 and E2 components, the experiment has been planned to allow monitoring  $\gamma$ -beam rate and calibrate it to absolute beam intensity and thus calculating the absolute cross-sections of both E1 and E2 components will be possible.

Calculating the required beam-intensities, elapsed-times and calibrating the auxiliary detectors is independent task from the development of machine reconstructions and can be accomplished in parallel.

As mentioned in Section 3.2 in part of the experimental runs a  $^{16}\text{O}(\gamma, p)^{15}\text{N}$  reaction with known cross-section [36] was measured. After a dedicated study this reaction can be used as an independent source of calibration for other reactions' rates. The study will required repeating the reconstruction as the offline trigger was set to treat the  $^{16}\text{O}(\gamma, p)^{15}\text{N}$  reaction as a background.

## 7.3 Continuation of the experiments

As the measurement conducted in a scope of April and August experimental campaigns were successful, the proof-of-principle of WARSAW TPC for the study of photo-disintegration reactions was accomplished.

With the event analysis principles in place and the upcoming progress in the event reconstruction the main obstacle remaining is the intensity of the available  $\gamma$ -beam. This problem becomes even more apparent for the lower-energies as the  $^{16}\text{O}(\gamma, \alpha)^{12}\text{C}$  cross-section decrease rapidly severely limiting the number of entries that can be collected.

A letter of intend was submitted requesting a continuation of the WARSAW TPC experiments at HI $\gamma$ S in a lower  $\gamma$ -beam energy region of 8.66 and 8.46 MeV. The problem of decreasing cross-section is planned to be addressed by requesting higher  $\gamma$ -beam intensities and with longer  $\gamma$ -beam exposure times. Such brute-forcing the experiments can't continue indefinitely as the monetary costs of every new experimental point in lower energies direction will increase.

In coming years this problem can be averted by future  $\gamma$ -beam system at ELI-NP that anticipates higher  $\gamma$ -beam intensities and better spectral width than HI $\gamma$ S. An experiment with an active target TPC with electronic readout [83] was accepted as a Day-1 experiment at the ELI-NP.



# Chapter 8

## Summary

This thesis summarizes the four years of studies with the WarsawTPC — from the detector concept, designing the procedures and planning the experiments to analyzing the experimental data and obtaining the first results.

The first chapter of the thesis gives the physical motivation for the studies, the nuclear astrophysics context, the specifics of stellar nuclear reaction and the “paramount importance” of the  $^{12}\text{C}/^{16}\text{O}$  produced during the helium burning. The ratio is regulated by the relative rates of two reactions:  $3\alpha \rightarrow ^{12}\text{C}$  and  $^{12}\text{C}(\alpha, \gamma)^{16}\text{O}$ . The measurement of the  $^{12}\text{C}(\alpha, \gamma)^{16}\text{O}$  cross-section at the relevant energy pose a significant problem for the experimental technique.

To avert the problem a time reversed photodisintegration reaction  $^{16}\text{O}(\gamma, \alpha)^{12}\text{C}$  can be studied instead as the reaction cross-section can be related with the  $^{12}\text{C}(\alpha, \gamma)^{16}\text{O}$  cross-section by the detail balance principle.

To take advantage of the photodisintegration two prerequisites are required: an access to a monochromatic  $\gamma$ -beam with high intensity and a detector capable of measuring the low energy products of the reaction. The HI $\gamma$ S facility is one of a few in a world facilities with the  $\gamma$ -beam of the desired parameters.

The second chapter describes the WARSAW TPC detector — an active target time projection chamber with an electronic readout. The detector’s R&D took place at the University of Warsaw. The detector was designed with studying photo-nuclear reactions with the particular aim at the  $^{16}\text{O}(\gamma, \alpha)^{12}\text{C}$  photodisintegration. The detector employs a stack of three GEM foils for charge amplifications and a multilayered PCB pads organized into three families of strips (one strip family redundant). The DAQ is based on GET. The system is capable of external and self-triggering. A stack of three GEM foils is used for charge amplification.

The third chapter presents the experiment with the WARSAW TPC and the  $\gamma$ -beam of HI $\gamma$ S facility at TUNL, Durham, NC, USA. The experiment took place in two rounds in April 2022 and August 2022. The detector was filled with  $\text{CO}_2$  at subatmospheric pressure and the working points were optimized for the measurements of the  $^{16}\text{O}(\gamma, \alpha)^{12}\text{C}$  reaction.

A total of 15 experimental points in a center-of-mass energy range of 1.35–6.7 MeV were investigated. The expected background consists of other  $(\gamma, \alpha)$ ,  $(\gamma, p)$   $(\gamma, n)$  reactions with the naturally occurring isotopes of oxygen and carbon. The other type of background are  $\alpha$  particles emitted from the detectors hull. The background reactions can be separated from the investigated  $^{16}\text{O}(\gamma, \alpha)^{12}\text{C}$  reaction. While being categorized

as a background some of the measured reactions such as  $^{12}\text{C}(\gamma, 3\alpha)$  stand a separate research material on they own.

The fourth chapter describes the data preprocessing and event reconstruction algorithms. The preprocessing starts at the waveform level where the FPN and baseline corrections are applied. A channel mapping is applied to transform the electronic signals into a representation related to the physical problem. Representations of most important classes of events for the studies were given.

With the current study a manual reconstruction algorithm was used. In this procedure human experts marked the vertices and endpoints in the events. The resolution and compatibility were investigated statistically. To lessen the load on the experts an offline trigger is used.

The fifth chapter contains the analysis of the reconstructed data and estimation of the beam stability. A set of data quality checks and corrections was proposed such as calculating the beam misalignment from experimental data and verifying the drift velocity. The fiducial cuts were defined and applied in order to removed not-fully contained or corrupted events as well as events not correlated with the beam. In the next step a correction for detector efficiency was applied.

An isotopic selection procedure basing on the length of tracks was shown. In the next step a method of reconstruction of ion energy and establishing an energy scale was given. The energy effective resolution of the detector for the  $^{16}\text{O}(\gamma, \alpha)^{12}\text{C}$  events and manual reconstruction method was estimated to be 67(3) keV and much smaller than the width of the  $\gamma$ -beam.

The measured energy distributions of  $^{16}\text{O}(\gamma, \alpha)^{12}\text{C}$  reaction selected data were studies in order to calculate relative cross-section for sum of E1 and E2 components. The dependence of detector response on orientation was studied and a discrepancy between event oriented towards and against the readout plane was found.

In the next step angular distributions of the  $^{16}\text{O}(\gamma, \alpha)^{12}\text{C}$  reaction events were studied. The polarization of the  $\gamma$ -beam was calculated for the experimental data and a change of linear polarization fraction between the experimental campaigns was found. The results were in good agreement with the beam facility diagnostics.

The final part of the analysis discusses the polar angle distributions encoding the information about E1 and E2 cross-section ratios and E1–E2 phase mixing angle. The distributions were fitted to the energy selected experimental data and E1 and E2 cross-section ratio and phase mixing angle were obtained. The E1–E2 phase mixing angle was a free parameter of the fit. In a few cases the sensitivity of the fit to the cross-section ratio was too small with used sample sizes. A size of sample required to achieve needed sensitivity was estimated. Reconstruction of the rest of experimental material is expected to meet the requirements.

The sixth chapter presents the most important results of the analysis. Studying the absolute beam intensity was outside of the scope of this work and relative  $^{16}\text{O}(\gamma, \alpha)^{12}\text{C}$  cross-section of sum of the E1 and E2 was given. A qualitative comparison to the state of the art R-matrix fit was done.

The E1, E2 cross-sections were reported in a form of fraction of E1 cross-section to the sum of cross-sections. The fraction was compared with the theoretical prediction and no major discrepancies were found. cross-sections of the  $^{16}\text{O}(\gamma, \alpha)^{12}\text{C}$  E1, E2 components were reported.

Finally, the obtained values of E1–E2 phase mixing angle were compared with the theoretical prediction based on the scattering data. In literature the relationship between the E1–E2 phase mixing angle and the scattering was put into question, but no discrepancies were found at the studied effective energies.

An unexpected result was the first observation of dependence between spatial position and energy of the  $\gamma$ -beam at HI $\gamma$ S. To the knowledge no previous experiments and detectors used at HI $\gamma$ S were able to measure this dependence. A follow up experiment to investigate the observation is planned.

The seventh chapter gives an outlook into the future developments with the WARSAW TPC and ongoing work. To proceed with the study a machine based event reconstruction should be utilized instead of the currently used manual reconstruction. Two general notions of machine based reconstruction are possible: a reconstruction based on classical algorithms such as Hough line detection followed up by a ionization along the track fit, or a reconstruction based on machine learning. As a parallel effort the beam intensity measurements collected during the experiment can be studied and calibrated in order to calculate absolute cross-sections for both E1 and E2 components.

The capabilities of WARSAW TPC as a tool for studying  $\gamma$ -beam induced reactions were proven and a letter of intent to continue the experimental program at HI $\gamma$ S in a lower energy range was submitted.

The results in a form of E1–E2 phase mixing angle and relative cross-sections after further refinement can enrich the experimental knowledge on the  $^{12}\text{C}(\alpha, \gamma)^{16}\text{O}$  reaction. Moreover the data processing, reconstruction and analysis methods and workflows presented in this work can be either used or be a reference point for other analyses of the WARSAW TPC data.



# Appendix A

## Kinematics of photodisintegration of oxygen

The photodisintegration of oxygen  $O(\gamma, \alpha)C$  can be understood as a two-body production of excited oxygen from a  $\gamma$ -particle and oxygen, followed by a two-decay of the excited oxygen to an  $\alpha$ -particle and carbon:

$$\gamma + O \rightarrow O^* \rightarrow \alpha + C \quad (\text{A.1})$$

In order not to lose the generality the relativistic formulas are provided and subrelativistic limits are given when useful.

The relativistic relations for the total energy and kinetic energy are used. The relations hold in any reference frame and each particle since the omission of the reference frame index and usage of  $i$  index for the particle. A standard units system is used with the speed of light  $c$ .

Particle energy  $E$  expressed with the momentum  $\mathbf{p}$  and its invariant mass  $m$ :

$$E_i^2 = (\mathbf{p}_i c)^2 + (m_i c^2)^2 \quad (\text{A.2})$$

Energy  $E$  expressed as a sum of kinetic energy  $T$  and invariant mass  $m$ :

$$E_i = T_i + m_i c^2 \quad (\text{A.3})$$

By transforming Equations A.2 and A.3 relations between kinetic energy  $T$  and momentum  $\mathbf{p}$  can be found:

$$|\mathbf{p}_i| = \sqrt{T_i (T_i + 2m_i c^2)} \quad (\text{A.4})$$

$$T_i = \sqrt{(\mathbf{p}_i c)^2 + (m_i c^2)^2} - m_i c^2 \quad (\text{A.5})$$

The following formulas can be adapted for other photodisintegration reaction to two products such as  $^{12}\text{C}(\gamma, \alpha)^8\text{Be}$ ,  $^2\text{H}(\gamma, n)p$ , etc.

## A.1 Center of Mass reference frame

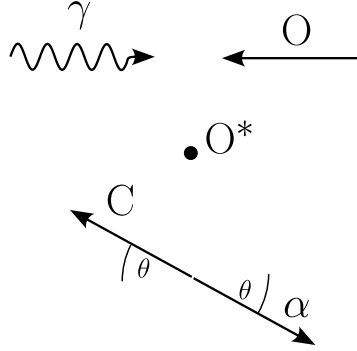


Figure A.1: Center of Mass reference frame.

The total momentum vanishes in the Center of Mass (CM) reference frame (Figure A.1):

$$\mathbf{p}_\gamma^{\text{CM}} + \mathbf{p}_\text{O}^{\text{CM}} = 0 \quad (\text{A.6})$$

Similarly for the reaction products:

$$\mathbf{p}_\alpha^{\text{CM}} + \mathbf{p}_\text{C}^{\text{CM}} = 0 \quad (\text{A.7})$$

The total energy in CM  $\sqrt{s}$  corresponds to the mass of excited oxygen:

$$\sqrt{s} = E_\gamma^{\text{CM}} + E_\text{O}^{\text{CM}} = E_\alpha^{\text{CM}} + E_\text{C}^{\text{CM}} \quad (\text{A.8})$$

Solve to obtain the product momentum:

$$|\mathbf{p}_\alpha^{\text{CM}}| = |\mathbf{p}_\text{C}^{\text{CM}}| = \frac{1}{2\sqrt{s}} \sqrt{s - (m_\alpha c^2 - m_\text{C} c^2)^2} \sqrt{s - (m_\alpha c^2 + m_\text{C} c^2)^2} \quad (\text{A.9})$$

Similarly for the substrates:

$$|\mathbf{p}_\gamma^{\text{CM}}| = |\mathbf{p}_\text{O}^{\text{CM}}| = \frac{s - m_\text{O}^2 c^4}{2\sqrt{s}} \quad (\text{A.10})$$

Excitation energy of oxygen  $E_\text{x}^{\text{CM}}$  is related to the total energy by:

$$E_\text{x}^{\text{CM}} = \sqrt{s} - m_\text{O} c^2 \quad (\text{A.11})$$

A Q-value ( $Q$ ) is defined as the difference of masses between the substrates and products of a reaction:

$$Q = (m_\text{O} - m_\alpha - m_\text{C}) c^2 \quad (\text{A.12})$$

Note the Q-value is a constant since it depends only on masses of the reagents not on their energies. The value for the  $^{16}\text{O}(\gamma, \alpha)^{12}\text{C}$  reaction is:

$$Q_{^{16}\text{O}(\gamma, \alpha)^{12}\text{C}} = -7.162 \text{ MeV} \quad (\text{A.13})$$

The Q-value can be also expressed with the kinetic energies:

$$Q = T_\alpha^{\text{CM}} + T_\text{C}^{\text{CM}} - E_\gamma^{\text{CM}} - T_\text{O}^{\text{CM}} \quad (\text{A.14})$$



The nuclear physics community often uses a values named Center of Mass Energy  $E_{\text{CM}}$  [1]:

$$E_{\text{CM}} = T_{\alpha}^{\text{CM}} + T_{\text{C}}^{\text{CM}} = Q + E_{\text{x}}^{\text{CM}} \quad (\text{A.15})$$

The used Center of Mass Energy  $E_{\text{CM}}$  is different than the center-of-mass or invariant mass known from general relativity  $\sqrt{s}$ .

## A.2 Laboratory reference frame

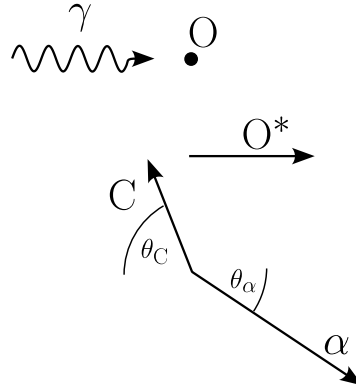


Figure A.2: Laboratory reference frame (target rest frame).

The laboratory reference frame (LAB) also called the target rest frame is define as a reference frame where the target (oxygen) is at rest (Figure A.2):

$$\mathbf{p}_{\text{O}}^{\text{LAB}} = 0 \quad (\text{A.16})$$

The relative speed between LAB and CM is given by:

$$\beta = \frac{E_{\gamma}^{\text{LAB}}}{E_{\gamma}^{\text{LAB}} + m_{\text{O}}} \quad (\text{A.17})$$

The Lorentz factor associated with the relative speed between the reference frames:

$$\gamma = \frac{1}{\sqrt{1 - \beta^2}} \quad (\text{A.18})$$

The  $E_{\gamma}^{\text{LAB}}$  can be expressed using other energies in LAB:

$$E_{\gamma}^{\text{LAB}} = E_{\alpha}^{\text{LAB}} + E_{\text{C}}^{\text{LAB}} - m_{\text{O}}c^2 \quad (\text{A.19})$$

A Lorentz boost can be applied to transform vectors between the reference frames. For any particle when  $\theta$  is the angle between the particle momentum and the boost direction:

$$\begin{pmatrix} E^{\text{CM}} \\ p^{\text{CM}} \cos(\theta^{\text{CM}}) \\ p^{\text{CM}} \sin(\theta^{\text{CM}}) \end{pmatrix} = \begin{pmatrix} \gamma & -\beta & 0 \\ \beta & \gamma & 0 \\ 0 & 0 & 1 \end{pmatrix} \begin{pmatrix} E^{\text{LAB}} \\ p^{\text{LAB}} \cos(\theta^{\text{LAB}}) \\ p^{\text{LAB}} \sin(\theta^{\text{LAB}}) \end{pmatrix} \quad (\text{A.20})$$

The boost Equation A.20 can be used to associate the  $\gamma$ -beam in the CM  $E_\gamma^{\text{CM}}$  is with the energy  $\gamma$ -beam in the LAB  $E_\gamma^{\text{LAB}}$  with the following formula:

$$E_\gamma^{\text{CM}} = E_\gamma^{\text{LAB}} \sqrt{\frac{1-\beta}{1+\beta}} = E_\gamma^{\text{LAB}} \sqrt{\frac{m_{\text{O}}}{2E_\gamma^{\text{LAB}} + m_{\text{O}}}} \quad (\text{A.21})$$

Another implication of the A.20 is the transformation of the  $\theta$  angle:

$$\theta^{\text{LAB}} = \arctan \left( \frac{\sin(\theta^{\text{CM}})}{\gamma \left( \cos(\theta^{\text{CM}}) + \beta \frac{E^{\text{CM}}}{p^{\text{CM}}} \right)} \right) \quad (\text{A.22})$$

Due to conservation principles the opening angle  $\vartheta^{\text{CM}}$  (angle between two particles) of products in CM is always equal  $180^\circ$ . The opening angle in LAB  $\vartheta^{\text{LAB}}$  is smaller than the  $180^\circ$ .

The Figure A.3 presents the transformations of chosen variables depending on the  $\theta^{\text{CM}}$  for the products of  $^{16}\text{O}(\gamma, \alpha)^{12}\text{C}$ .

### A.3 Useful relations

The kinetic energies of products in CM can be related by the energy-momentum conservation law:

$$T_{\text{C}}^{\text{CM}} = \sqrt{T_{\alpha}^{\text{CM}} (T_{\alpha}^{\text{CM}} + 2m_{\alpha}c^2) + (m_{\text{C}}c^2)^2} - m_{\text{C}}c^2 \quad (\text{A.23})$$

with a subrelativistic limit:

$$\lim_{T_{\alpha} \ll m_{\alpha}c^2} T_{\text{C}}^{\text{CM}} = T_{\alpha}^{\text{CM}} \frac{m_{\alpha}}{m_{\text{C}}} \quad (\text{A.24})$$

The Center of Mass Energy can be expressed with the  $\gamma$ -beam energy in LAB:

$$E_{\text{CM}} = \sqrt{m_{\text{O}}c^2 (2E_{\gamma}^{\text{LAB}} + m_{\text{O}}c^2)} - m_{\alpha}c^2 - m_{\text{C}}c^2 \quad (\text{A.25})$$

with a subrelativistic limit:

$$\lim_{E_{\gamma}^{\text{LAB}} \ll m_{\text{O}}c^2} E_{\text{CM}} = E_{\gamma}^{\text{LAB}} + Q \quad (\text{A.26})$$

The reverse relation of the  $\gamma$ -beam energy in LAB with the Center of Mass Energy takes the following form:

$$E_{\gamma}^{\text{LAB}} = \frac{(E_{\text{CM}} + m_{\alpha}c^2 + m_{\text{C}}c^2)^2 - (m_{\text{O}}c^2)^2}{2m_{\text{O}}c^2} \quad (\text{A.27})$$

with a subrelativistic limit:

$$\lim_{E_{\text{CM}} \ll m_{\text{O}}c^2} E_{\gamma}^{\text{LAB}} = E_{\text{CM}} - Q \quad (\text{A.28})$$

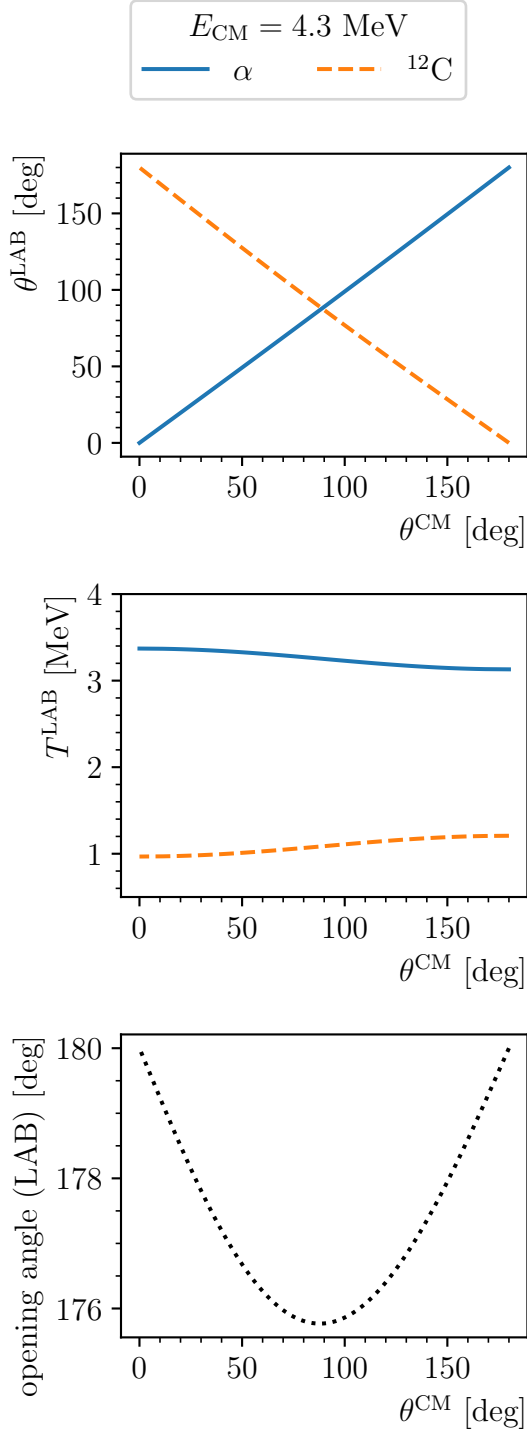


Figure A.3: CM to LAB transformation of  $^{16}\text{O}(\gamma, \alpha)^{12}\text{C}$  products for example energy  $E_{\text{CM}} = 4.3\text{MeV}$  ( $E_{\gamma}^{\text{LAB}} = 11.5\text{MeV}$ ). Top: angle transformation. The angle in LAB is a convex function of the angle in CM.

Center: Kinetic energy transformation. A fixed value of kinetic energy in the CM is shifted to higher or smaller values during the transformation to the LAB reference frame depending on the  $\theta^{\text{CM}}$ .

Bottom: opening angle (angle between the particles) transformation. The opening angle in CM equals  $180^\circ$ . The opening angle in LAB depends on the  $\theta^{\text{CM}}$  and is smaller than the  $180^\circ$  except for  $\theta^{\text{CM}} = 0^\circ$  and  $\theta^{\text{CM}} = 180^\circ$ .



# Appendix B

## Coordinate system

In the scope of WARSAW TPC three coordinate systems are considered:

1. UVW coordinate system — associated with the segmentation of readout with strip structures.
2. DET coordinate system — associated with the coordinates used during the chamber design.
3. BEAM coordinate system — associated with the  $\gamma$ -beam and reflecting the reaction kinematics.

### B.1 DET and BEAM coordinate systems

#### B.1.1 Definition

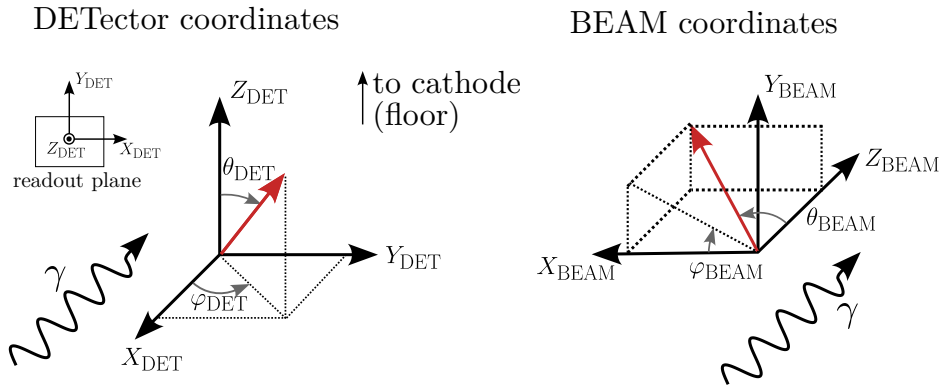


Figure B.1: DET and BEAM coordinate systems. Left: DET coordinate system associated with detector coordinates. The  $x_{\text{DET}}$  and  $y_{\text{DET}}$  are to the readout plane, while  $z_{\text{DET}}$  is along the drift direction and points towards readout (geographically up). Right: BEAM coordinate system associated with  $\gamma$ -beam coordinates. The nominal direction of  $\gamma$ -beam ( $z_{\text{BEAM}}$ ) corresponds to  $-x_{\text{DET}}$ .

The DET coordinate system is inherited from the chamber design. The planar coordinates  $x_{\text{DET}}$  and  $y_{\text{DET}}$  are parallel to the readout plane, while the  $z_{\text{DET}}$  coordinate is perpendicular and directed towards the readout (along the drift direction).

The BEAM coordinate system is a natural system to describe the physical phenomena as it is dictated by the orientation of beam. The  $z_{\text{BEAM}}$  coordinates is along the direction of the  $\gamma$  BEAM, while  $x_{\text{BEAM}}$  and  $y_{\text{BEAM}}$  are perpendicular to it.

The DET and BEAM coordinate systems are depicted in the Figure B.1. Both of the system are naturally related by the position of  $\gamma$ -beam relative to the detector.

The Cartesian DET system defines an associated DET polar coordinate system with the following formula:

$$\begin{cases} x_{\text{DET}} = r \cos(\varphi_{\text{DET}}) \sin(\theta_{\text{DET}}) \\ y_{\text{DET}} = r \sin(\varphi_{\text{DET}}) \sin(\theta_{\text{DET}}) \\ z_{\text{DET}} = r \cos(\theta_{\text{DET}}) \end{cases} \quad (\text{B.1})$$

Similarly a BEAM polar coordinate system can be associated with the Cartesian BEAM coordinate system:

$$\begin{cases} x_{\text{BEAM}} = r \cos(\varphi_{\text{BEAM}}) \sin(\theta_{\text{BEAM}}) \\ y_{\text{BEAM}} = r \sin(\varphi_{\text{BEAM}}) \sin(\theta_{\text{BEAM}}) \\ z_{\text{BEAM}} = r \cos(\theta_{\text{BEAM}}) \end{cases} \quad (\text{B.2})$$

### B.1.2 Transformation

Assuming the nominal  $\gamma$ -beam direction of  $-x_{\text{DET}}$  the transformation between the system can be expressed with:

$$\begin{pmatrix} x \\ y \\ z \end{pmatrix}_{\text{BEAM}} = \mathbf{A}_{\text{nominal}} \begin{pmatrix} x \\ y \\ z \end{pmatrix}_{\text{DET}} = \begin{pmatrix} 0 & -1 & 0 \\ 0 & 0 & 1 \\ -1 & 0 & 0 \end{pmatrix} \begin{pmatrix} x \\ y \\ z \end{pmatrix}_{\text{DET}} \quad (\text{B.3})$$

The transformation matrix is nonsingular and the transformation is invertible. For convenience the transformation can be expressed as a rotation  $\mathbf{R}$  with Euler angles [84]:

$$\begin{cases} \phi = \frac{\pi}{2} \\ \theta = -\frac{\pi}{2} \\ \psi = 0 \end{cases} \quad (\text{B.4})$$

$$\mathbf{A}_{\text{nominal}} = \mathbf{R}(\phi, \theta, \psi) \quad (\text{B.5})$$

A chamber misalignment (Section 5.1.3) can be taken into account by providing a beam tilt correction to the transformation. The Figure B.2 depicts a parametrization of the beam tilt with slope  $\alpha$  and offset  $r$ . The beam normal offset  $\boldsymbol{\xi}$  can be expressed with offset  $r$ :

$$\boldsymbol{\xi} = \begin{pmatrix} -r \sin(\arctan(\alpha)) \\ r \cos(\arctan(\alpha)) \\ 0 \end{pmatrix}_{\text{DET}} \quad (\text{B.6})$$

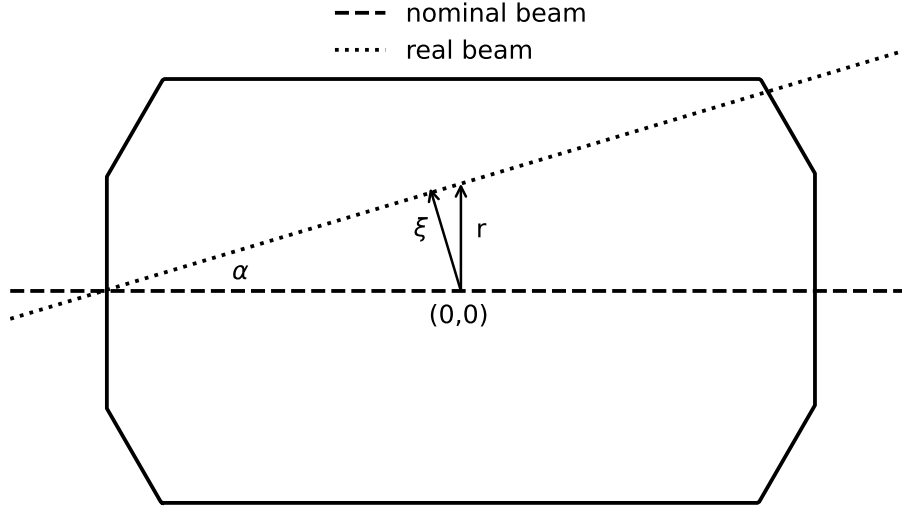


Figure B.2: Beam tilt correction. The real beam is tilted with slope  $\alpha$  and offset  $r$  with respect to the nominal beam. A beam normal offset  $\xi$  can be calculated as a projection of origin of coordinate system on the real beam. The beam tilt presented on the plot is exaggerated on purpose, the real beam expected in experimental data should follow the nominal direction with only a small correction.

For practical reasons the corrected transformation between DET and BEAM coordinate systems is factorized as a translation  $\mathbf{T}$  by beam normal offset  $\xi$  followed by nominal rotation  $\mathbf{A}_{\text{nominal}}$  and rotation  $\mathbf{R}$  by beam slope  $\alpha$  (expressed in the following formula with the Euler angles):

$$\begin{pmatrix} x \\ y \\ z \end{pmatrix}_{\text{BEAM}} = \mathbf{R} \left( \frac{\pi}{2}, \arctan \alpha, \frac{\pi}{2} \right) \mathbf{A}_{\text{nominal}} \mathbf{T}(\xi) \cdot \begin{pmatrix} x \\ y \\ z \end{pmatrix}_{\text{DET}} \quad (\text{B.7})$$

## B.2 UVW coordinate system

### B.2.1 Definition

A UVW coordinate system is associated with the readout strips. The coordinates  $u, v, w$  are used to describe position in readout plane and corresponds to the projection of a point on U, V, W strip directions. The U strip direction is parallel to the beam direction, while the V and W are tilted under  $-120^\circ$  and  $-60^\circ$  respectively. The  $t$  coordinate corresponds to the position along the drift direction and comes from the sampling of electronic signal. The UVW coordinate system is presented in the Figure B.3

Note the coordinates of this system are not orthogonal and the system is described with 4 coordinates (one redundant planar coordinate).

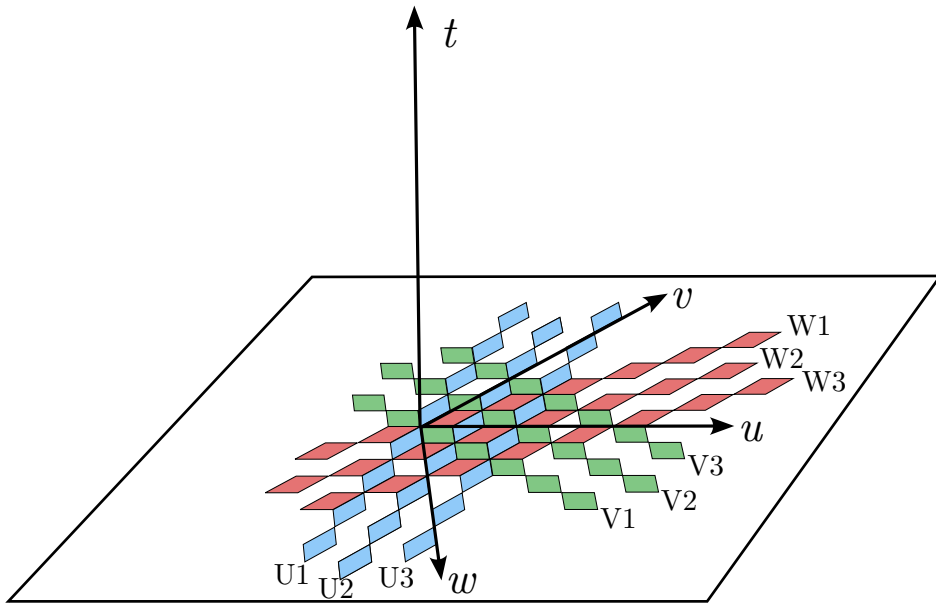


Figure B.3: UVW coordinate system. The three planar coordinates  $u, v, w$  corresponds to the projections of a given point on the readout strip directions U, V, W, while the vertical coordinate is measured in DAQ electronics time bins along the drift direction (perpendicular to the readout plane all).

### B.2.2 Transformation

Assuming a drift velocity  $v_d$  a transformation from DET to UVW coordinate system can be expressed with the following formula:

$$\begin{pmatrix} u \\ v \\ w \\ t \end{pmatrix} = \begin{pmatrix} \cos(0) & \sin(0) & 0 \\ \cos(-\frac{2\pi}{3}) & \sin(-\frac{2\pi}{3}) & 0 \\ \cos(-\frac{\pi}{3}) & \sin(-\frac{\pi}{3}) & 0 \\ 0 & 0 & \frac{1}{v_d} \end{pmatrix} \begin{pmatrix} x \\ y \\ z \end{pmatrix}_{\text{DET}} \quad (\text{B.8})$$

The angles appearing in this formula are fixed and related to the directions of the readout strips. The UVW has redundant coordinates the transformation is non-invertible. Since the natural notion during the data reconstruction is to measure positions in UVW related to the readout and transform to DET coordinate system, a few approaches has been proposed:

- pseudoinverse - a generalization of inversion for non-square matrix such as Moore-Penrose inverse can be used. While well known and defined, assumes all the coordinates in UVW are equally weighted which may not be strictly fulfilled given the coordinates are determined with finite and potentially different precision from the experimental data.
- reduced system inverse - by removing one of the  $u, v, w$  coordinates a non-redundant, invertible system can be obtained. Usually a coordinate obtained with the lowest precision or from degenerated data is chosen to be removed. Given the redundancy the removed coordinate can be later reobtained from the remaining



coordinates in self-consistent manner. For instance, an inversion using only  $u$  and  $v$  coordinates yields:

$$\begin{pmatrix} x \\ y \\ z \end{pmatrix}_{\text{DET}} = \begin{pmatrix} \cos(0) & \sin(0) & 0 \\ \cos\left(-\frac{2\pi}{3}\right) & \sin\left(-\frac{2\pi}{3}\right) & 0 \\ 0 & 0 & \frac{1}{v_d} \end{pmatrix}^{-1} \begin{pmatrix} u \\ v \\ t \end{pmatrix} \quad (\text{B.9})$$

- Monte Carlo fit - a minimization procedure is used to fit inverse UVW to DET relation. Accommodation for different weighting of coordinates is possible.

### B.3 Reference frames

In scope of this work two reference frames are used:

- LAB reference frame — associated with laboratory. Also target rest frame.
- CM reference frame — center-of-mass frame. A reference frame with zero total momentum, natural to describe physical phenomena such as nuclear reactions.

These frames are the same as presented in Appendix A, but this time they relationship and practical realisation will be discussed.

The reference frames are related by a Lorentz boost with  $\beta$  (formula for transformation from LAB to CM, the opposite sign for the other direction):

$$\beta = -\beta \mathbf{e}_{z_{\text{BEAM}}} \quad (\text{B.10})$$

The relative speed  $\beta$  is given by the formula A.17.

Depending on the problem, but very often in this work the coordinate system and reference frame are associated together into two pairs, namely (DET coordinate system, LAB reference frame) or (BEAM coordinate system, CM reference frame) as they appear to be best suited to describe detector and reaction related phenomena respectively.

In principle the  $\gamma$ -beam energy  $E_{\gamma}^{\text{LAB}}$  used in the formula A.17 can be expressed in two ways:

1. Nominal energy of the  $\gamma$ -beam ray. The same value is used for all the events and disregarding the beam energy spectrum width.
2. Energy of the  $\gamma$  beam reconstructed from measured data using the equation A.19. The value is established per event basis.

In practice, for light nuclei such as  $^{12,13}\text{C}$  or  $^{16,17,18}\text{O}$  and  $\gamma$ -beam energy in range 8–14 MeV with resolution  $\sim 1$  MeV, and assuming the energy reconstruction pessimistically of 1 MeV, the differences in boost obtained with both methods are negligible ( $\beta$  difference of order 1‰) as the whole problem operates in classical regime.

A certain advantage of using the nominal  $\gamma$ -beam energy is that the value does not relay on the reconstruction of ion energies and can be established independently from them. As such this method has been used in the current analysis for the Lorentz boost transformation between the LAB and the CM reference frames.



# Appendix C

## Detector Control System

The design of DCS for the WARSAW TPC was started as apart of the MSc thesis [20]. The concept was later refined and the functional implementation [85] was used during the experiments with the experiments with WARSAW TPC.

The DCS also known as a slow-control is a Supervisory Control And Data Acquisition (SCADA) [86] adapted for the needs of the physical experiments. The system acts as an interface for all the sensors, controllers and other experimental equipment accompanying the detector. The basic, most common need for implementing such system is the requirement of providing an online, remote access to the experimental setup during the experiments, when the physical attendance at the experiment hall is prohibited due to safety reasons such as radiation safety. In such cases usually the operators stand is moved to a separate Control room from which the experiment is conducted. The scheme of such situation is depicted in the Figure C.1.

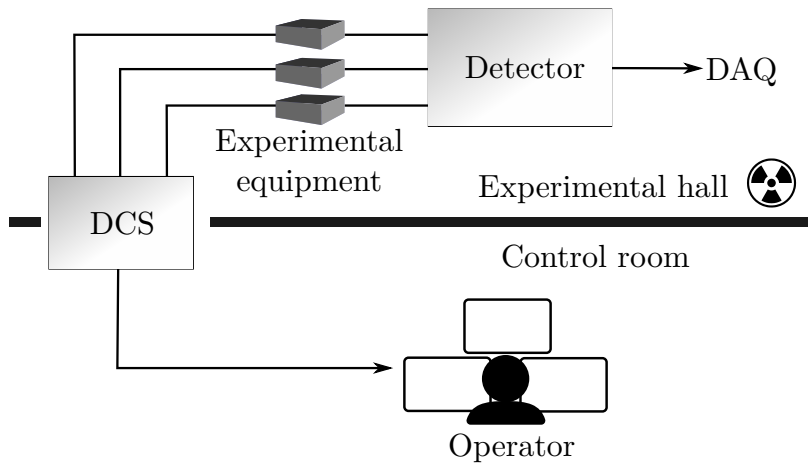


Figure C.1: DCS scheme

While the remote the access is an important feature for some of the experiments the system provides also other important functionalities on its own:

- monitoring - a semi-real access to the states of the devices can be provided to inspect the current status of the setup,

- controlling - besides reading the states of the devices the system may enable modifying their states by sending commands and request such changing the output voltage,
- state restriction - the system may implement a state machine model and restrict the set of available commands depending on the current state of the setup,
- alarming - a logical function can be performed on the monitor data and an alarm can be issued if predetermined conditions are not met,
- access control - restricting the functionalities to available groups of users with different levels of privileges such as users such as viewer, run operator, engineer, administrator,
- logging - keeping track of all the activities done in the scope of system,
- archiving - storing historical data for later reference and offline access,
- automation - a tedious and error prone set of consecutive actions can be automated into high level routines, such as pre-configuring the devices or a multi-step operation of brining up the detector.

## C.1 DCS structure

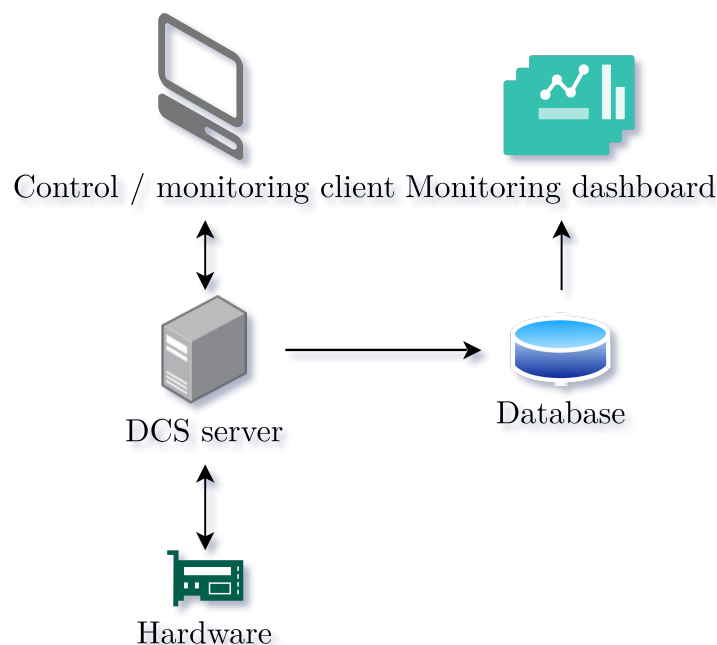


Figure C.2: Diagram of the DCS structure. The DCS servers control the communication with the hardware and store the records in a database. The database is connected to a dashboarding service that allows monitoring historical data. A client application can connect to the server to monitor or request a change of the state of the hardware through server.

The DCS dedicated for WARSAW TPC follows a client-server model. A scheme of the system structure is presented in the Figure C.2. In this model the server is responsible for all the direct communication with the devices (state polling, sending commands) and applying logical functions (alarms, high level routines).

A client can subscribe to a server updates of selected states and request a command to be issued or higher level routine to be performed. In such model the user cannot directly tamper with the equipment as its hidden behind the server. The server manages also its activity logging and archiving the measurement to an external Database (DB) that can be accessed by the users in order examine the historical information.

## C.2 Middleware

During the design phase of the DCS for WARSAW TPC several possible technologies for the server-client middleware were investigated. The two most commonly found frameworks among HEP community are Tango Controls [87] and EPICS [88] were considered among others and several drawbacks were found such as:

- relatively high entry barrier,
- outdated or unavailable documentation and developer guides (EPICS),
- feature bloat - both the system were designed to handle setups much more complex than the WARSAW TPC.

As an alternative a newer industrial open standard OPC UA [89] was chosen. Even though being originating from industry the standard has been embraced already by some parts of the HEP community and found its use both in CERN infrastructure [90] and experiments like ATLAS [91]. The usage of this framework when compared to EPICS or Tango Controls allows the system to better reflects the current needs of WARSAW TPC without the need to implementing the features that unused and minimizing the probability that the backing middleware will become abandoned in the near future.

The standard is actively developed and available on many platforms and operating systems, the APIs are provided for multiple programming languages. For instance clients written in Python or Java can communicate without issues with a server written in C.

The OPC UA stack used by the DCS is the open62541 [92] — an open source C99 implementation certified by the OPC Foundation. The same implementation is used by the CERN quasar [93].

## C.3 User interface

The DCS designed for WARSAW TPC includes a Graphical User Interface (GUI) client application aimed to be a run operator interface and a (Human-Machine-Interface HMI) for the experimental equipment and sensors. The interface implements a separate display for each device where the current measurements and states are displayed. An example window for a HV controller is presented in the Figure C.3.

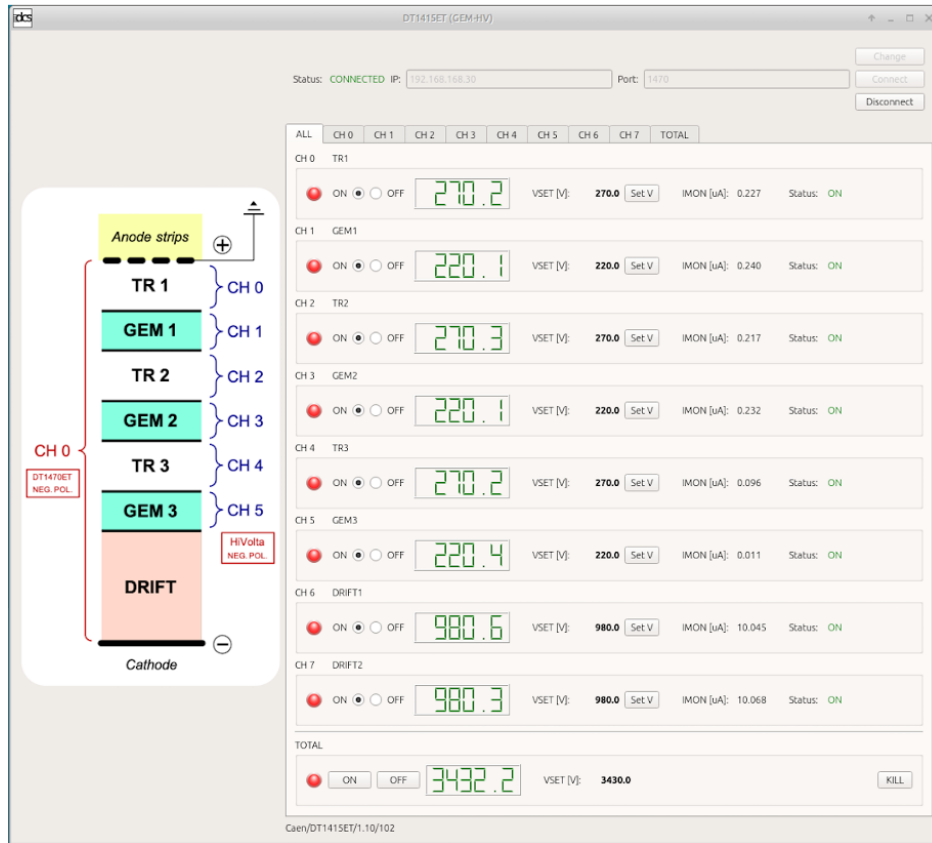


Figure C.3: DCS GUI client application. Operator can monitor and control the state of all the devices in experimental setup from native graphical windows. Example window for high voltage module is presented. The operator can among other options monitor the voltages and amplitudes of each channel as well as turn on or off outputs or set the voltages.

For compliance and debugging the server has been accessed and tested with an independent generic client UaExpert [94]. The dedicated operator interface graphical elements are based on the popular Qt library [95]. Note that thanks to the usage of client-server model the client can be run natively on a separate platform than the server application.

## C.4 Historical data

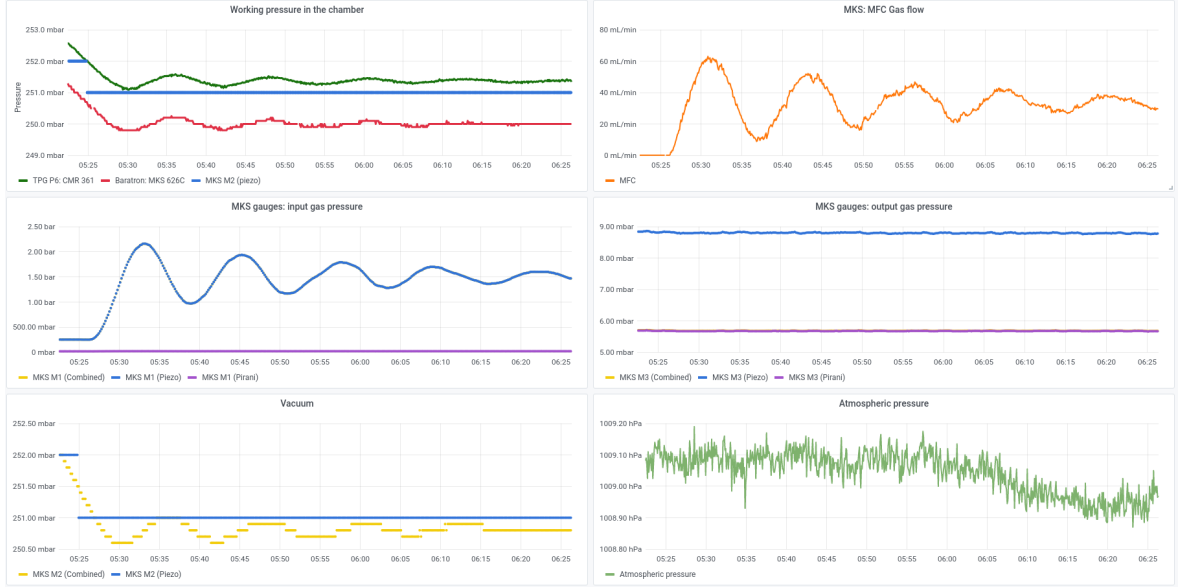


Figure C.4: Example Grafana [96] dashboard. Historical measurement data is stored in a time series database and presented using Grafana dashboarding service for later reference. The example shows historical record of stabilizing pressure after changing detector configuration.

The ability to monitor the statuses on-line in semi-real time is only one of the desired accesses to the data. The possibility to retrieve and check the historical statuses of the system becomes essential during debugging the system, assessing its stability and acts as a reference for offline physics analysis.

The DCS takes advantage of the “Data historizing” feature of the OPC UA specification, that allows the server to collect the variables and store them in a given DB.

The proof-of-concept version of the DCS for WARSAW TPC used SQLite [97] a relational DB based on SQL, but for the next iteration of the system it was decided that a time-based DB is a preferred choice over a relation database as the data on which the system operates has a natural representation as time series a time-based and gives more flexibility.

Finally the InfluxDB [98] was decided to be used with the system. Other alternatives were considered with the strongest contender being Prometheus [99], but were rejected given the higher popularity of InfluxDB [100].

A very important aspect of historical access is providing interfaces for accessing the DB in effective and efficient ways. A very popular choice for monitoring interface are so called dashboarding services that with no-code configuration allows for displaying and organizing a vast amount of graph, plots and tables constructed from the data stored in a DB.

The dashboarding system of choice for the DCS is Grafana [96]. An example dashboard for monitoring the pressure in WARSAW TPC is presented in the Figure C.4. The InfluxDB and Grafana is a very popular stack that has been used not only in an industry but also in a great number of scientific applications such as [101, 102].

## C.5 Experimental equipment and sensors

The DCS has been successfully applied and operates currently two setups at the University of Warsaw:

1. WARSAW TPC experimental setup.
2. Low-pressure test-bench circular detector [17].

The system has been used not only during the laboratory tests with the detectors but has been already used in full-scale physical experiments ([21, 58]).









Regardless of the additional features of the system its the most crucial component is support for the equipment. The DCS supports a number of devices from a range of system:

- Low Voltage (LV) system — LV Power Supply Unit (PSU)s, Power Distribution Units (PDU),
- HV system — HV PSUs,
- vacuum system — Proportional-Integral-Derivative (PID) controllers, gas-flow controllers, vacuum gauges, transducers,
- environmental sensors — temperature sensors, pressure gauges,

with a possibility to add new systems and devices as needed. A non-exhaustive list of supported equipment being use in laboratory test and the experiments is presented in Table C.1.



Table C.1: Experimental equipment used with the DCS. The devices are divided into three subsystems: low volt-age power supply units, high voltage power supply units and vacuum equipment.

Device	Vendor	Role	Remote Control Interfaces	Image
DT1415ET	CAEN [103]	8 channel HV PSU	Ethernet, USB	
DT1470ET	CAEN	4 channel HV PSU	Ethernet, USB	
N1471	CAEN	4 channel HV PSU	USB, RS-232	
HMP2020	Rohde & Schwartz [104]	2 channel LV PSU	Ethernet, RS-232/USB, GPIB	
HMP4040	Rohde & Schwartz	4 channel LV PSU	Ethernet, RS-232/USB, GPIB	
946 Vacuum System Controller	MKS Instruments [105]	PID controller	RS-232	
910 DualTrans <sup>TM</sup> MicroPirani <sup>TM</sup>	MKS Instruments	Vacuum gauge	RS-232	
TPG 362	Pfeiffer-Vacuum [106]	Vacuum gauge	RS-485, USB	

## C.6 Interlock

An interlock is a safety feature that couples the state of two devices in order to prevent occurrences of undesired or hazardous global state. The interlocks are important part of any hardware control system. In general two types of interlock implementation are considered.

### C.6.1 Hardware interlock

The hardware interlock relies on the capabilities built-in in the equipment by its vendors. While the naming depends on the vendor two general capabilities are considered:

1. Relay - a sensor with this capability can be set with a threshold. Depending on the setting when the measured value is either above or below the threshold the device will provide different analog output. Example device with such capability is a MKS 910 vacuum gauge that after measuring a pressure above set threshold will change the voltage at its relay output.
2. Interlock - a device with this capability will turn off and lock its outputs depending on the state that of its interlock input. Example device with this mechanism is a DT1415ET HV PSU that depending on the voltage at its interlock input will enter kill state and terminate its HV outlets.

Those basic capabilities can be extended with some additional behaviors such as relay with hysteresis that is more robust against fluctuations or locking interlock that will remain in terminate mode until the state is acknowledged and reset.

Given the features of relays and interlocks it is natural to create large systems of many devices fused with relays. The WARSAW TPC setup employs such interlock system to terminate the HV outlet connected to the chamber if the pressure inside the chamber crosses operational range. The main purpose of this system is to increase detectors safety by avoiding sparking and breakdowns.

### C.6.2 Software interlock

In cases when the vendor did not provide a device with any interlocking capabilities, such mechanism can be simulated by software. The disadvantages of this approach are that the speed of reaction is limited by sampling the state of the devices by the monitoring system. The other disadvantage is that such system requires constant connection to the software system and does not provide any form of safety if that system goes offline.

The clear advantage of this approach is that relay-interlock pair can be built using any variables and actions existing in the system and can be easily extended for more complicated series of operations or even created programmatically.

A software interlock has been used in the WARSAW TPC setup to provide extra level of safety and prevent overfilling of the chamber by coupling the measured pressure in the chamber with controlling the gas flow of mass flow controller operated from PID controller.

## C.7 Software project

The DCS as a software project is written in C++ with elements of C, Python and shell script. It uses the popular build system generator CMake. The project has two main dependencies:

1. Qt5 [95] for GUI part of the project.
2. open62541 [92] for middleware part of the project.

The project follows Semantic Versioning (SemVer) [107] based release cycle and uses Git [108] as Version Control System (VSC). A public MIT licensed mirror [85] of the software repository is available. The package includes both server and client applications as well as a software library. The software is distributed for x86 architectures in form of source code, deb packages or Open Container Initiative (OCI) containers (such as docker [109]). The projects implements the Continuous Integration/Continuous Delivery (CI/CD) practices via Gitlab Pipelines.

## C.8 3rd party bug fixes

During programming communication with the DT1415ET module by CAEN [103], a few inconsistencies between firmware 1.10 and documentation rev. 7 of the module were discovered and reported back to the vendor.caen



# Appendix D

## TPCReco

*To err is human, but to really foul things up  
you need a computer.*

— Paul R. Ehrlich

TPCReco is a software suite developed specifically for the WARSAW TPC. The wide range of this project covers:

- event viewer,
- event reconstruction with manual procedure and preliminary attempts at batch reconstruction [75, 76],
- general data analysis and data quality analysis,
- recent addition (May 2023) of the Monte Carlo simulations with fast-toy simulation or Geant4 [57].

The suite is based on ROOT [63] and GET [27] software. For user convenience the GUI application for online event preview as well as offline data viewer and manual reconstruction tool are provided. The Figure D.1 presents a screenshot from manual event reconstruction with the GUI application.

The suite comes with a collection of utility scripts for common workflows with WARSAW TPC data. As such the project is mostly written in C++ language with some minor elements written in Python or shell script.

The project evolved from a collection of legacy ROOT macros. After refactoring which aimed to bring the project closer to a standard development practices, the project's core is standard C++14 and using CMake [110] as a build generator system. A small but growing suit of tests with GTest framework [111] has also been added. The project is using Git [108] for VSC and follows a release cycle which make it transparent to track and audit.

The software is developed and deployed using both the OCI containers (such as docker [109]) and Apptainer (previous name Singularity) [112, 113]. Thanks to the use of container technology the software is equally accessible for the main DAQ server during the experimental run, High-Performance Computing (HPC) environment for eventual batch reconstruction and also on individual researches computers.

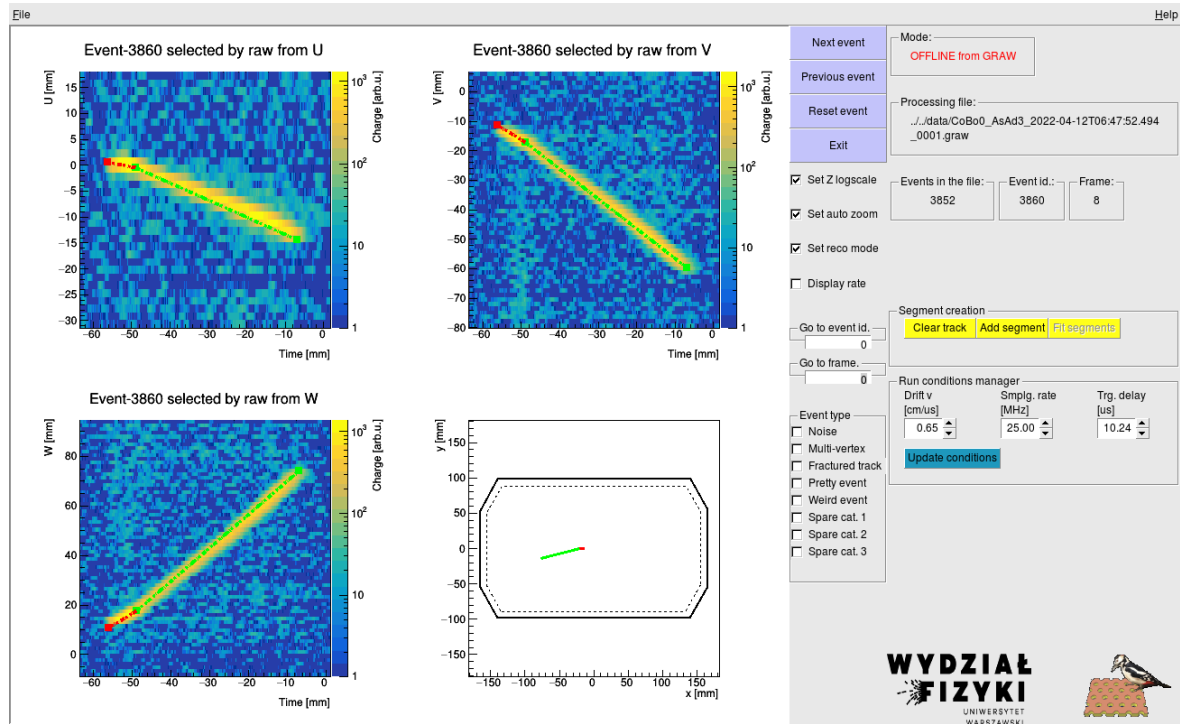


Figure D.1: TPCReco GUI application for online event preview, offline viewer and manual reconstruction. A manual fit to a 2-prong event is displayed.

While the TPCReco provides a general data analysis utilities, its libraries can also be used as a dependencies for ROOT or CMake based user analysis. Alternatively the output data formats produced by TPCReco can be converted with uproot [52] to typical Python formats when working with higher level language is expected to be more convenient (the user analysis described in Chapter 5 follows this path).

# References

1. deBoer, R. J. *et al.* The  $^{12}\text{C}(\alpha, \gamma)^{16}\text{O}$  reaction and its implications for stellar helium burning. *Rev. Mod. Phys.* **89**, 035007 (3 2017).
2. Fowler, W. A. Experimental and theoretical nuclear astrophysics: the quest for the origin of the elements. *Rev. Mod. Phys.* **56**, 149–179 (2 1984).
3. Rolfs, C. Nuclear reactions in stars. *Progress in Particle and Nuclear Physics* **46**, 23–35. ISSN: 0146-6410 (2001).
4. Weaver, T. A. & Woosley, S. Nucleosynthesis in massive stars and the  $^{12}\text{C}(\alpha, \gamma)^{16}\text{O}$  reaction rate. *Physics Reports* **227**, 65–96. ISSN: 0370-1573 (1993).
5. Dyer, P. & Barnes, C. The  $^{12}\text{C}(\alpha, \gamma)^{16}\text{O}$  reaction and stellar helium burning. *Nuclear Physics A* **233**, 495–520. ISSN: 0375-9474 (1974).
6. M.Assuncao. E1 and E2 S factors of  $^{12}\text{C}(\alpha, \gamma_0)^{16}\text{O}$  from  $\gamma$ -ray angular distributions with a  $4\pi$ -detector array. *Physical Review C* **73**, 055801 (May 2006).
7. Kunz, R. *et al.*  $^{12}\text{C}(\alpha, \gamma)^{16}\text{O}$ : The Key Reaction in Stellar Nucleosynthesis. *Phys. Rev. Lett.* **86**, 3244–3247 (15 2001).
8. Plag, R. *et al.*  $^{12}\text{C}(\alpha, \gamma)^{16}\text{O}$  studied with the Karlsruhe  $4\pi$  BaF<sub>2</sub> detector. *Phys. Rev. C* **86**, 015805 (1 2012).
9. Smith, R., Gai, M., Stern, S. R., Schweitzer, D. K. & Ahmed, M. W. Precision measurements on oxygen formation in stellar helium burning with gamma-ray beams and a Time Projection Chamber. *Nature Communications* **12**, 5920. ISSN: 2041-1723 (2021).
10. Von Wimmersperg, U., Kernel, G., Allardyce, B., Mason, W. & Tanner, N. A test of time reversal invariance through detailed balance of the reaction  $^{12}\text{C}(\alpha, \gamma)^{16}\text{O}$ . *Physics Letters B* **33**, 291–293. ISSN: 0370-2693 (1970).
11. Weller, H. R. *et al.* Research opportunities at the upgraded HI $\gamma$ S facility. *Progress in Particle and Nuclear Physics* **62**, 257–303. ISSN: 0146-6410 (2009).
12. Gales, S *et al.* The extreme light infrastructure—nuclear physics (ELI-NP) facility: new horizons in physics with 10 PW ultra-intense lasers and 20 MeV brilliant gamma beams. *Reports on Progress in Physics* **81**, 094301 (2018).
13. Ziegler, J. F. Stopping of energetic light ions in elemental matter. *Journal of Applied Physics* **85**, 1249–1272. ISSN: 0021-8979. eprint: [https://pubs.aip.org/aip/jap/article-pdf/85/3/1249/10597440/1249\\_1\\_online.pdf](https://pubs.aip.org/aip/jap/article-pdf/85/3/1249/10597440/1249_1_online.pdf) (Feb. 1999).

14. Ziegler, J. F., Ziegler, M. & Biersack, J. SRIM - The stopping and range of ions in matter (2010). *Nuclear Instruments and Methods in Physics Research Section B: Beam Interactions with Materials and Atoms* **268**. 19th International Conference on Ion Beam Analysis, 1818–1823. ISSN: 0168-583X (2010).
15. Nygren, D. R. Origin and development of the TPC idea. *Nuclear Instruments and Methods in Physics Research Section A: Accelerators, Spectrometers, Detectors and Associated Equipment* **907**. Advances in Instrumentation and Experimental Methods (Special Issue in Honour of Kai Siegbahn), 22–30. ISSN: 0168-9002 (2018).
16. Ćwiok, M. Nuclear Reactions at Astrophysical Energies with  $\gamma$ -ray Beams: A Novel Experimental Approach. *Acta Phys. Polon. B* **47**, 707 (2016).
17. Ćwiok, M. *et al.* A TPC Detector for Studying Photo-nuclear Reactions at Astrophysical Energies with Gamma-ray Beams at ELI-NP. *Acta Phys. Polon. B* **49**, 509–514 (2018).
18. Bihalowicz, J. S. *The mini ELITPC: Reconstruction and identification of charged particles tracks during beam tests at IFIN-HH in 2017 IEEE International Young Scientists Forum on Applied Physics and Engineering (YSF)* (2017), 259–262.
19. Djakonow-Lichnowska, A. *Komora projekcji czasowej do badania reakcji wtórnych neutronów w akceleratorze 3MV Tandetron w IFIN-HH* Polish only. Master's thesis (University of Warsaw, 2022).
20. Fila, M. *Detector Control System of the ELITPC chamber in experiments with gamma beams – the software framework* Master's thesis (University of Warsaw, 2019).
21. Kuich, M. *et al.* Active Target TPC for Study of Photonuclear Reactions at Astrophysical Energies. *Acta Physica Polonica B Proceedings Supplement* **16**, 1 (2023).
22. Ćwiok, M. *et al.* Warsaw Active-Target TPC: a new detector for photonuclear reactions studies at astrophysical energies. *EPJ Web of Conferences* (Submitted).
23. Sauli, F. The gas electron multiplier (GEM): Operating principles and applications. *Nuclear Instruments and Methods in Physics Research Section A: Accelerators, Spectrometers, Detectors and Associated Equipment* **805**. Special Issue in memory of Glenn F. Knoll, 2–24. ISSN: 0168-9002 (2016).
24. Charpak, G., Bouclier, R., Bressani, T., Favier, J. & Zupancic, C. The Use of Multiwire Proportional Counters to Select and Localize Charged Particles. *Nucl. Instrum. Meth.* **62**, 262–268 (1968).
25. Antonello, M. *et al.* Precise 3D Track Reconstruction Algorithm for the ICARUS T600 Liquid Argon Time Projection Chamber Detector. *Advances in High Energy Physics* **2013**, 1–16 (2013).
26. Procureur, S., Dupré, R. & Aune, S. Genetic multiplexing and first results with a 50x50cm<sup>2</sup> Micromegas. *Nuclear Instruments and Methods in Physics Research Section A: Accelerators, Spectrometers, Detectors and Associated Equipment* **729**, 888–894. ISSN: 0168-9002 (2013).



27. Pollacco, E. *et al.* GET: A generic electronics system for TPCs and nuclear physics instrumentation. *Nuclear Instruments and Methods in Physics Research Section A: Accelerators, Spectrometers, Detectors and Associated Equipment* **887**, 81–93. ISSN: 0168-9002 (2018).
28. Giovinazzo, J., Pancin, J., Pibernat, J. & Roger, T. ACTAR TPC performance with GET electronics. *Nuclear Instruments and Methods in Physics Research Section A: Accelerators, Spectrometers, Detectors and Associated Equipment* **953**, 163184. ISSN: 0168-9002 (2020).
29. Ayyad, Y. *et al.* Next-generation experiments with the Active Target Time Projection Chamber (AT-TPC). *Nuclear Instruments and Methods in Physics Research Section A: Accelerators, Spectrometers, Detectors and Associated Equipment* **954**, 161341. ISSN: 0168-9002 (2020).
30. Koshchiy, E. *et al.* Texas Active Target (TexAT) detector for experiments with rare isotope beams. *Nuclear Instruments and Methods in Physics Research Section A: Accelerators, Spectrometers, Detectors and Associated Equipment* **957**, 163398. ISSN: 0168-9002 (2020).
31. Estee, J. *et al.* Extending the dynamic range of electronics in a Time Projection Chamber. *Nuclear Instruments and Methods in Physics Research Section A: Accelerators, Spectrometers, Detectors and Associated Equipment* **944**, 162509. ISSN: 0168-9002 (2019).
32. Ritt, S. *ELOG* <https://elog.psi.ch/elog/>. Accessed: 2023.08.08.
33. Wang, M., Huang, W. J., Kondev, F. G., Audi, G. & Naimi, S. The AME 2020 atomic mass evaluation (II). Tables, graphs and references. *Chin. Phys. C* **45**, 030003 (2021).
34. Zimmerman, W. R. *et al.* Unambiguous Identification of the Second  $2^+$  State in  $^{12}\text{C}$  and the Structure of the Hoyle State. *Phys. Rev. Lett.* **110**, 152502 (15 2013).
35. Haverson, K. PhD thesis (In preparation).
36. Otuka, N. *et al.* Towards a More Complete and Accurate Experimental Nuclear Reaction Data Library (EXFOR): International Collaboration Between Nuclear Reaction Data Centres (NRDC). *Nuclear Data Sheets* **120**, 272–276. ISSN: 0090-3752 (2014).
37. NCBJ. *Tukank8k Multichannel Analyzer* <https://tukan.ncbj.gov.pl/>. Accessed: 2022.08.22.
38. Giovinazzo, J. *et al.* GET electronics samples data analysis. *Nuclear Instruments and Methods in Physics Research Section A: Accelerators, Spectrometers, Detectors and Associated Equipment* **840**, 15–27. ISSN: 0168-9002 (2016).
39. Cowan, G. A survey of unfolding methods for particle physics. *Conf. Proc. C* **0203181** (eds Whalley, M. R. & Lyons, L.) 248–257 (2002).
40. Krischer, W., Moorhead, W. G. & Seyboth, P. Present Status of Cern HPD Programme for Bubble Chambers. *IEEE Transactions on Nuclear Science* **12**, 305–309 (1965).

41. Culwick, B. & Goldsack, S. Measuring machine for bubble chamber photographs. *Nuclear Instruments and Methods* **13**, 118–123. ISSN: 0029-554X (1961).
42. Hough, P. V. C. Machine Analysis of Bubble Chamber Pictures. *Conf. Proc. C* **590914** (ed Kowarski, L.) 554–558 (1959).
43. Bohm, G. & Zech, G. Introduction to Statistics and Data Analysis for Physicists (Jan. 2010).
44. *Encyclopedia of Machine Learning* (eds Sammut, C. & Webb, G. I.) (Springer US, 2010).
45. Virtanen, P. *et al.* SciPy 1.0: Fundamental Algorithms for Scientific Computing in Python. *Nature Methods* **17**, 261–272 (2020).
46. Harris, C. R. *et al.* Array programming with NumPy. *Nature* **585**, 357–362 (2020).
47. Hunter, J. D. Matplotlib: A 2D graphics environment. *Computing in Science & Engineering* **9**, 90–95 (2007).
48. Wes McKinney. *Data Structures for Statistical Computing in Python* in *Proceedings of the 9th Python in Science Conference* (eds Stéfan van der Walt & Jarrod Millman) (2010), 56–61.
49. Meurer, A. *et al.* SymPy: symbolic computing in Python. *PeerJ Computer Science* **3**, e103. ISSN: 2376-5992 (Jan. 2017).
50. Pedregosa, F. *et al.* Scikit-learn: Machine Learning in Python. *Journal of Machine Learning Research* **12**, 2825–2830 (2011).
51. Rodrigues, E. *et al.* The Scikit HEP Project – overview and prospects. *EPJ Web Conf.* **245** (eds Doglioni, C. *et al.*) 06028. arXiv: 2007.03577 [physics.comp-ph] (2020).
52. Pivarski, J. *et al.* Uproot Sept. 2017.
53. Dembinski, H. & *et al.*, P. O. scikit-hep/iminuit (2020).
54. Schreiner, H., Liu, S. & Goel, A. *hist*
55. Friman-Gayer, U. *Probing Nuclear Structure Relevant for Neutrinoless Double-Beta Decay with Nuclear Resonance Fluorescence* en. PhD thesis (Technische Universität, Darmstadt, 2020).
56. Friman-Gayer, U. *Horst* <https://github.com/charlespwd/project-title>. 2022.
57. Allison, J. *et al.* Geant4 developments and applications. *IEEE Transactions on Nuclear Science* **53**, 270–278 (2006).
58. Ówiok, M. *et al.* Studies of photo-nuclear reactions at astrophysical energies with an active-target TPC. *EPJ Web of Conferences* **279** (eds Freeman, S., Lederer-Woods, C., Manna, A. & Mengoni, A.) 04002 (2023).
59. Biagi, S. Monte Carlo simulation of electron drift and diffusion in counting gases under the influence of electric and magnetic fields. *Nuclear Instruments and Methods in Physics Research Section A: Accelerators, Spectrometers, Detectors and Associated Equipment* **421**, 234–240. ISSN: 0168-9002 (1999).

60. Ayyad, Y., Bazin, D., Beceiro-Novo, S., Cortesi, M. & Mittig, W. Physics and technology of time projection chambers as active targets. *Eur. Phys. J. A* **54**, 181 (2018).
61. Ajzenberg-Selove, F. Energy levels of light nuclei  $A = 16$ -17. *Nuclear Physics A* **460**, 1–110. ISSN: 0375-9474 (1986).
62. Adye, T. *Unfolding algorithms and tests using RooUnfold* in *PHYSTAT 2011* (CERN, Geneva, 2011), 313–318. arXiv: 1105.1160 [physics.data-an].
63. Brun, R. & Rademakers, F. ROOT — An object oriented data analysis framework. *Nuclear Instruments and Methods in Physics Research Section A: Accelerators, Spectrometers, Detectors and Associated Equipment* **389**. New Computing Techniques in Physics Research V, 81–86. ISSN: 0168-9002 (1997).
64. Bourbeau, J. & Hampel-Arias, Z. PyUnfold: A Python package for iterative unfolding. *Journal of Open Source Software* **3**, 741 (2018).
65. D’Agostini, G. A Multidimensional unfolding method based on Bayes’ theorem. *Nucl. Instrum. Meth. A* **362**, 487–498 (1995).
66. Hodges, J. L. The significance probability of the smirnov two-sample test. *Arkiv för Matematik* **3**, 469–486 (1958).
67. Brune, C. R. Electric-multipole interference effects in the  $^{12}\text{C}(\gamma, \alpha)^{16}\text{O}$  reaction. *Phys. Rev. C* **64**, 055803 (5 2001).
68. Hecht, E. *Optics* ISBN: 9788131718070 (Pearson, 2012).
69. Wu, Y. Private Communication. Durham, NC, USA, 2022, 2023.
70. Plaga, R. *et al.* The scattering of alpha particles from  $^{12}\text{C}$  and the  $^{12}\text{C}(\alpha, \gamma)^{16}\text{O}$  stellar reaction rate. *Nuclear Physics A* **465**, 291–316. ISSN: 0375-9474 (1987).
71. Gai, M. Ambiguities in the rate of oxygen formation during stellar helium burning in the  $^{12}\text{C}(\alpha, \gamma)$  reaction. *Phys. Rev. C* **88**, 062801 (6 2013).
72. Tischhauser, P. *et al.* Measurement of elastic  $^{12}\text{C} + \alpha$  scattering: Details of the experiment, analysis, and discussion of phase shifts. *Phys. Rev. C* **79**, 055803 (5 2009).
73. Duda, R. O. & Hart, P. E. Use of the Hough Transformation to Detect Lines and Curves in Pictures. *Commun. ACM* **15**, 11–15. ISSN: 0001-0782 (1972).
74. Fischler, M. A. & Bolles, R. C. Random Sample Consensus: A Paradigm for Model Fitting with Applications to Image Analysis and Automated Cartography. *Commun. ACM* **24**, 381–395. ISSN: 0001-0782 (1981).
75. Kalinowski, A. *Highlights on track reconstruction in modern experiments* Faculty of Physics at the University of Warsaw (High Energy Physics Seminar). <https://indico.cern.ch/event/863628/#1-highlights-on-track-reconstr> (2023).
76. Fila, M. *Toward event reconstruction in an active-target TPC with strip readout* New Trends in Nuclear Physics Detectors NTNPD-2021. <https://indico.jinr.ru/event/2444/contributions/14464/> (2023).

77. Acciarri, R. *et al.* Convolutional neural networks applied to neutrino events in a liquid argon time projection chamber. *Journal of Instrumentation* **12**, P03011 (2017).
78. Kuchera, M. *et al.* Machine learning methods for track classification in the AT-TPC. *Nuclear Instruments and Methods in Physics Research Section A: Accelerators, Spectrometers, Detectors and Associated Equipment* **940**, 156–167. ISSN: 0168-9002 (2019).
79. Graczykowski, L. K., Jakubowska, M., Deja, K. R. & Kabus, M. Using machine learning for particle identification in ALICE. *JINST* **17**, C07016. arXiv: 2204.06900 [nucl-ex] (2022).
80. Wu, H. *et al.* Machine learning method for 12C event classification and reconstruction in the active target time-projection chamber. *Nuclear Instruments and Methods in Physics Research Section A: Accelerators, Spectrometers, Detectors and Associated Equipment* **1055**, 168528. ISSN: 0168-9002 (2023).
81. Smith, R. *Supervised Machine Learning TPC analysis for nuclear structure studies using gamma-beam* Time Projection Chamber 2023 (workshop). [https://cyclotron.tamu.edu/tpc2023/slides/5\\_Thu\\_AM/Robin\\_Smith\\_Machine\\_Learning\\_for\\_12C.pptx](https://cyclotron.tamu.edu/tpc2023/slides/5_Thu_AM/Robin_Smith_Machine_Learning_for_12C.pptx) (2023).
82. He, K., Zhang, X., Ren, S. & Sun, J. *Deep Residual Learning for Image Recognition* in *2016 IEEE Conference on Computer Vision and Pattern Recognition (CVPR)* (2016), 770–778.
83. Filipescu, D. *et al.* Perspectives for photonuclear research at the Extreme Light Infrastructure-Nuclear Physics (ELI-NP) facility. *The European Physical Journal A* **51**, 1–30 (2015).
84. Landau, L. & Lifshitz, E. *Mechanics: Volume 1* ISBN: 9780750628969 (Elsevier Science, 1976).
85. Fila, M. *m-fila/ELITPCdcs*: <https://doi.org/10.5281/zenodo.6958164>. Version v1.8.3. Aug. 2022.
86. Daneels, A. & Salter, W. What is SCADA? *Conf. Proc. C* **991004** (eds Bulfone, D. & Daneels, A.) 339–343 (1999).
87. Gotz, A. *et al.* *TANGO A CORBA BASED CONTROL SYSTEM* in (Oct. 2003).
88. Dalesio, L. EPICS: Recent Applications and Future Directions (Invited). *Conf. Proc. C* **0106181** (eds Lucas, P. W. & Webber, S.) 276–278 (2001).
89. OPC Foundation. *OPC UA* <https://opcfoundation.org/>. Accessed: 2023.04.12.
90. Stockinger, E. *et al.* OPC-UA Data Acquisition for the C2MON Framework. *JACoW ICALEPCS2021*, TUPV005 (2022).
91. Nikiel, P. P., Farnham, B., Schlenker, S., Boterenbrood, H. & Filimonov, V. *OPC Unified Architecture within the Control System of the ATLAS Experiment* in *14th International Conference on Accelerator & Large Experimental Physics Control Systems* (2014), moppc032.

92. Palm, F., Gruner, S., Pfrommer, J., Graube, M. & Urbas, L. *Open source as enabler for OPC UA in industrial automation* in *2015 IEEE 20th Conference on Emerging Technologies & Factory Automation (ETFA)* (2015), 1–6.
93. Nikiel, P., Moschovakos, P. & Schlenker, S. *quasar : The Full-Stack Solution for Creation of OPC-UA Middleware* in *17th International Conference on Accelerator and Large Experimental Physics Control Systems* (2020), MOPHA100.
94. Automation, U. *UaExper* <https://www.unified-automation.com/products/development-tools/uaexpert.html>. Accessed: 2023.08.08.
95. Qt Group. *Qt 5* <https://doc.qt.io/qt-5/index.html>. Accessed: 2023.04.03.
96. Grafana Labs. *Grafana* <https://grafana.com/>. Accessed: 2023.04.03.
97. Hipp, D. R. *SQLite* [www.sqlite.org/src/](http://www.sqlite.org/src/). Accessed: 2023.04.12.
98. influxdata. *InfluxDB* <https://www.influxdata.com/>. Accessed: 2023.04.03.
99. Rabenstein, B. & Volz, J. *Prometheus: A Next-Generation Monitoring System (Talk)* in (USENIX Association, Dublin, May 2015).
100. *DB-Engines, DB-Engines Ranking - popularity ranking of time Series DBMS, 2019*. <https://db-engines.com/en/ranking/time+series+dbms>. Accessed: 2023.04.12.
101. Flucke, G. *et al.* Karabo Data Logging: InfluxDB Backend and Grafana UI. *JACoW ICALEPCS2021*, MOBL04 (2022).
102. Vino, G., Chibante Barroso, V., Elia, D. & Wegrzynek, A. *A Monitoring System for the New ALICE O2 Farm* in *17th International Conference on Accelerator and Large Experimental Physics Control Systems* (2020), TUDPP01.
103. CAEN <https://www.caen.it>. [Accessed: 2023-06-21].
104. Rohde & Schwarz <https://www.rohde-schwarz.com>. [Accessed: 2023-06-21].
105. MKS Instruments <https://www.mksinst.com>. [Accessed: 2023-06-21].
106. Pfeiffer Vacuum <https://www.pfeiffer-vacuum.com>. [Accessed: 2023-06-21].
107. Tom Preston-Werner. *SemVer* <https://semver.org/>. Accessed: 2023.08.02.
108. Chacon, S. & Straub, B. *Pro git* (Apress, 2014).
109. Merkel, D. Docker: lightweight linux containers for consistent development and deployment. *Linux journal* **2014**, 2 (2014).
110. Martin, K. & Hoffman, B. *Mastering CMake Version 3.1* ISBN: 9781930934313 (Kitware Incorporated, 2015).
111. GoogleTest Authors. *GoogleTest* <https://github.com/google/googletest>. 2023.
112. Kurtzer, G. M., Sochat, V. & Bauer, M. W. Singularity: Scientific containers for mobility of compute. *PLOS ONE* **12**, 1–20 (May 2017).
113. Kurtzer, G. M. *et al.* *hpcng/singularity: Singularity 3.7.3* version v3.7.3. Apr. 2021.